Microstructural characterization of white etching cracks in 100Cr6 bearing steel with emphasis on the role of carbon

Von der Fakultät für Georessourcen und Materialtechnik der

Rheinisch-Westfälischen Technischen Hochschule Aachen

zur Erlangung des akademischen Grades eines

Doktors der Ingenieurwissenschaften

genehmigte Dissertation

vorgelegt von

M.Sc. David Mayweg

aus Starnberg

Berichter: Prof. Dr.-Ing. habil. Dierk Raabe

Univ.-Prof. Dr. rer. nat. Joachim Mayer

Tag der mündlichen Prüfung: 25.02.2021

Acknowledgments

As this season of intense efforts draws to an end, it is adequate to express my gratitude to the people who accompanied and helped me along the way. I feel humbled to know so many kind women and men who supported me in very different ways during the last years. I want to express my sincerest thanks to:

- Prof. Dierk Raabe for giving me the opportunity to work at the Max-Planck-Institut für Eisenforschung. It is to his credit that the institute provides such a plethora of opportunities to conduct investigations. Besides providing excellent facilities, the most important factor is that no matter what trouble one runs into, expertise on any number of topics (almost all) is available virtually next door.
- Prof. Joachim Mayer for his willingness to review this thesis, the general support of the project, and discussion of individual results. I want to specifically acknowledge him for providing the sample that allowed me to discover all the things I present in this thesis.
- My daily supervisor Dr. Michael Herbig. The completion of this thesis would not have been possible without him providing continued support, especially after major and minor setbacks and the following necessary restarts and the challenges ensuing from these.
- Dr. Lutz Morsdorf, whose attention to detail helped me immensely; without him pushing me to keep my eyes open and meticulously analyze the smallest features, I might have even overlooked key aspects.
- Katja Angenendt, Monika Nellessen, Christian Broß, Volker Kree, and Andreas Sturm, for keeping the microscopes up and running and the time they invested in instruction.
- Markus Bormann, Jürgen Baseler, Domenic Lindlau, Eugen Trautenbach, Jens Dose, Tristan Wickfeld, Mario Bütow, and Ralf Seelbach for manufacturing the parts for the test rig, many helpful suggestions, and also for putting up with my frequent special requests for sample preparation.
- Jürgen Wichert, Frank Schlüter, Frank Rütters, Dennis Klapproth, Michael Adamek, and Dr. Christian Baron for their willingness to help out on short notice on numerous occasions to keep my experiments running.
- Prof. Hauke Springer for valuable discussions regarding the design of the rolling contact fatigue test rig.
- Dr. Shanoob Balachandran Nair and Dr. Zita Zachariah for many hours of experiments conducted together and the amazing quality and quantity of spicy dishes served on Sunday noon.

- Drs. Huan Zhao, Andrew J. Breen, Leigh T. Stephenson, Markus T. Kühbach, Supriya Nandy, Isnaldi Souza Filho, Alisson Kwiatkowski da Silva, Baptiste J. G. Gault, Dirk Ponge, Franz Roters, Stefan Zaefferer, and Prof. Christoph Kirchlechner, Prof. Matthew Kasemer, Prof. Eric A. Jägle, Prof. Martin Diehl and Prof. Alfons Fischer for experimental support and many fruitful discussions on topics that are too numerous to recount but steered me in the right direction time and time again.
- Prof. Xiaoxiang Wu, and Drs. Yu Qin and Yanhong Chang for their support in conducting APT experiments and – amongst other things – especially for teaching me how to 包饺子!
- Drs. Jiwon Jeong, Xuyang Zhou, Wenjun Lu and Mrs. Irina Wossak and Mr.. Benjamin Breitbach for experimental support with SEM and TEM measurements and data analysis.
- Prof. H.-J. Christ at the University of Siegen for allowing me to use the facilities to conduct fatigue tests and also for giving me the opportunity to develop my practical skills on the TEM. I am also thankful for the guidance and instruction by Dr. Dirk Simon.
- Martin Stenke, Sven Brück, Karo Sedighiani and Dr. Bernhard Völker for help with designing and carrying out fatigue experiments.
- My family, foremost, my parents, who have supported me along the way by many means over and over again.
- My son Alfred and Sara, my beloved wife. She has been the backbone of this whole endeavor, and I have relied on her love and kindness all the way. Not only is she wonderfully beautiful, very cute, and outright aufmüpfig, but also a very smart cookie, who I hope to be around until the end of this earthly existence. I am deeply indebted to her as she strengthened me often and took care of the little guy when I was busy, and would even let me rest when she needed it, too.
- The triune God of the universe for creating a comprehensible physical reality full of wonders, iron, and the incomprehensible beauty of symmetry.

Zusammenfassung

White etching cracks (WECs) sind charakteristische Merkmale für ein frühzeitiges Versagen, das unter Rollkontaktermüdungsbedingungen mit sehr hohen Lastspielzahlen („*giga cycle fatige*“ > 10^9 Lastspiele) auftritt. Diese Problematik betrifft insbesondere Wälzlager, kann mitunter jedoch in ähnlicher Form auch in anderen Anwendungsfällen wie etwa in Bahnschienen auftreten. Der am stärksten betroffene Anwendungsfall sind Wälzlager in Getrieben von Windkraftanlagen. Eine bedeutende Anzahl der betroffenen Wälzlager besteht aus dem hochkohlenstoffhaltigen Standardwälzlagerstahl 100Cr6 und vergleichbaren Güten, die in bainitischem Zustand eingesetzt werden. Kennzeichnend für WECs sind mikrostrukturelle Veränderungen, die als *white etching areas* (WEAs) bezeichnet werden. Dabei handelt es sich um nanokristalline ferritische Bereiche, die unmittelbar an die Risse angrenzen und eine Breite von wenigen 10 nm bis zu einigen µm aufweisen. Das namensgebende weiße Erscheinungsbild im Lichtmikroskop ist der – im Vergleich mit der unveränderten Matrix – gesteigerten Resistenz gegenüber dem Angriff bei der metallographischen Ätzung geschuldet. Nach derzeitigem Kenntnisstand gehen oberflächennahe WECs in Großwälzlagern von nichtmetallischen Einschlüssen aus, die aus dem Herstellungsprozess des Roheisens stammen. Wenn Risse entstanden sind und sich fortpflanzen, kommt es, bedingt durch die Scherspannungsanteile infolge der zyklischen Lasten, zu einer wechselnden Relativbewegung der Rissflächen. Da Risskontakte reibungsbehaftet sind, führt dies bei hohen Lastspielzahlen zu extremen plastischen Dehnungen, die die Zersetzung der initialen Mikrostruktur herbeiführen. In Ermangelung eines detaillierten Verständnisses der mikrostrukturellen Veränderungen auf der Nanoskala ist eine Erklärung des frühzeitigen Versagens basierend auf dem Stand der Technik nicht möglich.

Die vorliegende Arbeit zielt darauf ab, mittels detaillierter mikrostruktureller Analysen einen Beitrag zu leisten, um das grundlegende Verständnis der Entstehung von WECs sowie der durch sie bedingten Schäden zu verbessern. Zu diesem Zweck wurde der Innenring eines Planetenradlagers aus einem Windkraftanlagengetriebe untersucht. Die Charakterisierung erfolgte auf Längenskalen von einigen Millimetern bis zur nahatomaren Größenordnung. Kristallografische Informationen wurden unter Zuhilfenahme der Raster- und Transmissionselektronenmikroskopie ermittelt. Die lokale chemische Zusammensetzung wurde mit spektroskopischen Methoden wie beispielsweise Röntgenspektroskopie und Atomsondentomographie bestimmt. Der Kohlenstoffgehalt in WEAs entspricht, entgegen der üblichen Annahme, nicht der nominellen Zusammensetzung der Legierung. Stattdessen weisen WEAs im Vergleich zum nominellen Gehalt in großen Teilen eine Verarmung an Kohlenstoff auf. In WEAs mit vergleichsweise großen Körnern wurden zudem Volumina mit Abmessungen von einigen zehn nm

gefunden, die aus annähernd reinem Kohlenstoff bestehen. Diese Ergebnisse zeigen, dass eine bedeutende Umverteilung des Materials in WEAs stattfindet. Aus dem Vorliegen von reinem Kohlenstoff innerhalb von WEAs wird geschlossen, dass dies auch an den Rissflächen möglich ist. Die Präsenz von reinem Kohlenstoff an Rissflächen könnte die Reibung zwischen diesen verringern und damit die Rissausbreitung beschleunigen.

Es wurde gezeigt, dass die Korngrößenunterschiede in WEAs in einem inversen Zusammenhang mit dem lokalen Kohlenstoffgehalt stehen. Hohe Kohlenstoffgehalte von bis zu etwa 10 at% stabilisieren dabei Korngrößen von weniger als 10 nm. Es wurde kein Hinweis auf Karbidausscheidungen innerhalb von WEAs gefunden, stattdessen liegt Kohlenstoff gelöst im Ferrit und gesteigert an Korngrenzen vor; beide Werte nehmen mit steigendem Gesamtkohlenstoffgehalt zu.

Die vorliegenden Ergebnisse untermauern die Annahme, dass WEAs stets an beiden Rissflächen vorliegen, selbst dort, wo die Verteilung von WEAs um einen Riss herum nicht symmetrisch ist. Dies stützt die Hypothese, dass die Bildung von WEAs die Präsenz von Rissen voraussetzt. Struktur und Zusammensetzung im Bereich um die Grenzfläche von WEAs und bainitischer Matrix wiesen darauf hin, dass Plastizität vorwiegend dort stattfindet. Dies bedeutet, dass die Zersetzung der Matrix in einem sehr schmalen Volumen von einigen zehn bis zu wenigen 100 nm stattfindet. Diese starke Lokalisierung ist wahrscheinlich der zyklischen Belastung geschuldet. Die vergleichsweise glatte Rissflankenmorphologie von WECs, die sich vom facettierten Erscheinungsbild häufig beobachteter Ermüdungsrisse sowie der Spitzen von WECs unterscheidet, deutet darauf hin, dass Asperitäten durch Rissreibung geglättet werden. Dennoch wird auf der Nanoskala eine exakte Passung gegenüberliegender Rissflanken beobachtet, die darauf hindeutet, dass WECs unter kombinierter Scher- und Druckbelastung teilweise verschweißen und bei Entlastung wieder aufbrechen. Wenn die Rissposition sich hierbei ändert, führt dies zu einer lateralen Risswanderung.

Abstract

White etching cracks (WECs) are a characteristic premature failure phenomenon found in components that experience very high cycle rolling contact fatigue (> 10^9 cycles). The issue is most prevalent in bearings but in a similar form also affects other applications such as rails. The most notable WEC occurrences are related to failures in gearbox bearings of wind turbines. Most of the bearings affected are made from high carbon bearing steel 100Cr6 and similar grades used in a bainitic condition. WECs manifest in microstructural alterations that are called *white etching areas* (WEAs). They are nanocrystalline ferritic regions located directly adjacent to the cracks and extend several tens nm to several µm around WECs. Their white appearance in optical microscopy, which is caused by increased etching resistance compared to the unaltered material, is the defining feature of WECs. The current understanding is that cracks in large scale bearings initiate below the surface in several hundred µm depths at non-metallic inclusions, which are remnants of the steel manufacturing process. Once cracks have formed and propagate, the shear loading also leads to reciprocating sliding movements of the crack surfaces. This leads to severe plastic deformation, which causes decomposition of the initial microstructure resulting in nanocrystalline WEAs. What is currently lacking is a detailed understanding of the alterations at the nm scale and, most importantly, a mechanism-based explanation of the premature nature of WEC related failures.

The present thesis aims at taking steps in this direction by contributing detailed microstructural analyses that aid in understanding the nature of WECs. To this end, a wind turbine gearbox bearing that failed due to WECs is investigated. Characterization techniques are used covering length scales from several mm to near-atomic distances. Analyses of the crystallographic structure are conducted using scanning and transmission electron microscopy techniques. Compositional analyses are performed employing spectroscopic methods such as X-ray spectroscopy and atom probe tomography. The results obtained show that, contrary to the expectation, the composition of WEAs does not equal the nominal alloy composition. In most cases, depletion in carbon is observed instead. Additionally, nanosized pure carbon deposits are found in WEAs with comparatively large grain sizes (several hundreds of nm). These results demonstrate that significant elemental redistribution occurs inside WEAs. The presence of pure carbon is in so far significant, as it renders the possibility of carbon being present at the crack surfaces. A consequence of this could be reduced friction that results in accelerated crack propagation.

Furthermore, it was found that the varying grain sizes inside WEAs are corresponding inversely to the local carbon content. High carbon contents up to around ten at% stabilize grain sizes down to less than 10 nm. No evidence of carbide formation was found inside WEAs. Carbon atoms partition between

grain interior and grain boundaries, both increasing as the total local carbon content increases. The presented investigations furthermore support the assumption that WEAs are always present on both sides of a WEC, even if the appearance on the two sides of cracks is strongly asymmetrical. This asymmetrical distribution is construed as an indication that cracks are a precondition for the formation of WEA. Structure and chemistry at and around interfaces of WEAs and bainitic matrix indicate that plasticity takes place there. This finding indicates that transformation into WEA proceeds from these interfaces into the base material. Structure and chemistry at and around the WEA-matrix interfaces show that decomposition occurs in a narrow region with a width of several tens to a few hundred nm. This confined nature is probably a consequence of cyclic loading. The smooth morphology of WECs flanks as compared to 'conventional' faceted fatigue cracks and even WEC tips indicates that crack surface rubbing is causing a smoothing of asperities. However, crack surfaces are faceted on the nanoscale and still exhibit puzzle-like fits, which is a strong indication that WECs partially reweld during combined compressive and shear loading and reopen during unloading. This mechanism is thought to cause material transfer leading to lateral crack displacement.

Table of Contents

Chapter 1 Introduction

1.1. Thesis structure

The outline of this thesis is as follows:

- In the introduction (Chapter 1), the motivation for this work, and the structure of this document are outlined.
- Chapter 2 starts with a concise summary of the methods and experimental parameters that were used to obtain the results presented in this thesis and is followed by a brief description of the standard bearing steel 100Cr6.
- In Chapter 3, a review of relevant literature regarding rolling contact fatigue (RCF) and white etching cracks (WECs) in bearings is presented.

The central part of the thesis is then comprised of three chapters that are based on three papers, the first of which is published in Acta Materialia, the second is under review with the same journal, and the third is in preparation for submission:

- Chapter 4 describes the carbon (re)distribution in white etching areas (WEAs) that is accompanied by local carbon depletion and attempts to explain the enhanced propagation of WECs as compared to normal RCF behavior.
- Chapter 5 takes an in-depth look at the carbon distribution within WEAs of varying grain size concerning the partitioning between grain interior and grain boundaries. Stabilization of the nanocrystalline structure is discussed in terms of relevant models found in the literature.
- Chapter 6 aims to explain the formation of WEAs through severe plastic deformation due to crack surface rubbing, causing decomposition of the matrix at the interface to the WEA. Particular focus is put on the decomposition of spheroidized cementite precipitates, which provides valuable insights into the chronology of microstructural alterations and the mechanism by which these are brought about.
- This thesis concludes with a summary of its achievements and a critical outlook on the remaining challenges and opportunities and future investigations intended or already being carried out.

1.2. Motivation

This thesis was part of a project motivated by the occurrence of WECs in wind power plant gearbox bearings that create high costs and reduce reliable operation times. Such costs are not only driven by the gearbox price (e.g., ~ 1,360,000 USD, for a 5 MW plant [1]) but also due to the most extended average downtime of all subassemblies in a failure case [2]. Here, a very brief sketch of the importance of wind power is given, which shows that the intention to tackle this failure mode is indeed well justified.

Renewable energy sources are a precondition for Germany (and other countries) to reduce greenhouse gas emissions by 55 % by 2030 (compared to 1990) and zero-emission by 2050. These aims are regulated in the *Climate Protection Act* ('Bundes-Klimaschutzgesetz', KSG) in §1. Wind power is amongst the frontline energy sources, with the current lack of storage capacity. In the first six months of 2020, wind energy contributed 29 % of the total electricity generation[1] (all renewables 51.8 %), which was the most considerable contribution of a single source (including fossil fuels and nuclear power). This development has to be put in the context of the decrease in the total electricity output of 16.7 % between April 2019 and April 2020.

By June 30 of 2019, the installed wind power capacity in Germany was approximately 59.3 GW, with 52.7 GW being onshore (29,456 plants [3]), which is roughly a quarter of the total capacity of 221 GW [4]. In the European Union, the installed wind power capacity was 191 GW [5] with an estimated increase to some 350 GW by 2030 and between 700 and 1200 GW by 2050[2] [6]. The widespread use of wind power in Germany was primarily facilitated through subsidies regulated through the *Renewable Energy Sources Act* ('Erneuerbare-Energien-Gesetz', *EEG*), which came into effect in 2000 and has been modified several times since. In the year 2020, the *EEG* surcharge is 6.756 ct./kWh (2019: 6.41 ct./kWh, which was ~ 21 % of the average price of 30.85 ct./kWh). In Germany, consumer prices are the second-highest in the EU, only superseded by Denmark (by 1 %) [7]. In this context, it is noteworthy that, as of 2018, in Germany, electricity produced by onshore wind turbines (system costs 1500-2000 €/kW), together with photovoltaics, is, on average, the most cost-efficient [8]. The levelized cost of energy (LCOE) for onshore wind is ranging from 3.99-8.32 ct./kWh. Brown coal, the most cost-efficient fossil source for electricity generation, is reported to be at 4.59-7.98 ct./kWh. While the LCOE for electricity from offshore wind turbines (system costs 3100-4700 €/kW) is significantly higher (Germany 2018: 7.49-13.79 ct/kWh), it was recently reported that offshore parks had made significant

[1] https://www.destatis.de/DE/Presse/Pressemitteilungen/2020/09/PD20_352_43312.html (last accessed Nov. 11th, 2020)

[2] "Scenarios are often telling more about the time when they are made than about the future. Although we need some scenarios to assess possible developments." S. Pauliuk

progress in competitiveness with the LCOE of 5.1±0.3 ct./kWh in in 'northern Europe' (2019) [9]. Furthermore, the first successful subsidy-free projects in Germany and the Netherlands are in operation.

It is thus clear that a reliable operation of wind power plants will be a building block for electrical energy supply in the future. The increasing size of wind power plants relies on materials that can reliably operate for up to 30 years, as opposed to currently approved operation times of 20 years [10]. To put this into perspective, the average hub heights of newly installed onshore plants increased from 99 m to 133 m from 2010 to 2018. More importantly, the average rotor diameter increased from 80 m to 118 m [10]. As the torque scales with diameter cubed, this equals a factor of about 4.6, which is also a rough estimation of the gearbox weight increase [11]. A reference design for a 5 MW turbine from 2017 (hub height: 90 m, rotor diameter: 126 m) reports a gearbox weight of ~ 60 t. Although the world's largest wind turbine is a direct drive design for offshore use (*Haliade-X*, GE, 12 MW, operational 2018), there are new design concepts of, e.g., 10 MW offshore turbines in development that make use of gearboxes [12]. Onshore turbines are mostly geared designs, with *Enercon* turbines being an exception. Thus, there is no apparent reason to expect that gearboxes will not be used in wind turbines in the future. The tendency towards larger heights and rotor diameters will directly influence the size of bearings for main shafts and gearboxes. At the same time, larger plants are already less reliable [13]. Failures in general and gearbox failures are not often attributed to specific causes such as WECs in the latter case. Publications and reports generally do not state a cause for the failure of a component [14], sometimes explicitly for reasons of confidentiality [15]. A clear assessment in terms of case numbers for WEC failures is therefore not possible. However, the proposal that has led to the ongoing project received necessary support by industry, showing that a solution is in its interest. The work that is presented in this thesis was conducted as part of this project funded by the *German Federal Ministry of Education and Research* (*BMBF*) under the initiative 'materials research for energy transition'[3]. The project aims to provide new insights into the mechanisms governing WEC phenomena by employing state of the art microscopy techniques to describe characteristic chemical and structural features of WECs. An improved understanding of the mechanisms that govern WEC-related failures is a precondition for developing successful solutions. This project aims to pave the way for the development of WEC resistant materials. Therefore, research that can assess the fundamental questions related to the WEC phenomenon is necessary to accommodate the continued immense contribution of wind power to electricity generation and further enhance it with both cost and resource efficiency.

[3] https://www.bmbf.de/foerderungen/bekanntmachung.php?B=851 (accessed Nov. 6, 2020) original title 'Materialforschung für die Energiewende'. *Energiewende* refers to Germany's ongoing efforts to transition from fossil and nuclear fuel-based to renewable energy generation.

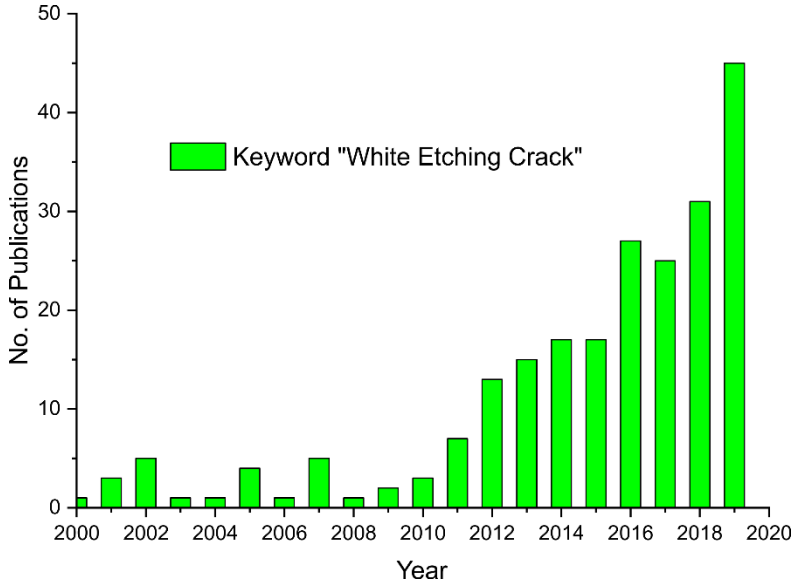

Figure 1.1: Number of peer-reviewed publications under the keyword 'White Etching Crack' listed in the Web of Science® from the year 2000 until the end of 2019.

In this context, it is helpful to look at the research activities in the past decade. The number of peer-reviewed articles on WECs being published has been significantly increasing over the last ten years (Figure 1.1). However, if one seeks the comparison to the numbers published on 'hot topics' like, e.g., high entropy alloys (1,514 vs. 45 in 2019)[4], it shows that WECs are more of a niche topic and more effort should be made to fundamentally understand the phenomenon so that the service life of components susceptible to WECs can be improved. A critical issue to address is that most of the studies listed in the *Web of Science*® are in either or both of two categories, 'Mechanical Engineering' and 'Materials Science'. Besides these two central contributing communities, tribologists and chemists (those occupied with lubricants) are also conducting research related to WECs. This account provides an accurate picture of the intricacies of the issue as it is at hand. It concerns the materials and the mechanics' community, additionally touching on other professions, all this with accompanying disagreements regarding the cause of the problem and its potential solutions. Besides the complexity of the phenomenon itself, part of the challenge is that researchers of different backgrounds approach WEC phenomena in starkly different ways. Due to this complexity, it is vital to maintain a broad perspective to understand the underlying mechanisms of WEC formation and propagation. It is unlikely that any solution can be put forward solely based on the mechanical, material, or chemistry approach side of things. Instead, a combined assessment of loading conditions, material properties, and lubricant

[4] This comparison is not strictly quantitative as the topic is vast, but gives an impression of the comparatively low number of materials researchers dealing with the topic.

influences is undertaken because WECs are most likely a system ‘property’ and do not occur when one variable is changed.

The most comprehensive review of the WEC phenomenon was done by Evans in two lengthy publications in 2012 and 2016 [16, 17], giving an excellent overview of microstructural characterizations and formation hypotheses. With this being said, investigators rarely elucidated the structure *and* the composition on scales that resolve features of the microstructural changes associated with WECs and decomposing base material sufficiently to draw conclusions, which can potentially advance the understanding of the underlying mechanisms or root causes. Herein lies another problem in that most WEC formation hypotheses are not directly set in relation to the foundational problem, i.e., *by which mechanism do WECs cause early failures*? This question is the starting point for the presented work showcasing extensive atom probe tomography and electron microscopy analyses that provide a more in-depth insight into the composition and microstructure of WEAs with varying grain sizes and carbon contents and the interface of WEA and initial material down to the near-atomic scale. Furthermore, this work attempts to link these observations to the premature nature of failures, which are the characteristic of WECs.

Chapter 2 Materials and Methods

2.1. Experimental methods

Sample preparation

Samples were cut from the gearbox bearing inner ring as axial and tangential cross sections by electrical discharge machining. Only some samples were embedded in phenolic resin because for specific analyses, like carbon content measurements, this can introduce carbon-containing material into the gaps formed by cracks. Preparation of all except one investigated crack network was conducted using standard metallographic techniques and carried out manually. Grinding and diamond polishing were followed by a finishing step using colloidal silica suspension. The time varied depending on the type of subsequent analyses. As some microstructural alterations are prone to be preferentially attacked, it can be as short as 20 s. One radial cross-section for electron probe microanalysis (EPMA) mapping was prepared by argon-ion cross-section polishing in a HITACHI E-3500 ion milling system at 6 kV acceleration voltage and 350-400 µA discharge current to avoid carbon contamination.

Scanning electron microscopy and focused ion beam preparation

Scanning electron microscopy was used for imaging and spectroscopy: Backscatter electron (BSE) and secondary electron (SE) imaging was performed on a Zeiss Merlin and Sigma SEMs at acceleration voltages of 20 and 30 kV and currents of 2.0-3.0 nA. Energy-dispersive X-ray spectroscopy (EDS) measurements were performed at 15 kV. Wavelength dispersive X-ray spectroscopy (WDS) EPMA maps were obtained utilizing a JEOL JXA-8100 microprobe analyzer at an acceleration voltage of 5 kV and a dwell time of 1 s. A cooling trap was used to reduce the deposition of carbohydrates through the electron beam. Electron backscatter diffraction (EBSD) orientation measurements were conducted using a Zeiss Sigma SEM and analyzed with the Software TSL-OIM 7.

Specimens for atom probe tomography (APT) and transmission electron microscopy (TEM) analyses were prepared as site-specific lift-outs with FEI Helios NanoLab 600 & 600i dual-beam SEM-Ga-FIBs.

Atom probe tomography

APT measurements were carried out on Cameca LEAPs (3000HR, 5000XS and, 5000XR) at temperatures of 60-70 K with detection rates ranging from 0.5 to 2 %. Measurements were carried out in voltage (pulse fraction 15%) as well as in laser mode (laser energies 20-30 pJ) with pulse rates of 200 and 250 kHz. Data analysis was carried out using the Imago visualization and analysis system (IVAS) 3.8.4. Compositions were quantified using the built-in peak decomposition algorithm in the

IVAS software. Sub volumes encompassing specific features or phases were individually ranged and quantified.

Transmission electron microscopy

Electron energy loss spectroscopy (EELS) maps were acquired on a probe-corrected FEI Titan Themis at 300 kV equipped with a Gatan Quantum ER spectrometer and analyzed using DigitalMicrograph®. All other transmission electron microscopy (TEM) investigations utilized a JEOL JEM-2200FS equipped with an Omega energy filter at 200 kV. The NanoMegas® ASTAR system was used for data acquisition of diffraction patterns and indexing. Orientation mapping was carried out in nanobeam mode with a nominal probe size of 0.5 nm without precession. The nominal step size was 1.25 nm. Indexing and correction for 180°-ambiguities were performed in ASTAR.

2.2. 100Cr6 bearing steel

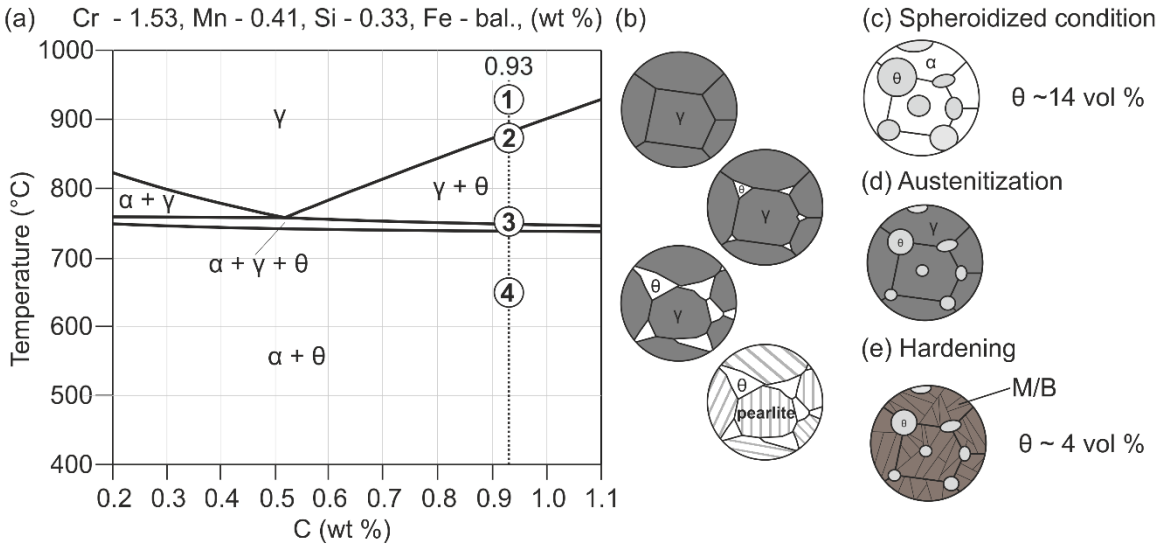

Figure 2.1: Pseudo binary phase diagram of 100Cr6 with the composition of the gearbox bearing ring and schematics of the (equilibrium) microstructures at different temperatures: (a) is a section of the phase diagram with carbon concentration on the x-axis (α – ferrite, γ – austenite, θ – cementite); (b) shows schematics of the microstructure evolution during (slow) cooling from the austenite regime with precipitation of proeutectoid cementite starting at grain boundaries and finally transformation into pearlite (depiction of the three-phase field is omitted). (c) Shows the microstructure at the end of the spheroidization treatment as globular pearlite, (d) depicts the condition of the material during austenitization and the final condition after hardening (M/B: martensite/bainite).

The main sample investigated in the presented work stems from an inner ring of a two-row wind turbine gearbox roller bearing made from the high carbon bearing steel 100Cr6 (DIN EN ISO 683-17, similar grades are SAE/ASTM/AISI 52100, SUJ2, 1.3505) in bainitic condition. A second sample was also

included in the investigation of the carbon redistribution in Chapter 5. This sample is a washer with martensitic microstructure from a thrust roller bearing fatigued in an FE-8 test rig [18]. Due to its high hardness and comparatively low price, 100Cr6 bearing steel is the most widely used steel in bearing applications [19].

Table 2.1: Compositional ranges of alloying and some impurity elements in 100Cr6 bearing steel according to DIN EN ISO 683-17 and compositions of analyzed bearings determined by optical emission spectroscopy (OES).

		Cr	C	Mn	Si	S	P	O
Standard	wt%	1.35-1.6	0.93-1.05	0.25-0.45	0.15-0.35	< 0.015	< 0.025	< 8 ppm
Gearbox bearing inner ring	wt%	1.54	0.93	0.41	0.334	0.0054	0.0057	-
	at%	1.59	4.16	0.40	0.64	0.0091	0.01	-
Thrust roller bearing washer	wt%	1.47	0.99	0.35	0.25	0.015	0.025	-
	at%	1.52	4.43	0.34	0.48	0.015	0.025	-

The compositional ranges for the main alloying and important impurity elements according to the standard and the measured compositions of the investigated bearing components are listed in Table 2.1. Figure 2.1 (a) shows a section of the pseudo-binary phase diagram for the measured composition of the gearbox bearing ring. Figure 2.1 (b) schematically shows the evolution of the near-equilibrium microstructures upon slow cooling from the austenite region. After hot rolling, the steel conventionally receives a so-called spheroidization treatment around A_{c1} (~ 750 °C). Several methods with different temperature profiles over several hours and result in a near-spherical shape of roughly 1 µm large cementite precipitates [20]. During this treatment, a significant amount of chromium partitions into the spheroidized cementite ($(Fe,Cr)_3C$ with ~12 at% Cr), leaving approximately two-thirds of the total chromium content within the iron matrix. Figure 2.1 (c) illustrates the resulting microstructure with spherical cementite. During austenitization (at ~ 850°C), the precipitates partially dissolve (Figure 2.1 (d)). Large scale bearings (wall thickness > 25-30 mm wall thickness) are then cooled to temperatures in the range of ~220-270 °C and held for up to several hours, resulting in a microstructure of lower bainite. During this step, spheroidized precipitates form a shell of Fe_3C around the $(Fe,Cr)_3C$ precipitates. In the final state, they bind around one-third of the carbon contained in the alloy. Lower

bainite is formed as described above, consisting of bainitic ferrite with intra-sheave cementite and ε carbide [21]. Figure 2.2 depicts features of the bainitic microstructure from the wind turbine gearbox bearing that were investigated in this work. Figure 2.2 (a), (b), and (c) are BSE, SE, and STEM bright-field images, respectively. Alternatively, components of small dimensions made from 100Cr6 are used in a through-hardened martensitic condition. It is achieved by quenching from ~850°C in water or oil and typically a single tempering step at ~140-180°C resulting in a final hardness of around 57-59 HRC [22]. The microstructure after quenching and tempering consists of a mixture of nano-twinned plate as well as lath martensite with a retained austenite content of typically ~6-14 vol% [19, 22, 23]. During tempering, transition carbides and cementite precipitate.

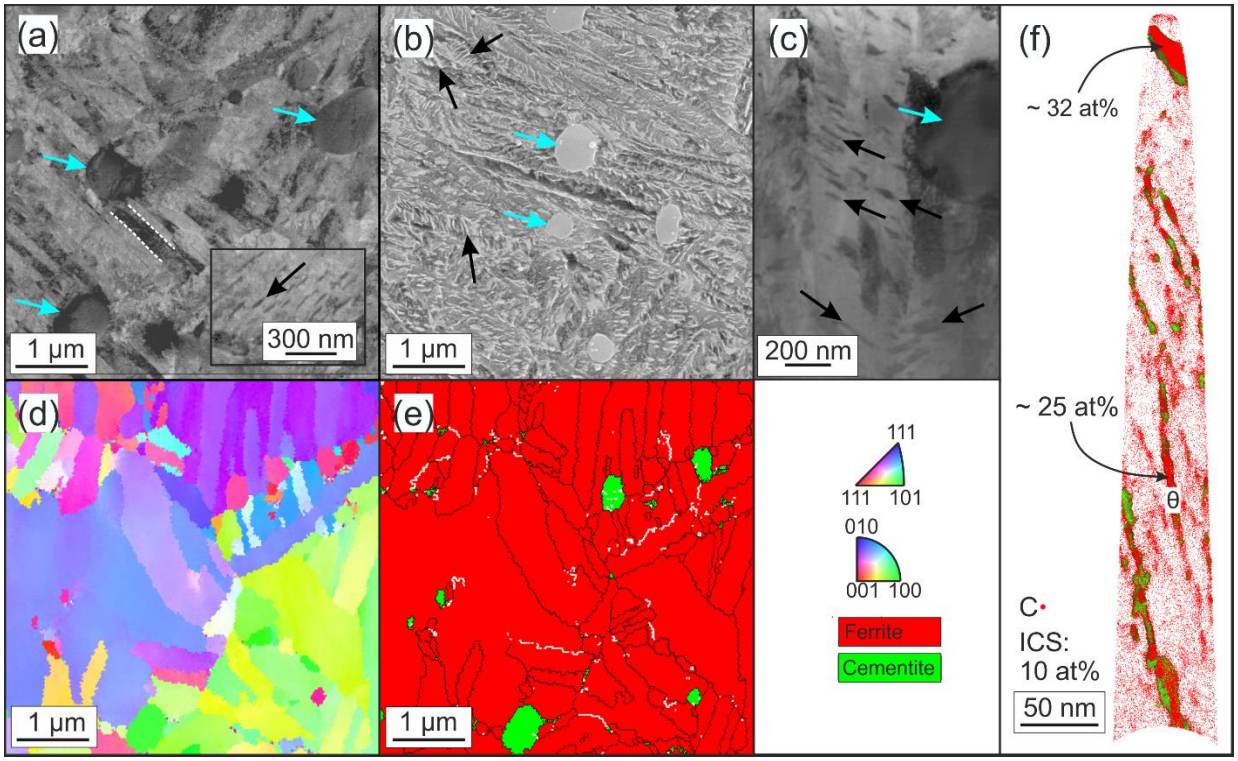

Figure 2.2: Initial microstructure of the investigated wind turbine gearbox bearing inner ring. 100Cr6 steel in bainitic condition. The BSE- (a) SE- (b) and STEM-images (c) are showing the microstructural features. Some subunits of bainitic ferrite (α_b) are indicated by dashed lines in (a) and (c). Cyan arrows mark Cr-rich spheroidized cementite while white arrows mark bainitic cementite. (d) Inverse pole figure and (e) phase map with grain boundaries (3-14° misorientation in white > 15° in black). The APT tip in (f) shows the presence of intra-sheaf carbides with carbon contents of ~ 25 at% (θ, cementite) and ~ 32 at% (transition carbide).

The spheroidized $(Fe,Cr)_3C$ precipitates (cyan arrows) and intra-sheave bainitic carbides (black arrows) are embedded in the bainitic ferrite matrix (Figure 2.2 (a)-(c)). Several subunit boundaries are marked by dashed lines. Such subunits are clearly visible in the inverse pole figure map in Figure 2.2 (d) and

(e), which also show their heterogeneous size distribution. The spatial resolution of electron backscatter diffraction (EBSD) is not sufficient to resolve bainitic carbides. Figure 2.2 (e) is a phase map, high angle grain boundaries (> 15°) are outlined in black, low angle grain boundaries in white. The APT tip depicted in Figure 2.2 (f) shows bainitic carbides (cementite and transition carbides).

Table 2.2: Mechanical properties of 100Cr6 and 52100 bearing steel with similar composition and heat treatments ([24]and [22]).

Condition	Yield strength (MPa) [24]	Ultimate tensile strength (MPa) [24]	Hardness (HRC) [22]	K_{IC} (MPa·m$^{1/2}$) [22]	ΔK_{th} (MPa·m$^{1/2}$) R = 0.5 [22]	Endurance limit (MPa) R = -1 [22]	Retained austenite (vol%) [22]
Martensite*	1476	2149	62.5	16.9	4.3	926	12
Bainite**	2058	2476	58.5-59	17.8	8	783	< 1

*[24] austenitization: 860 °C/ 20 min, oil quench 50 °, tempering 160 °C/ 1.5 h

[22] austenitization: 860 °C/ 20 min, oil quench 60 °, tempering 180 °C/ 2 h

**[24] austenitization: 860 °C/ 20 min, 230 °C/ 6 h, [22] austenitization: 860 °C/ 20 min, 235 °C/ 5 h

Generally, the mechanical properties of bainitic and martensitic condition are similar. An overview of the mechanical properties of two conditions obtained from the same batch is given in Table 2.2. While the martensitic condition has higher hardness, the bainitic condition is superior in terms of tensile and yield strength. Although the critical values for instable crack growth (K_{IC}) are similar, the threshold value for crack propagation is roughly twice as high for the bainitic condition. Under conventional push-pull fatigue conditions, the martensitic condition is superior, which is probably related to the transformation of retained austenite. Both conditions have comparably low resistance against crack propagation in mode I if compared to other steels like case hardeners that can reach values in the range of ~70-120 MPa·m$^{1/2}$ (AISI 8620 [25]).

Chapter 3 Literature review – Rolling contact fatigue and white etching cracks

The WEC phenomenon derives its name from the white appearance of altered microstructure decorating WECs in optical images after etching with nital. The term used to refer to the altered microstructure is 'white etching area' (WEA). It consists of nanocrystalline ferrite with grain sizes ranging from several 100 nm down to as small as 3-20 nm [26-30]. An example of a WEC within a bainitic microstructure is shown in Figure 3.1. The optical image in Figure 3.1 (a) demonstrates the name-giving effect. Figure 3.1 (b) is a BSE micrograph of the region indicated in (a) by a white rectangle. In some regions, the WEA appears homogenous at the given magnification (white arrow in (b)). The inset on the left-hand side shows a TEM bright-field (BF) image demonstrating the extreme grain refinement in a WEA.

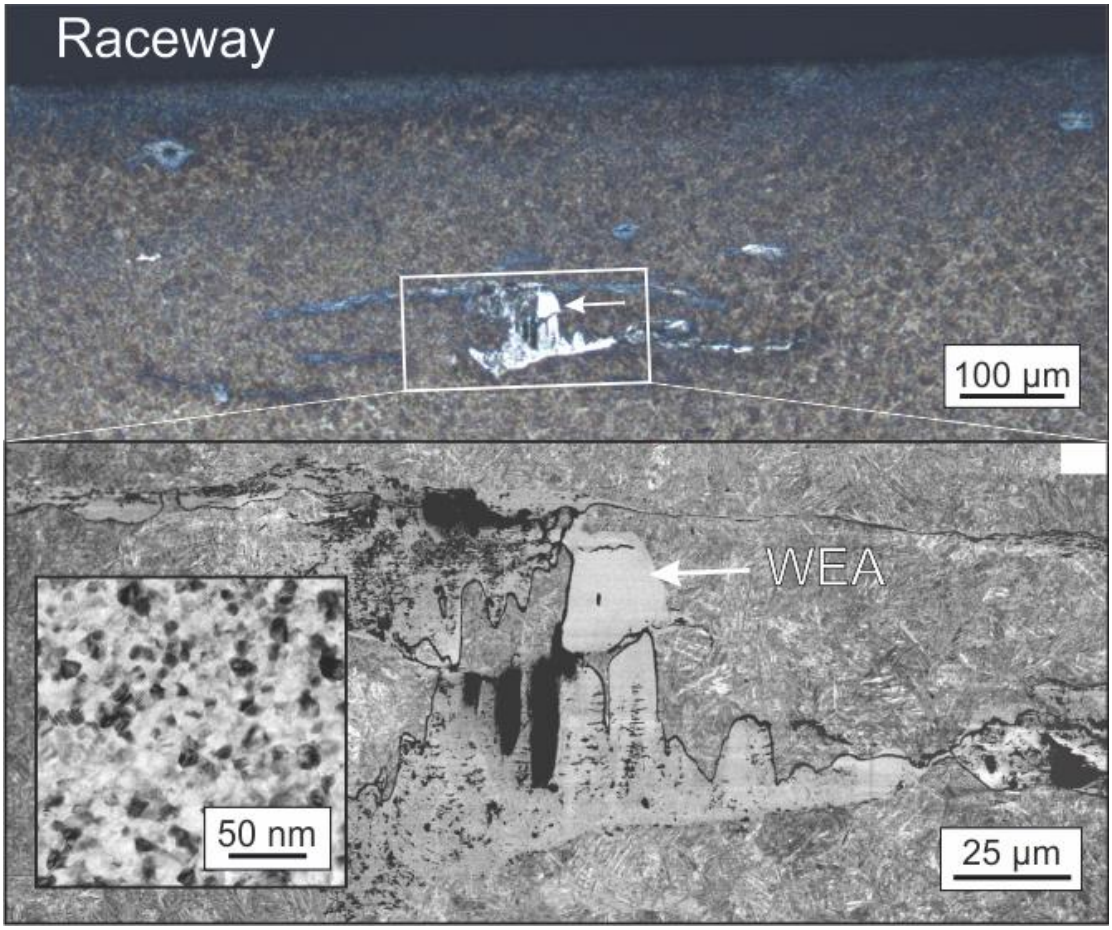

Figure 3.1: Example of a WEC in a bainitic bearing in a depth of ~200-300 µm below the raceway. Subfigure (a) is an optical micrograph of a nital etched sample and (b) a BSE image of the marked region after repolishing. While in (a) the WEA appears white, in (b) large region have homogenous contrast (white arrow) since grains are not resolved at this magnification. The inset on the left shows a TEM BF image of an average grain size below 20 nm WEA. The over rolling direction is normal to the image plane.

This introductory section will address classical rolling contact fatigue, followed by a review of crack initiation around non-metallic inclusions, so-called *butterflies*, and a thorough treatment of WECs and their potential drivers and initiation mechanisms. Competing views about those issues found within the relevant literature are presented. Finally, shear mode crack propagation will be discussed briefly to frame the outcomes in Chapter 4.

3.1. Rolling contact fatigue

While WECs are a rolling contact fatigue (RCF) phenomenon, they differ significantly from the usual failure modes. RCF without WEC related failures is already a complex phenomenon and shall be considered to clarify similarities and distinctions of 'conventional' RCF failures and those caused by WECs. Although not all aspects of conventional RCF are directly related to WEC induced failures, some considerations help categorize WECs and recognize key differences. Therefore, a brief overview is given in this section.

RCF is a succession of loading events caused by rolling elements. In the case of bearings, which are used in wind turbine gearboxes, high strength steels are used exclusively[5]. Under ideal conditions, actual contact of the bodies, hence friction, is almost entirely avoided through lubrication, which separates the bodies so that no asperity contact takes place. Although this is generally the case for proper lubrication conditions, some traction is still being exerted on the raceway [31]. Each over rolling event is a single load cycle that causes a multiaxial stress field, which is usually approximated by Hertzian contact theory [32]. The displacements that are consequences of the acting stresses are qualitatively illustrated in Figure 3.2 (a): the volume below the contact is stressed compressively. To the left and right, the volumes are sheared in opposite directions. Calculation of these stresses by Hertzian theory predicts maxima of both shear and von Mises stresses inside the contacting bodies. This is illustrated in Figure 3.2 (b) and (c), which show lines of equal stress under Hertzian line contact (from [33]). Taking into account the viscosity of the lubricant assuming so-called elasto-hydrodynamic (EHD) lubrication, the actual pressure and hence the stress distribution is even more complex, exhibiting a spike at the outlet of the lubricant from the contact region [34]. Usually, though, the simplified case is used to describe the subsurface stresses because the material's inhomogeneity more strongly influences them than by small deviations in the pressure distribution [31].

[5] Some small and medium-sized single-row deep groove ball bearings and cylindrical roller bearings (< ~200 mm bore diameter) are available as so-called hybrid bearings. In such bearings, steel rings are used in conjunction with ceramic (silicon nitride) balls, which have superior properties in highly corrosive environments, at extreme velocities, and under poor lubrication conditions.

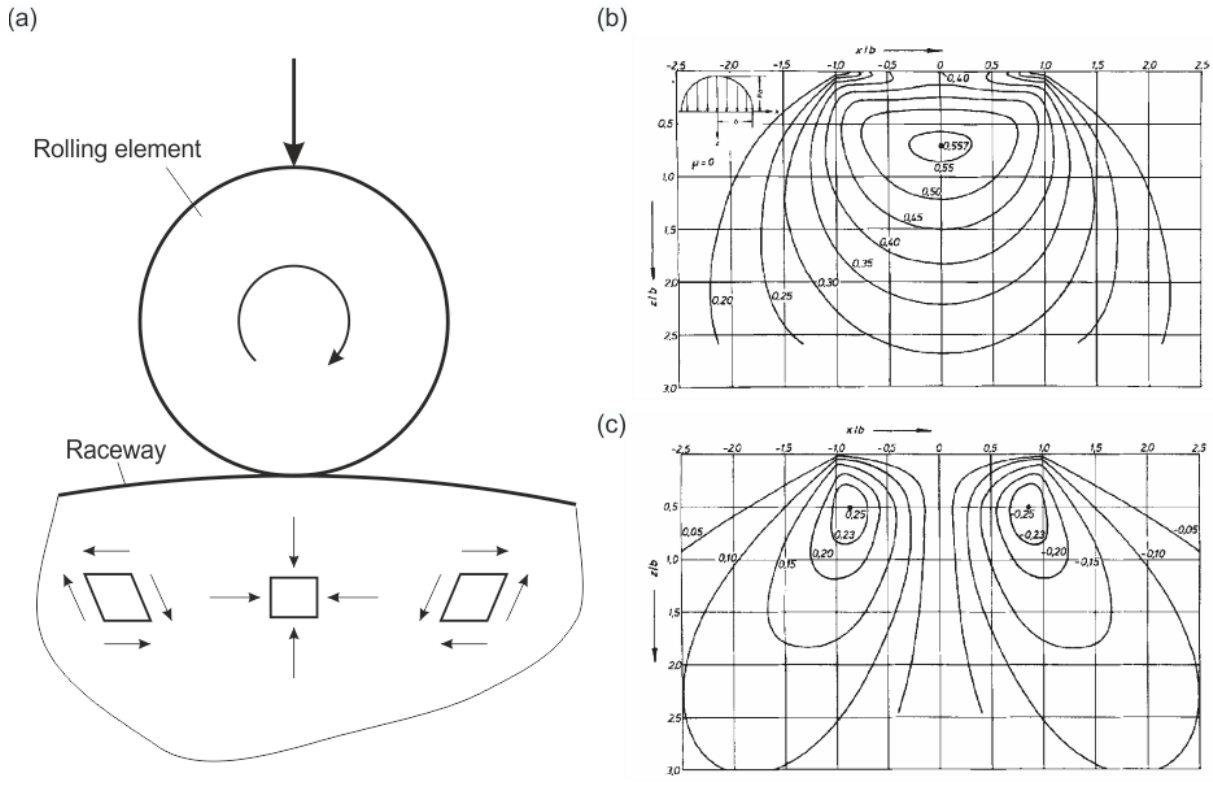

Figure 3.2: (a) Illustration of the loading scenario in rolling contact fatigue. The volume underneath a rolling element is under compressive stress, while the volume ahead additionally sees a forward shear, and the one behind is sheared in the opposite direction. Upon one over rolling event, the shear stress is hence reversed. (b) and (c): Lines of v. Mises stress and equal alternating shear stress distribution under frictionless Hertzian line contact under the assumption of an isotropic, elastic solid. Stresses are normalized by the contact pressure p_0 and depth (z) and tangential direction (x) by the contact radius. The maxima are underneath the surface, with the von Mises maximum being slightly deeper inside the bodies than the shear stress maxima. (Figures (b) and (c) from [33], used with permission of John Wiley and Sons).

As can be seen from Figure 3.2, RCF in general and in bearings, in particular, is significantly dissimilar to classical fatigue, which is often investigated with simple (i.e., uniaxial) loading scenarios actualized by rotating-bending or compression-tension testing [31]. In addition to the multiaxial stress state, hydrostatic stress components are significant [35], and because of minute contact areas, only comparatively small volumes in the subsurface region of the material are strongly affected [31]. In terms of microstructural development of the material, conventional RCF in lubricated bearings can be divided into three stages as described by Voskamp [36]: 1 shakedown, 2 steady-state and, 3 material softening; the latter leading to crack initiation and finally failure by spalling. Stage 1 is a very short period (~1000 revolutions) of work hardening response resulting in residual stresses. Stage 2 is mostly in the elastic regime where no noticeable alterations inside the material occur. Finally, in stage 3, the microstructure softens, which manifests in phase transformations, texture formation, and decay of

residual stresses [37]. In stage 3, multiaxial stresses cause localized microstructural decay accumulating in the most severely stressed volume resulting in a plastically deformed zone underneath the raceway. Microstructural alterations in the form of the so-called high and low-angle white bands form through dislocation activity, accompanied by carbon redistribution. Softening first results in micro yielding followed by failure through crack formation parallel to the rolling direction, propagation thereof, and finally spalling. The crack propagation is aided by the mentioned texture formation [35] that leads to in-plane compressive stresses both parallel and, most importantly, perpendicular to the rolling direction and hence a tensile component in the direction of the surface normal [36]. Lifetimes of bearings are often expressed in probabilistic terms using the so-called L_{10} lifetime, which describes the number of revolutions that 90% of bearings will endure without failure. This description is based on the early work of Lundberg and Palmgren [38], who used Weibull distributions to describe the results of large numbers of experiments to express the failure probability of bearing inner rings mathematically. As this approach and many others built on it are not related to the physical mechanisms taking place inside the material, other methods were developed that attempt to base the lifetime prediction on models of crack initiation and propagation (for an overview, see [31]). Numerical simulations of RCF, taking an emulated microstructure into account, were used to obtain a failure probability distribution, which matched well with a Weibull distribution obtained in a previous study by Raje et al. [39]. This type of mechanism-based modeling approach was continued in [40], employing a 3D finite element grain structure coupled with damage mechanics. From a real materials perspective, limitations are evident since the microstructural evolution through stage 1 to 3 is not well enough understood to be described with sufficient precision through modeling. Part of the challenge is that RCF is a very high cycle fatigue (VHCF) phenomenon, often exceeding 10^8 loading cycles in bearing applications, limiting the accessibility through simulations.

3.2. Butterflies and their formation around non-metallic inclusions

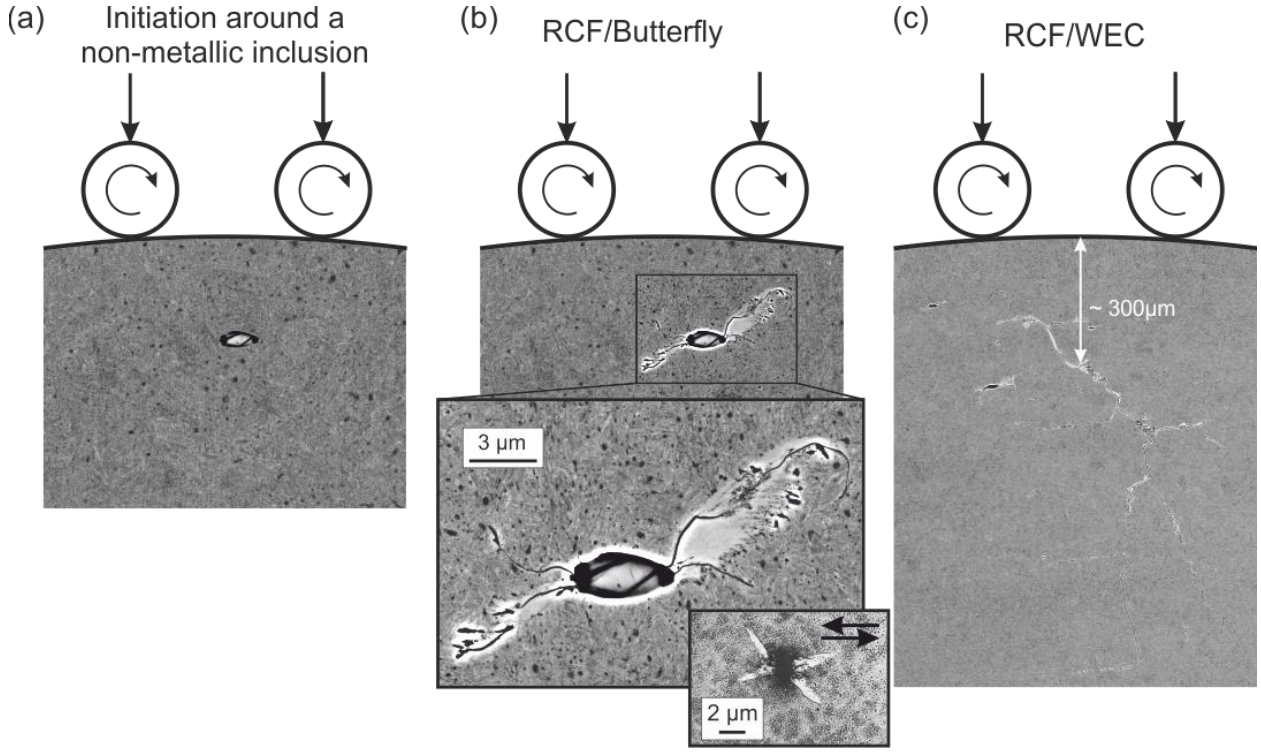

Figure 3.3: Schematic evolution of WECs: Initiation at a non-metallic inclusion (a) leads to the formation of a two-winged butterfly (b), which upon growth evolves into a WEC-network (c). Note the inset in (b), which elegantly shows that upon reversal of the rolling direction, a four-winged butterfly forms (inset in subfigure (b); from [41], used with permission from Elsevier).

So far, the description of RCF did not account for the real heterogeneous microstructure of the material. Both bainitic and martensitic microstructures are anisotropic on the micro to nanoscale. These properties result from segregation, local crystallography, incomplete transformation, or interfaces, and most importantly, comparatively large defects in the form of non-metallic inclusions (see Figure 3.3 (a)), which have a size of a few to several tens of µm. These non-metallic inclusions are remnants from manufacturing processes. They have detrimental effects on the lifetime as they can cause failures that differ from those described in the prior section. It has been known for approximately seven decades that so-called butterflies form in the subsurface region in bearings subjected to RCF loading [42] around non-metallic inclusions [43] (in *super-clean* aerospace alloys, initiation can also occur at carbides [44]). In the characteristic appearance, butterflies exhibit two main cracks emanating as wings at about 45° to the raceway surface on opposite sides of the inclusion, as illustrated in Figure 3.3 (b) – the upper wing points in the over rolling direction. Tricot et al. showed that the direction of over-rolling plays a role in butterfly formation. Upon reversing the over rolling direction, butterflies with four wings were formed [41] (see inset in Figure 3.3 (b)). The cracks emanating from non-metallic inclusions are

typically bordered by WEA, mostly on one crack side with a relatively sharp transition to the matrix on the opposite side of the crack. The opposite side of the WEA wing is often more serrated and less clearly defined. The wing length is on the order of some tens to a few hundred µm [16]. Butterflies have been experimentally investigated by TEM since the early 1970s [27, 41] and more recently using site-specific FIB lift outs [26, 28, 45] in combination with TEM and ion imaging. These investigations have shown that the WEA wings bordering the crack on one side and the matrix on the opposite side consist of nanocrystalline ferrite with a wide range of grain sizes down to ~3 nm [26] (Figure 3.3 (b)), with voids frequently being found around cracks inside WEAs. No apparent difference between WEAs at butterfly wings and those found in mature WEC networks could be found, neither within the cited literature nor in the work conducted for this thesis.

Bearing steel cleanliness has significantly increased over the past decades. The average oxygen content in SEA 52100 was reported to have decreased from 11 to 5 ppm from 1986 to 1996 [46]. The sequence of vacuum induction melting (VIM) followed by vacuum arc remelting (VAR) also reduced the amount of sulfur from 65 to 7 ppm [47]. Hence, the decreasing number and size of non-metallic inclusions result in prolonged RCF lifetimes [36]. Nevertheless, inclusions such as TiN, MnS, or $(Al,Ca,Mg)_xO_y$ are still present and act as initiation sites for butterflies and small cracks [48]. Initiation is caused by the elastic incompatibility of both hard and soft inclusions with the matrix under cyclic stresses. Given identical size and shape, inclusions with stiffness higher than the matrix are most effective in initiating butterflies [49]. Inclusion size, shape, and orientation with respect to the loading direction play an important role. Murakami [48] introduced the projected area of a defect as a parameter to quantify the likelihood of crack initiation for a specific inclusion under a given load. Based on investigations of the microstructure of a butterfly in [28], the initiation is described as a sequence of debonding at the interface, followed by deformation of the matrix, which then leads to microcrack initiation. According to Lewis and Tomkins [50], the following propagation takes place in mode I (crack opening) due to tensile stresses around inclusions. Mode I propagation fades out as a crack propagates away from the region where the stress field is governed by the inclusion. Propagation comes to a halt when the stress intensity factor (SIF) falls below the threshold for mode I crack propagation [50]. A further aspect in regards to the likelihood of butterfly formation and the shape (wing size ratio) is the depth of inclusion ([51] and citations in [49, 52]). Regarding the depth of initiation with respect to the positions of maximum shear, different views are held amongst investigators. Evans holds that initiation is not happening at the location of maximum shear stress ([16] and citations therein). Conversely, Moghaddam et al. claim that butterflies form first at this depth position [49], taking into account surface traction in the calculation of the shear stress leads to a non-symmetrical shear stress distribution. They

derived a *butterfly formation index* that matches well with experimental findings (data from [53] shown in [49]). This is noteworthy since based on this calculation approach of the shear stress in their further work [52, 54], they were able to correctly predict the two-winged shape of butterflies and the experimental observation that the upper wing points into the direction of over rolling (compare Figure 3.3 (b)).

The formation of WEAs is attributed to the interaction of crack surfaces (crack surface rubbing), which leads to the decomposition of the initial microstructure by severe plastic deformation (SPD), resulting in nanocrystalline ferrite [55]. The accumulated high local strains and defects probably cause some amount of low-temperature recrystallization [28]. The exact mechanisms, though, are not well understood. The lifetime governing role of initiation and propagation RCF seems to be different from conventional fatigue with initiation at subsurface inclusions. For the latter case, it is well documented that crack initiation consumes most of the lifetime [56-59]. Typical RCF experiments reach 10^8 load, cycles with butterflies appearing before 10^5 cycles. On the other hand, butterflies are often found not to propagate. Investigations by Makino et al. [60] demonstrated early long crack initiation under RCF conditions in the presence of artificial defects (holes with a diameter of 15 µm and 200 µm depth) using synchrotron tomography. Such indents are surface defects and might therefore be understood to be of limited use for reasoning in support of early subsurface initiation. However, since non-artificial surface initiation is related to high amounts of slip, tensile residual, or hoop stresses – all of which were absent in these experiments – and horizontal crack initiation away from the surface was observed, one can convincingly argue that early initiation at subsurface inclusions is possible. This conclusion is supported by results from Lankford, who provided insight into the debonding of inclusion and early initiation of cracks demonstrating the start of debonding during the first load cycle [61, 62].

3.3. White etching cracks

WECs are associated with premature failures, which means they occur earlier than the classical probabilistic description of RCF by Lundberg-Palmgren [38] predicts, typically after 5-10 % of the L_{10} lifetime [16]. This deviation means that by definition, WECs are not ‘normal’ RCF failures. WECs grow independent of the microstructure as long cracks and occur in a variety of morphologies with preferred crack orientations mostly in the horizontal direction (i.e., parallel to the raceway surface) and to a lesser extent in the vertical direction when developed networks are linking together. Furthermore, varying volumes of WEA are present around cracks, and they occasionally exhibit significant grain size variations. Some researchers report that no preferred orientation is present in nanocrystalline WEAs

[28, 63], while others mention a variation in the intensity of diffraction rings from TEM investigations [64]. A lack of accessible tools likely causes these contradicting assessments since EBSD cannot resolve nanocrystalline WEA structure with grain sizes as small as 5 nm. Non-random textures were found in WEA regions that underwent significant coarsening [65]. Figure 3.4 shows BSE images illustrating the appearance of WECs. Figure 3.4 (a) shows a WEC that has propagated across bainite subunits, demonstrating that propagation is not governed by interaction with microstructural features such as grain boundaries. Figure 3.4 (b) and (c) provide a comparison of a mode I fatigue crack in a martensitic 100Cr6 compact tension shear (CTS) specimen and a WEC – the differences are evident. While the mode I crack in (b) is serrated, exhibiting sharp kinks, the WEC, the crack in (c) is very smooth, which is resulting from crack surface rubbing that levels asperities.

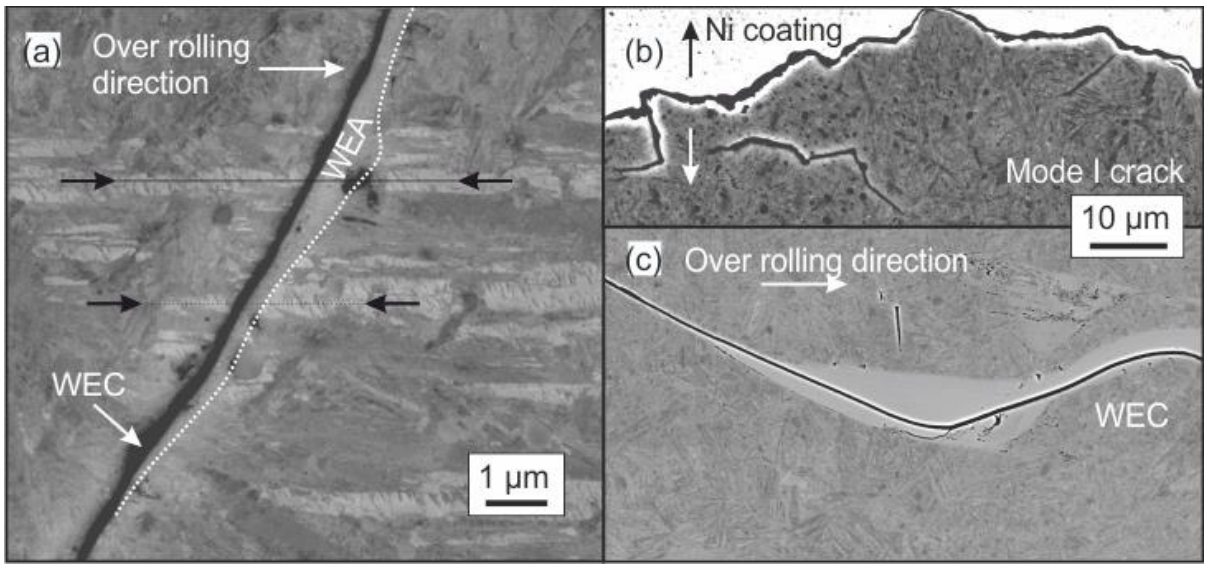

Figure 3.4: BSE images of crack morphologies: (a) shows a WEC that has propagated across bainite subunits (black arrows), indicating that crack propagation is governed by long-ranging stresses. Cracks in (b) and (c) are depicted at the same magnification; (b) shows a flank of a serrated mode I fatigue crack from a martensitic 100Cr6 compact tension shear (CTS) specimen (black and white arrow indicate the loading direction) and (c) a smooth WEC. This demonstrates the different morphologies due to different loading conditions.

The previously mentioned aspects (crack morphology, WEA structure, crack propagation) are likely related to special environmental, loading, and material conditions differing in each application or testing scenario [16, 17]. Three key questions will be addressed in the following sections: first, if subsurface or surface initiation is most relevant, second, the question regarding the chronology of events, i.e., which comes first: WEA or crack? And third, if hydrogen is the root cause or just a driving influence? Finally, the role of carbon will be briefly addressed.

3.3.1. Surface vs. subsurface initiation of WECs

It is contested as to whether typical WECs initiate at the surface or in the subsurface [17], with experimental evidence existing for both cases. In wind turbine gearboxes, bearings can experience complex loading scenarios, including overloads. Regular operation under moderate conditions results in contact pressures in the range of 1200-1600 MPa [66], which induce stresses inside the material below the conventionally assumed fatigue limit. But due to transient conditions, which can result from starting and breaking [11], emergency stops, etc., peak loads above 2500 MPa with strong non-uniform vibrations were observed [66]. In the same publication, successful 'production' of surface-initiated axial WEC in a large scale test rig are reported, brought about by a combination of excessive peak loads (< 3500 MPa) and vibrations. Crack propagation is assumed to be driven by a tribo-corrosive attack. However, contrary to this study, others came to the conclusion that no excessive loading was present in monitored bearings in wind turbines (cited in [17]). A further example of surface initiation was also reported for angular contact ball bearings fatigued on test rigs with and without hydrogen charging [67]. Like the above, this was reported to be followed by lubricant ingress leading to corrosion driven crack propagation. Initiation at the surface can also be related to tensile stresses in the circumferential direction. In inner rings, hoop stresses from tight interference fits ensure no relative movement between the bearing ring and shaft can occur. Waviness at inner bearing ring seats was also shown to be the cause of tensile stresses near the raceway [68]. Finite element analyses taking the waviness into account, successfully predicted the location of axial surface cracking in subsequent tests. The resulting cracks also exhibited WEA formation.

Despite these reports, in recent years, the consensus has grown that WECs not only can be initiated purely subsurface and form extended networks but that this mode is the dominant one in premature failure of wind turbine bearings [69]. The subsurface nature for different bearing types, from service applications and laboratory tests alike, is evidenced by 3D investigations of whole WEC networks by serial sectioning methods using mechanical grinding [70] as well as FIB [65] and X-ray tomography [69, 71, 72]. Initiation is taking place at non-metallic inclusions where butterflies form, some of which then extend and link together, forming WEC networks. Therefore, one possible location at which WECs initiate is the subsurface region. This is important because subsurface WECs have no connection to the surface until they branch towards the surface towards the end of a bearing part's lifetime. Hence no fluid ingress can take place and directly affect crack propagation by corrosion cracking or internal pressure from trapped fluid causing crack opening, i.e., mode I propagation [73]. Furthermore, material loss carried by reactions with atmospheric oxygen or leaching by a fluid is not possible for subsurface cracks. Manieri et al. [74] reported that subsurface WECs occurrence originating at non-metallic

inclusions is linked to the stress history, i.e., excessive loading early in a components lifetime is more detrimental than such that occur later.

3.3.2. The role of hydrogen

Many researchers believe that WEC and WEA formation is relying on atomic hydrogen diffusing into the material. Different hydrogen drivers and sources such as water contamination [75], tribo-chemical reactions [66], corrosion, slip [76], and electric currents [77, 78] are often mentioned. These mechanisms facilitate the decomposition of, e.g., lubricants by nascent metal surfaces created by slip, corrosion, or heating and lightning from discharge currents. All these effects potentially play a role in the actual bearing operation. Since operation conditions in real applications (torque variations, lubrication regime, humidity, localized corrosion, idling, etc.) are usually not well known, it is challenging, if not impossible, to pin down the individual contributions, if any at all. In laboratory testing, a hydrogen-producing driving mechanism is often intentionally used to trigger WEC formation. For example, the design of cylindrical roller thrust bearings causes an extreme amount of slip that is much higher than in other bearing applications. Slip under these mixed friction conditions in the boundary lubrication regime [79] then leads to dissipation of energy, likely creating nascent metal surfaces that facilitate hydrogen formation. Therefore, experiments conducted using FE-8 test rigs [63, 76, 80-82] –a rig designed for lubricant testing – are likely not representative of WECs in bearings in general or wind turbine gearbox bearings. The same is likely true for electrochemical hydrogen charging, which is often used for WEC 'production' in other bearing types [55, 65, 80, 83]. or so-called low reference oils with certain additives [17, 79] that lead to early failures. Numerous investigations exist as evidence that hydrogen shortens the time to failure significantly [51, 55, 65, 67, 84-86]. However, Ruellan et al. [67] demonstrated the artificial hydrogen charging did not only reduce the lifetime significantly to less than 10 % of the non-charged reference bearings but also changed the location of WECs in the material while keeping all further conditions unchanged.

While hydrogen-related WEC formation receives a lot of attention in the literature, rarely actual mechanisms have been presented trying to explain the premature nature of WECs failure. Earlier investigations ascribed the effect simply as hydrogen embrittlement that results in spalling [83, 84]. A more detailed, physically based mechanism was proposed by Vegter and Slyke [55]. They hypothesized that increased hydrogen contents lead to a larger number of vacancies, which are mobile as hydrogen vacancy pairs and are able to promote iron self-diffusion. This then is understood to enable accelerated fatigue damage based on the increased likelihood of dislocation climb. This means that stage 2 in RCF (see section 3.1) is shortened. The enhanced plasticity is also viewed as potentially accelerating butterfly formation because high defect densities in the material, which undergo decomposition and

grain refinement by severe plastic deformation, will attract fast diffusing hydrogen. Butterflies then are thought to propagate and form WEC networks resulting in spalling failures. Very importantly, Uyama at el. [86] showed that while hydrogen charged RCF fatigued samples suffering from accelerated failures due to subsurface crack initiation did exhibit WEA formation, charged samples with surface initiation also experienced accelerated failures, yet without WEA formation. This means that hydrogen can promote failures in RCF with and without the formation of WEAs, i.e., at least in this case, it has different effects that lead to reductions in lifetime.

Since the bulk of the present work is concerned with investigations of a field-returned bearing component that has not been intentionally hydrogen precharged and furthermore has a black oxide finish which is reported to strongly reduce WEC propensity by reducing the hydrogen intake [87], this thesis focusses on hypotheses that leave room for the case that hydrogen indeed enhances WEC formation and maybe propagation, but that it is not the sole root cause of the WEC phenomenon in the investigated bearing. This understanding is strongly supported by three further aspects.

First, vacuum pump bearings, which were run with fluorinated lubricants. i.e., excluding possible hydrogen sources as good as possible, were shown to be affected by WECs [88]. This is also confirmed by Gould et al., who also found that WEC formation in specimens that were tested with fluorinated lubricants [77].

Second, the presence of hydrogen can never be fully suppressed, especially if one takes into account that it diffuses rapidly in ferrite. However, this does not mean that it always has to have a significant effect. Judging from compression tension experiments on quenched and tempered SUJ2 [89] and SAE 52100 [24], it is well possible that for noticeably enhanced crack propagation, a threshold content must be exceeded. Besides, for shear modes, hydrogen seems to be less critical, at least when mode I branching is partially suppressed [90] (i.e., similar to RCF, where it is almost fully suppressed). The number of cycles to failure was only reduced by ~ 50 % for martensitic SAE 52100 samples with 0.05 ppm and 1.6 ppm hydrogen. If hydrogen were the direct or root cause of WEAs, one would need to explain how cracks initiation and propagation are enhanced for shear modes under RCF conditions. Either initiation or propagation has to take place in an accelerated manner when compared to normal RCF. Otherwise, there would be no premature failures. Suppose one would be able to explain this. In that case, the question still arises why WEA formation is necessary for early failures (and not hydrogen enhanced plasticity or embrittlement at the crack tip). And finally, if WEAs do not play a significant role, why are they *the* characteristic feature of this premature failure mode?

Third, several studies that investigated shear mode crack propagation in hardened 1.5 wt% Cr-1 wt% C (100Cr6 and similar grades) bearing steels have presented evidence that the interaction of the crack surfaces (what is called *crack surface rubbing*) leads to grain refinement adjacent to such cracks [91-93]. This means that hydrogen (exceeding the amount that is always present) is not necessary for WEA formation. In addition to these investigations, classical fatigue experiments on this type of high strength bearing steels have also shown that similar grain refinement is present in so-called fine granular areas (FGA) around non-metallic inclusions [94] or at artificial surface defects if tests are run in vacuum [95, 96]. These experiments only led to the reported grain refinement, as long as the stress intensity factor (K_I) was below the propagation threshold [95-98]. These observations indicate that contact between crack surfaces is necessary for the grain refinement to occur and also supports the understanding that it is not a consequence of crack tip plasticity. Similarly, tension-compression tests with superimposed shear loading during the compressive segment lead to grain refinement around cracks [99]. All these experiments were conducted without hydrogen charging and did not lead to early failures. The conclusion, drawn from the observations cited here, is that WEA formation is closely related to the loading scenario a crack experiences.

3.3.3. Chronology of white etching cracks and white etching area

There are different explanations in terms of chronology of events regarding formation mechanism, namely if cracks (WECs) are forming first, which then produce microstructural alterations (WEAs) or vice versa, where WEA is formed prior to cracks, which initiate at and propagate along the interface between WEA and initial microstructure.

Proponents of the ‘WEA first’ hypothesis [30, 65, 88, 100, 101] assume that microstructural alterations are caused by localized plasticity in the absence of cracks, a mechanism, which is supported by hydrogen. Because the resulting WEA is harder than the surrounding bainitic or martensitic microstructure, cracks are thought to initiate at the interface between matrix and initial microstructure. The presence of small volumes of WEA independent of a crack is only shown in a single case in the available literature [65]. There, data were obtained by FIB based tomographic reconstruction that was created by recording BSE images after every sectioning step. Image processing was then used to analyze every frame individually. As detailed depictions of individual slices are not included in the respective publication, one can only speculate on how far the assessment is taking into account that cracks can reweld as shown for a WEC network from the bearing that is investigated in this thesis [102]. If WEAs form first, this requires an explanation of how WEAs are formed, especially how their

localized nature can be brought about without local stress raisers. Holweger et al. [100] explain WEA formation by accumulated plastic deformation in cementite (aided by hydrogen), which then induces a change in magnetic and electrical properties followed by localized heating upon discharge events due to the changed properties. These, in turn, trigger enhanced diffusion of chromium and carbon in certain areas resulting in burst-like WEA formation. Similarly, in [103], electro-thermal decomposition of carbides is proposed as a potential WEC driver. However, recent experimental and theoretical work likely refuted this by showing that undeformed cementite under current densities exceeding those at usual operating temperatures and without deformation is stable [104].

Proponents of the 'crack first' coalition [55, 72, 74, 82, 101, 102, 105, 106] argue that WEA forms by crack surface rubbing, which leads to grain refinement by severe plastic deformation. This is also the present author's stand. Following this line of reasoning, cracks are a precondition for the possibility of WEA formation. They cause localized stresses limiting microstructural alterations to the cracks' direct vicinity. Within this framework, it is reasoned that butterflies extend to WEC networks [82]. Because these are connected to a large number of non-metallic inclusions [106, 107], it is assumed that butterfly cracks are linking together continuously, extending and finally forming large networks (see Figure 3.3 (c)). The extension of WEAs on both sides of cracks – symmetrically and asymmetrically – has been attributed to a sweeping movement of WECs normal to their plane where material transfer occurs from one side of the crack to the other [55, 102]. A further argument in favor of the understanding that cracks precede WEA formation is that the amount of WEA towards the crack tip is drastically smaller than at crack positions that are presumably older, as seen at the initiation sites around non-metallic inclusions. This is also in agreement with laboratory tests emulating RCF conditions where the amount of WEA is larger near the cracks' initiation sites [97]. The experimental evidence cited at the end of the assessment of the role of hydrogen supports the idea that cracks are preconditions for WEA formation.

One aspect has to be further considered because a common understanding within the 'crack first' camp is that WEAs are merely symptoms of WEC associated premature failures [72, 74, 108, 109]. However, the question arises why WEAs seem to be the defining aspect of premature failure due to WECs, if they are not connected to the root cause? This thesis includes an attempt to explain the potential influence of WEA formation in premature failure, which is presented in Chapter 3.

3.3.4. The role of carbon

The role of carbon in WECs is the primary topic of the present thesis, and many characteristics will be traced back to its role in the main body of this work. Some introductory remarks seem fit at this position.

Firstly, the reason why WECs are only found in high and medium carbon bearing steels is likely simple. Carbon alloying of steels is the only way to provide material of sufficient hardness in large quantities at reasonable pricing; hence it is virtually the only class of material used in bearings of sizes larger around 200 mm bore diameter. Other high strength materials are either costly (high nitrogen and maraging steels) or not available in large dimensions and quantities (nanostructured materials). Secondly, although most studies related to WECs are performed on 100Cr6 and similar grades, some further investigations on case hardeners and highly alloyed steels have brought forth some evidence that it is likely that the less carbon a steel contains and the more strongly carbides bind it, the less likely WEC formation occurs. Extreme grain refinement, as seen in WEC/As, is not limited to bearing steels in particular or carbon steels in general. Due to the relative movement of two bodies that causes different wear phenomena, grain refinement with similar morphologies is also observed in Cu [110, 111], Ni [112] or Ni-Ti [110], and many other systems.

From the literature review provided in this chapter and the reasoning drawn from the interrelations of the presented aspect, the key question arises: *Why are WECs propagating faster than cracks in 'normal' RCF*? Only if the underlying root causes are sufficiently understood is it possible to tailor specific, cost-efficient solutions. This thesis aims to contribute to this understanding by an in-depth characterization of the WEA-WEC microstructure with particular attention to the element carbon down to the nanoscale.

Chapter 4 The role of carbon in the white etching crack phenomenon in bearings

This chapter is a modified version of the paper by Mayweg, D.; Morsdorf, L.; Wu, X.; Herbig, M.: *The role of carbon in the white etching crack phenomenon in bearing steels*, [113] Acta Materialia 203 (2021) 116480.

4.1. Introduction

White etching cracks (WECs) are a failure phenomenon primarily observed in high-carbon martensitic, bainitic, or pearlitic steels [16]. WECs are cracks bordered by nano-ferritic regions, which appear white in optical microscopy after etching and are called white etching areas (WEA[6]). WEC-associated failures occur under rolling contact fatigue (RCF) conditions in a broad range of applications, e.g., bearings and rails [16]. In particular, their occurrence in wind turbine gearbox bearings has received attention, as high financial losses due to unpredictable failures are the consequence [16]. WECs frequently occur even at load amplitudes well below the fatigue limit ([17] and references cited there). Failures differ from conventional RCF as they arise unpredictably after only a minor fraction of the calculated lifetime, typically around 5-10% [16]. So far, no damage models are available, which can precisely predict WEC-failure, as the underlying mechanisms are still lacking complete understanding.

It is widely agreed that WECs initiate below the raceway surface at non-metallic inclusions [72, 82] approximately in the zone of highest stresses [33]. Because of their subsurface location, complex loading conditions, and the length scale at which the phenomenon occurs, WECs and the associated microstructure alterations can hardly be investigated in-situ, neither in applications nor in laboratory experiments. The generation of WECs occurs through multiple contributing factors [16]. Cyclic loading in conjunction with, e.g., hydrogen charging [51], electric stray currents [114, 115], or pronounced slip [116] triggers the formation of WECs. Also, lubricants influence the formation of WECs [116]. The highly localized transformation of initially undeformed matrix microstructure into nanocrystalline WEA is attributed to crack surface[7] rubbing [55, 74, 105], which causes the decomposition of the initial microstructure by severe plastic deformation. Recently, Morsdorf et al. [102] proposed a mechanism

[6] W*hite etching area* refers to the altered microstructure, which is a consequence of rolling contact fatigue and micro-cracking. Major constituents are nano-ferritic grains, but also secondary phases or voids may be present, as will be shown in this paper.
[7] *Crack surface* refers to the free surface areas of the WECs inside the bulk material.

that extends the crack surface rubbing concept towards WEA formation by combined crack surface rubbing and crack movement normal to the crack plane [102].

The occurrence of WECs in the widely used 100Cr6 bearing steel (ASTM 52100, SUJ2) was comprehensively reviewed by Evans [16, 17]. Carbon in these steels is present in carbides, such as cementite and transition carbides, as well as segregated to defects and grain boundaries and, to a lesser extent, remains in solid solution. So far, only little emphasis has been put on the role of carbon in WEC failures [64, 117-120]. Yet, high nitrogen steels with partial substitution of carbon by nitrogen have been shown to run without failure in applications where otherwise failures due to WECs often occur [17, 115]. This points out that carbon potentially plays a crucial role in WEC phenomena. While it has been put forward that a reduction in carbon content can reduce the WEC propensity of bearing steels [17, 43, 105], a direct influence of carbon on WEC propagation was not considered. Instead, WEAs are often regarded as a byproduct of WECs, which may be of minor importance for WEC propagation [74, 109]. Still, the reported WEC failures predominantly occurred in steels containing significant amounts of carbon. Hence, further structural and chemical analysis regarding the role of carbon is called-for. Electron probe microanalysis (EPMA) investigations by Pinard et al. have shown that carbon is not simply homogenized in WEAs [119, 121]. In recent studies by Curd et al. [120, 122], such heterogeneous carbon distribution within WEAs was thoroughly investigated. They demonstrated the effect of carbon depletion in WEAs for different steel grades. Additionally, they reported the observed effect in field-returned bearings [120] and in laboratory tests on hydrogen-charged specimens [122]. While WEAs in butterflies only exhibited carbon depletion compared to the matrix material, WEC/WEA networks showed both carbon depletion and enrichment. However, depletion was observed more often, i.e., an overall carbon deficiency was detected. This thesis addresses the open question of the location and effect of the ‘missing’ excess carbon from depleted WEAs, a correlative approach of combined EPMA and atom probe tomography experiments in conjunction with transmission electron microscopy.

4.2. Results

4.2.1. Carbon distribution in WEAs

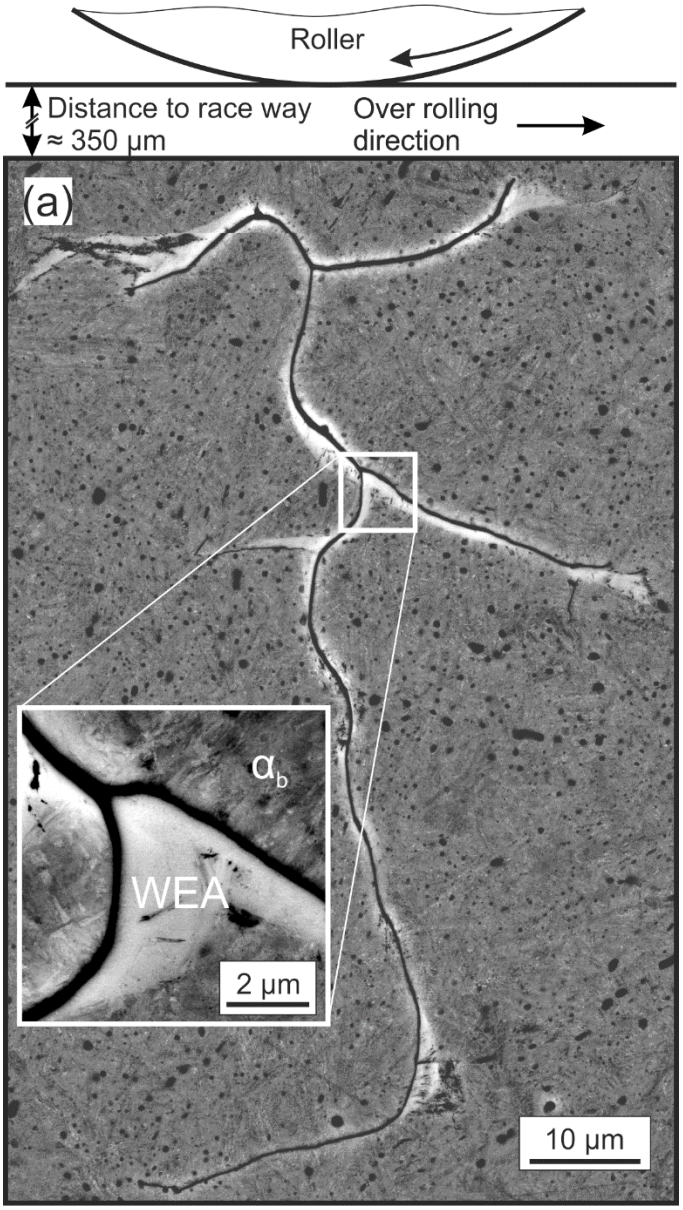

Figure 4.1: BSE image of a typical WEC network in axial view. A magnified region in the inset shows the fine granular WEA adjacent to the WEC.

Figure 4.1 shows a BSE image of a typical WEC network from approximately 350 µm below the raceway surface. In this cross-sectional view, the rolling direction is from left to right. The bright regions adjacent to the crack are WEAs. The bainitic matrix is characterized by typical lenticular grains. In the bainitic microstructure, spheroidized cementite precipitates with a diameter of around ~ 1 µm appear dark in the BSE micrograph due to their lower density. In this particular 2D section, the crack

network extends ~ 90 µm in the depth direction and ~ 60 µm laterally. The inset in Figure 4.1 shows a magnified BSE image of a crack branch with adjacent WEA. While on one side of the crack, the initial microstructure remains unaltered, on the other side, it is completely decomposed and transformed into WEA. The WEA appears in homogenous grey contrast in BSE imaging due to the nano-sized ferritic grains, which cannot be resolved. Note that the seemingly wide opening of the crack in the BSE image is an artifact due to edge effects in this imaging mode. The actual crack opening is far narrower, as will be evident from comparison to topography-sensitive SE images in Figure 4.2.

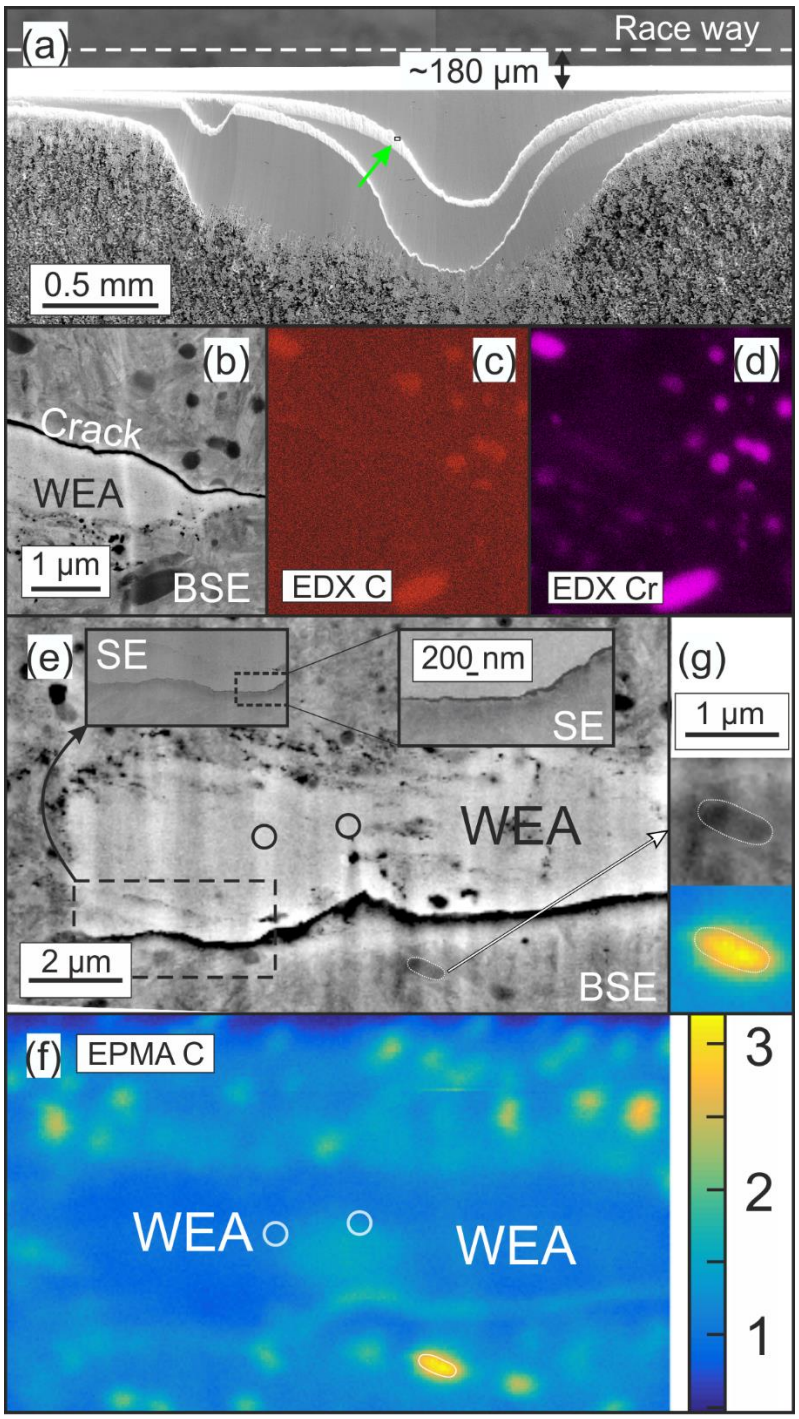

Figure 4.2: EPMA carbon analysis of WEA. (a) SE image of an axial cross-section (i.e., the image plane is normal to the rolling direction) showing terraces generated by several argon-ion cross-section polishing steps. (b) BSE image of a WEC and (c), (d) C and Cr EDX maps (10 kV): C appears homogenous except for cementite positions, while Cr is enriched at some positions inside the WEA. (e) BSE image from the position marked in (a) by a green arrow, insets show SE images demonstrating the narrowness of the crack, which is slightly opened (~50-100 nm). (f) EPMA carbon map. (g) Enlarged views of a cementite precipitate in (e) and (f), which demonstrates the resolution of the EPMA measurement: the precipitate appears larger due to the interaction volume in which X-rays are created.

Sample preparation artifacts can significantly deteriorate the measurement of the carbon distribution. Standard metallographic preparation steps such as cutting, embedding, grinding, polishing, and etching can alter the sample material in an unintended manner. For example, SiC grinding paper, carbon-containing etchants or cleaning agents, diamond polishing suspension, and embedding resin with pyrolytic graphite for better electrical conductivity all introduce carbon-containing debris into cracks or voids in the prepared cross-section. This renders carbon measurements less reliable than it is often acknowledged. Hence, special care has been taken during the preparation and analysis of carbon in WEAs and around WECs. Therefore, argon ion polishing was used to eliminate carbon contamination prior to EPMA measurements. Because of possible contamination and the presence of carbon as a minor element in WEAs (< 1 wt.%), SEM EDX is not a suitable technique to analyze the carbon distribution [123].

Figure 4.2 (a) shows an SE image of an axial cross-section, which provides a tangential view of the sub-surface microstructure, i.e., the over rolling direction is now normal to the image plane. Preparation by argon ion polishing avoids carbon surface contamination that would interfere with the X-ray analyses. One further advantage of this preparation method is that several 100 µm of material can be removed without introducing, e.g., grinding debris into cavities or cracks. In addition, no preferential chemical dissolution of regions with different compositions or grain morphology can occur, as in the case of polishing with colloidal silica or etching [102]. The first ~ 180 µm from the raceway surface were removed by manual grinding to focus ion polishing on the zone of highest shear stress where WECs are typically located. The dashed line in Figure 4.2 (a) indicates the initial raceway position. Figure 4.2 (b), (c), and (d) show a BSE image of a segment of an ion polished WEC and corresponding carbon and chromium EDX maps. Cementite precipitates show up as high-intensity regions in both maps. However, WEA and matrix are not distinguishable in the carbon map, while in the chromium map, regions of increased intensity are visible. This means that EDX in this experimental setup cannot be used to assess the carbon distribution inside WEAs and matrix. Figure 4.2 (e) shows a magnified BSE image of a WEC (position is marked in (a)). The bright vertical lines throughout the cross-section are due to a curtaining effect from ion polishing but do not affect subsequent EPMA mappings. Figure 4.2 (f) shows a qualitative EPMA carbon map of the area depicted in Figure 4.2 (e). The WEA and matrix regions can be identified from comparison with the BSE image in (e). It reveals that the top and bottom areas correspond to the matrix microstructure while the WEA is situated in the middle with an adjacent crack below. Interestingly, lower carbon content is measured inside the WEA when compared to the matrix. This is surprising as WEAs are formed by mechanical mixing during crack surface rubbing and thus should have the nominal alloy composition. Yet, the observation of carbon depletion

in the WEA is in agreement with earlier measurements on WEAs in the literature [119, 120, 122]. From the topographic SE images that appear as insets in Figure 4.2 (e), it is clear that the crack is actually much narrower than suggested by the BSE image. The seemingly enhanced carbon signal at the crack location cannot unequivocally be attributed to significant carbon enrichment but is likely a result of the topographic step that is visible in the SE image and thus is treated as an artifact [121].

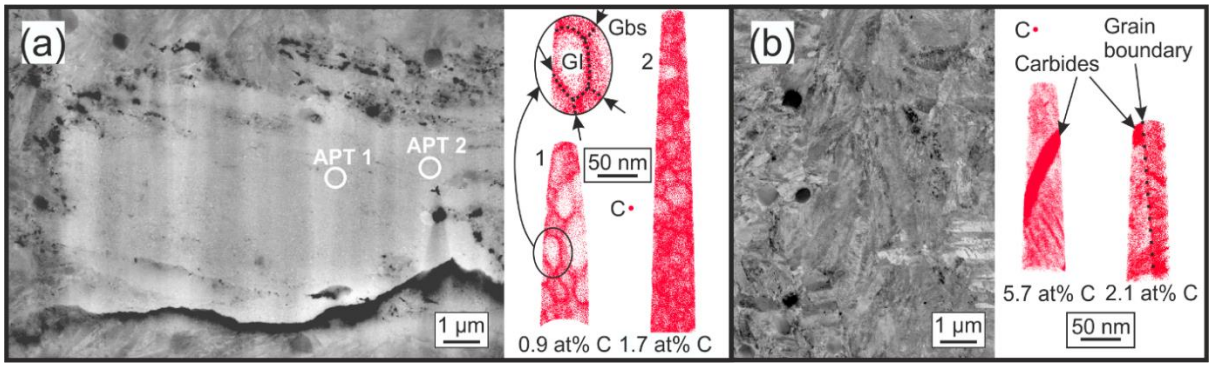

Figure 4.3: APT carbon analysis of WEA and matrix material. BSE images with corresponding APT reconstructions showing the carbon distribution (carbon content is given for each data set). (a) WEA region from EPMA measurement with equiaxed grains revealed by carbon segregation to grain boundaries. (b) Initial matrix microstructure containing carbon in the form of segregation to dislocations and grain boundaries as well as carbides.

Figure 4.3 presents a comparison of WEA and initial microstructure both in terms of BSE images and APT measurements. Figure 4.3 (a) focuses on the WEA that has been analyzed with EPMA in Figure 4.2. The grain structure is revealed by carbon segregation to grain boundaries in two APT specimens, also shown in Figure 4.3 (a). The nanocrystalline ferrite grains are approximately equiaxed and contain less carbon in the grain interior as compared to their boundaries (see enlarged view with black arrows pointing at the grain boundaries). In the 2D slices of the reconstructions shown in Figure 4.3(a), the grain size varies between ~ 10-50 nm. The respective lift-out positions are marked in the BSE image. Locally, an equilibrium is established where the ultra-fine grain size is stabilized by an equilibrium between grain boundary segregation and the carbon inside the ferritic grains, which can be present around dislocation cores, vacancies, or in solid solution [124]. Hence, grain growth is effectively inhibited in WEAs by carbon situated at the grain boundaries [18, 125]. The BSE image in Figure 4.3 (b) shows the initial microstructure of the matrix material. It consists of bainitic ferrite with nanoscale cementite precipitates (as shown in the APT reconstructions) and larger chromium-rich cementite precipitates (as shown in the BSE images).

Comparatively large WEAs, such as the ones analyzed in Figure 4.2 and Figure 4.3, encompass an altered microstructure volume of many µm³ that contained a statistically representative fraction of

spheroidized cementite precipitates and bainitic matrix microstructure in the original condition. Thus, it may be expected that the carbon content of WEAs is close to the nominal carbon composition. However, the determination of carbon contents by APT reveals a significant deviation from the nominal composition. The average carbon content in the APT reconstructions from the WEA shown in Figure 4.3 (a) is 0.9 at% and 1.7 at%, which is significantly below the nominal carbon content of ~ 4.2 at%[8] (as measured by optical emission spectroscopy). A statistically robust analysis based on 20 APT measurements from WEA locations (not all shown here) confirms the observed carbon deficiency in WEAs. The average carbon content in the analyzed WEAs yields only ~ 1.8 at%. Deviations in carbon content between individual WEA measurements were found to be mostly due to differences in local WEA grain size, which in turn affects the total grain boundary area.

The overall carbon content in the two APT volumes from the matrix material depicted in Figure 4.3 (b) is 5.7 at% and 2.1 at%. The average matrix (composed of bainitic ferrite and nanoscale cementite) carbon content, excluding the carbon bound in spheroidized cementite, is ~ 2.7 at% according to ThermoCalc. The average carbon content of the matrix was experimentally determined to be 3.1 at% (10 APT measurements), which is in rough agreement with the calculation considering the heterogeneous structure of the matrix. Therefore, the measured average WEA carbon content is even lower than the one measured of the matrix, excluding spheroidized cementite. In conclusion, the presented APT measurements quantify the difference in carbon content between WEA and matrix, which was qualitatively revealed by the EPMA measurement. The investigated WEAs are depleted in carbon. This raises the question about the location of the missing carbon.

It may be argued that the missing carbon from the WEA has diffused into the matrix microstructure adjacent to the WEA. However, ferrite inside the matrix is already supersaturated in carbon as it contains at least about 1 at% carbon (according to APT results from low carbon precipitate-free regions), while the maximum solubility at RT is as low as 10^{-5} ppm [126]. Hence, there is no thermodynamic driving force for carbon diffusion into the surrounding matrix. On the contrary, there is a driving force for carbon diffusion out of the carbon-supersaturated ferrite in lower bainite or martensite.

[8] Confirmation of the latter value is not directly possible by means of APT because the volume of a single measurement is significantly smaller than the size of some microstructural features like spheroidized cementite precipitates.

4.2.2. Absence of carbide precipitation in WEA

Another possible explanation for the measured carbon depletion in WEAs might be its local agglomeration in the form of cementite precipitates. Kang et al. reported the presence of cementite in WEAs [127] in 100CrMo7 under loading conditions that were not further specified. If these precipitates were unevenly distributed in the WEA, they might be overlooked by EPMA and APT measurements depending on the location of the metallographic cross-section.

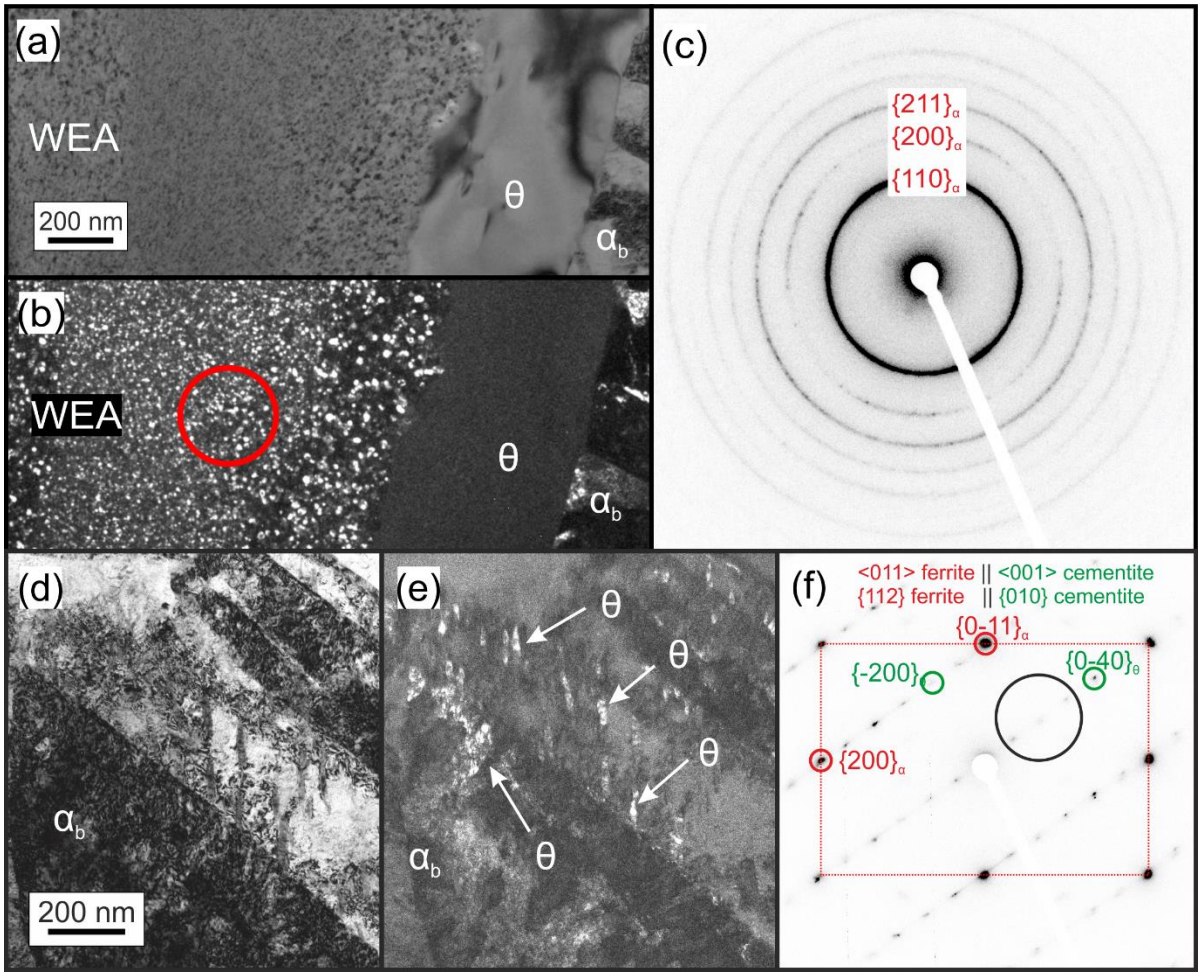

Figure 4.4: TEM diffraction analysis of WEA (a-c) and matrix microstructure (d-f). (a) BF TEM image of a WEA matrix interface with a spheroidized cementite precipitate in the direct vicinity. (b) 10 eV energy-filtered centered dark-field TEM image of the same region as in (a). (c) Selected area diffraction pattern from the region marked by a red circle in (b) showing only ferrite rings and no cementite reflections. Subfigures (d) and (e) BF and displaced aperture dark-field TEM micrographs from the matrix microstructure; (e) is acquired using the reflections marked by a black circle in the selected area diffraction pattern in (f). The bright regions in (e) correspond to cementite precipitates from bainitic transformation and likely follow a Bagaryatski orientation relationship to the matrix ferrite.

At first glance, carbide precipitation seems plausible because the solubility of carbon is exceeded by several orders of magnitude in the nanocrystalline ferrite after the original microstructure is decomposed. However, carbide nucleation and growth require thermal activation. Takahashi et al. and Li et al. observed cementite precipitation in nanocrystalline ferrite (heavily cold drawn wires) in hypereutectoid steels starting from aging temperatures of 350°C and 250°C, respectively [128, 129]. This means that carbide precipitation in such supersaturated ferrite nano-grains only occurs at temperatures significantly above the maximum service temperature of conventional bearings, which is 60-90 °C.In proving the absence of precipitates inside the WEA on a larger scale than by individual APT measurements, TEM investigations were carried out. Figure 4.4 (a) shows a bright-field (BF) TEM image of a WEA next to the initial microstructure. In this particular example, a spheroidized cementite precipitate in the matrix microstructure is located right next to the WEA at the interface. Within the matrix microstructure, the cementite precipitate is only mildly strained, while it is entirely decomposed within the WEA. Such observation was also analyzed in [102] and is frequently observed across the investigated WEC-WEA network. Figure 4.4 (b) displays an energy-filtered centered dark-field image using a portion of the {110} ferrite ring from the corresponding selected area diffraction pattern (SADP) in Figure 4.4 (c). The diffraction pattern was recorded from the area indicated by the red circle in (b). Figure 4.4 (d) and (e) are BF and displaced aperture dark-field TEM images from the initial (unaltered) bulk microstructure. Figure 4.4 (f) shows an SADP along a ferrite <011> zone axis from the dark grain in the lower part of Figure 4.4 (d). Cementite reflections are marked and indexed in green, while red indices show ferrite reflections. The dark-field image in Figure 4.4 (e) is taken from the cementite reflections marked by a black circle in Figure 4.4 (f), and the bright regions correspond to the locations of cementite precipitates, which stem from bainitic transformation. In contrast to the initial microstructure, the selected area diffraction pattern from WEA in Figure 4.4 (c) shows no cementite reflections, and hence cementite precipitation can be excluded inside this WEA. This is particularly remarkable because the WEA is situated right next to a partially decomposed spheroidized cementite precipitate, where the locally highest carbon composition can be expected. Also, there is no indication of transition carbide precipitation that can occur from carbon supersaturated ferrite even at ambient temperatures [130]. The absence of carbides is in accordance with measurements on three other TEM lamellae of WEAs from the same bearing. In comparison, cementite reflections are visible in the SADP from the matrix. This also confirms the results from 20 APT data sets, which did not reveal any cementite or transition carbide precipitates inside WEAs. The absence of carbides is in agreement with soft X-ray spectroscopy investigations on butterfly WEAs by Curd et al. [120]. In conclusion, it can be stated that the results presented above provide evidence that the apparent carbon depletion in WEAs cannot be explained by carbide precipitation.

4.2.3. Presence of carbon deposits

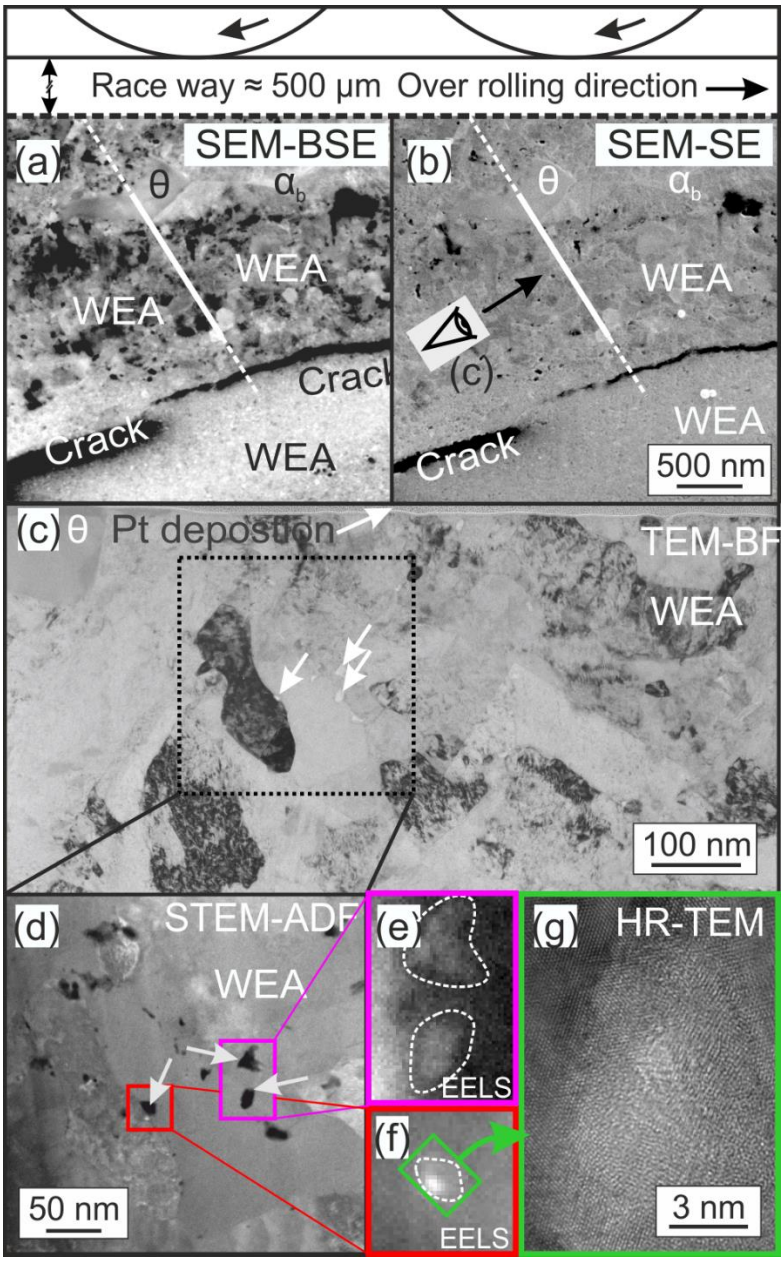

Figure 4.5: TEM analysis of carbon deposits: a) and (b) are SEM BSE and SE images of the same region showing a crack with WEA on both sides and surrounding unaltered microstructure (α_b,θ). The white line shows the TEM lamella lift–out position. The black arrow in (b) marks the viewing direction on the lamella, and the solid line segment marks the extent of the area shown in (c), which is a TEM-BF image of coarse-grained WEA (i.e., several 100 nm grain size). White arrows point at high-intensity regions. (d) ADF-STEM image of the region indicated by a rectangle in (c). Arrows point at regions with comparatively low average density. Segments (e) with red and (f) with magenta outline are carbon maps obtained by STEM-EELS in the region marked by rectangles in (d), enhanced carbon signals at low-density regions marked by dashed outlines. Brighter contrast stands for higher carbon content. (g) The HR-TEM image of the carbon deposit marked by a green rectangle in (d) reveals a different crystallographic structure compared to the surrounding ferrite.

As described above, no carbide precipitation was found inside WEAs. Instead, in some WEAs, one can observe the presence of nano-sized carbon agglomerates in TEM and by APT experiments, as presented in this section.

Figure 4.5 presents these results from analyses of regions containing high carbon deposits inside a WEA[9]. The BSE and SE images in Figure 4.5(a) and (b) show a WEC that is bordered by WEA with different grain morphologies. Bainitic matrix microstructure (α_b) is visible in the upper part of the images, including a partially decomposed cementite precipitate (θ), which is also visible in the upper left in Figure 4.5 (c). The solid segment of the white line marks the trace of the cross-section, which is displayed in (c) as a TEM-BF image. White arrows denote small regions of increased BF intensity. These features are visible in the STEM annular dark-field (ADF) image in Figure 4.5 (d) that displays the area marked by the white rectangle in Figure 4.5(c). The ADF contrast is sensitive to the average atomic number of elements present in the respective area, which is, in this case, substantially lower than in the surroundings. This means that the sparsely and inhomogeneously distributed low-intensity regions contain significantly less iron and other comparably heavy alloying elements such as chromium and manganese. Figure 4.5 (e) and (f) show carbon maps acquired by STEM-EELS. These maps qualitatively confirm that the regions with low Z contrast are enriched in carbon if one compares the white outlines with the same positions in the ADF image in Figure 4.5 (d). The lamella thickness is ~60-80 nm in the ferrite region near the carbon-rich deposits as determined from the ratio of zero loss and plasmon peak, assuming an average atomic number of 26. Since the neighboring ferritic grains still contain a small amount of carbon and some hydrocarbon may be present on the lamella, further quantification is challenging. Yet, any substantial carbon contamination coming from the metallographic preparation can be ruled out because the investigated TEM lamella was extracted from the bulk material, i.e., no connection to the surface was present before preparation by FIB. The energy-filtered high-resolution TEM image in Figure 4.5 (g) from the position of the rectangle in Figure 4.5 (f) shows that these regions consist of matter with significantly different crystallographic structures than the adjacent ferrite grains. It appears to be at least partially amorphous. Further clarification on the crystallographic structure of these carbon deposits could not be achieved as FIB-based specimen preparation as well as high energy electrons in the TEM are known to potentially alter the original structure [131].

[9] To reveal the location of missing carbon in the WEA, a particularly coarse-grained WEA is analyzed where the difference of carbon content in comparison to the nominal value is particularly large (measured by APT, data sets not shown here).

APT measurements were conducted to quantify the local carbon enrichment in such carbon deposits. During APT experiments, the applied electric field exerts a significant mechanical force on the specimens. The carbon deposits are weakening the structural integrity of the APT specimen by acting as stress raisers and often cause early fracture during APT measurements. Compared to electron spectroscopy, APT has the advantage that light elements such as carbon are detected with the same accuracy as heavier elements such as in the present case, iron, chromium, and manganese.

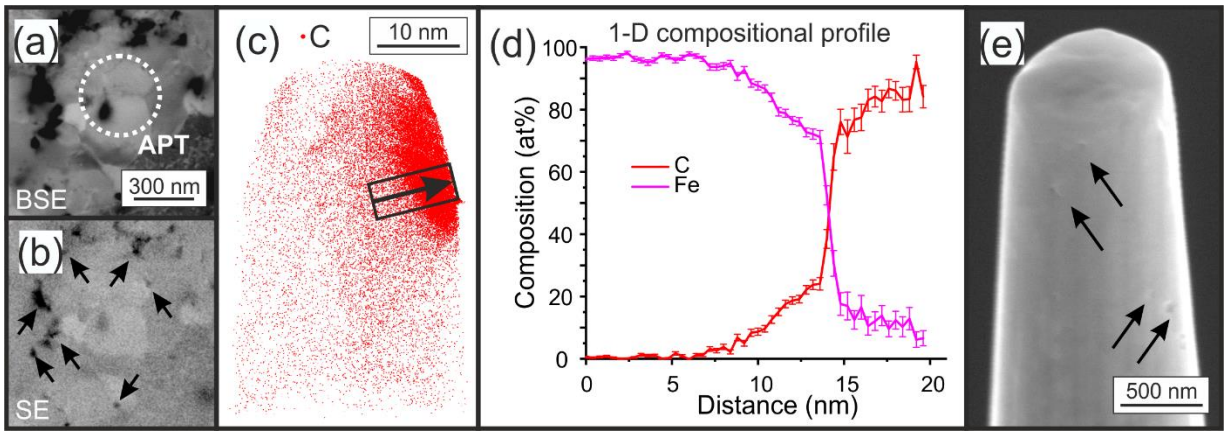

Figure 4.6: APT analysis of carbon deposits. BSE (a) and SE (b) images of a small segment of WEA selected for target preparation by FIB for APT analysis. Black arrows in (b) show carbon deposits on the sample surface. (c) APT reconstruction of about eight million ions from the region marked with a white circle in (a) displaying all carbon atoms therein. (d) 1D composition profile along the arrow in (c), only Fe and C are displayed. Subfigure (e) is an SE image taken during FIB preparation of an APT specimen from a similar region. Black arrows mark locations of carbon deposits.

Figure 4.6 (a) and (b) show a BSE and SE image of a small segment of WEA that was selected for target preparation of an APT specimen. In Figure 4.6 (a) and (b), small features with dark contrast are visible, which are marked with black arrows. These are likely carbon-rich deposits as in the TEM lamella cross-sections in Figure 4.5; due to their high carbon content, the carbon deposits should be considerably softer than the surrounding matrix and can therefore be removed from the sample surface in the course of metallographic preparation, leaving cavities behind. Distinguishing regions with very high carbon content and holes is often hardly possible in SEM due to the low electron density of carbon. Figure 4.6 (c) shows the APT reconstruction of the measurement from the region marked in Figure 4.6 (a). Only carbon atoms are displayed. A carbon-rich region captured in this measurement is located in the upper right part of the reconstructed volume. Figure 4.6 (d) shows the 1D composition profile along the arrow in Figure 4.6 (c). For the sake of clarity, only iron and carbon profiles are shown in the graph. The composition of carbon increases from ~ 1 at% to a maximum of more than 85 at% over a distance of ~ 15 nm. Regions with high carbon contents such as carbides are known to have a significantly different field evaporation behavior than ferrite, which leads to the so-called local magnification effect

in APT measurements [132]. This effect leads to a superposition of recorded ion positions from the adjacent phases on the detector, which blurs out sharp compositional changes and compromises compositional measurements within a few nm around interfaces. Thus, the transition between matrix and high carbon deposit is, in reality, more abrupt than measured here, and the measured carbon content is an underestimation, i.e., the real carbon composition must be higher than 85 at%. The measured composition exceeds the carbon compositions of typical carbides found in steels by far. Stoichiometric cementite contains only 25 at% carbon. The carbides with the highest carbon contents are ε-carbide and η-carbide with a composition of $Fe_{2\text{-}3}C$ (25-33 at% carbon) and Fe_2C (33 at% carbon), respectively. Thus, it can be ruled out that the carbon deposits represent carbides that precipitated in the microstructure. In terms of spatial dimensions, the carbon deposit measured by APT is in agreement with the ones observed in TEM. Additionally, Figure 4.6 (e) shows an SE image from an APT specimen during preparation by FIB from a similar area as displayed in Figure 4.6 (a) and (b) with features in the same order of spatial dimensions as observed in APT and TEM. These cannot be introduced during metallographic preparation, as they are only uncovered during FIB milling. While APT proves an extremely high carbon content locally in carbon deposits within the WEA, the TEM investigations and the SE images show that such features are frequently observed in WEAs. Still, quantifying the distribution of carbon deposits from polished sample surfaces is challenging, as explained above, and the number density of such carbon deposits is too low for the acquisition of statistically relevant data from TEM or APT measurements. Note that the corresponding features on the sample surface shall not be confused with larger cavities caused by preferential etching of ferrite grains during metallography, as it was shown in [102].

4.3. Discussion

The complementary use of scale-bridging EPMA and APT measurements revealed carbon depletion inside WEAs with respect to the average initial matrix carbon content. Carbon cannot leave the bearing. This implies that significant carbon redistribution must take place along with WEA formation and that the missing carbon must be located elsewhere in the microstructure. The following aspects are now discussed: the process of carbon redistribution, the structure of deposits, and their formation mechanism; finally, the potential role of the WEC crack surfaces in terms of serving as an additional carbon sink. Last, a hypothesis is proposed how this phenomenon can contribute to the accelerated bearing failures by WEC formation.

4.3.1. Structure of carbon deposits

The presented results show that at least part of the carbon deficiency in carbon-depleted ferritic grains in WEAs is compensated by highly concentrated and localized carbon deposits inside the nanocrystalline WEA microstructure. In the previous sections, evidence of (i) local carbon depletion and (ii) the presence of carbon deposits with carbon compositions far beyond those of iron carbides were presented.

The presence of carbon deposits with compositions much higher than iron carbides poses the question about the crystallographic structure of these carbon agglomerates. As detailed above, the measured carbon content of at least 85 at% means that these carbon enriched regions cannot be carbides. Only the pure carbon allotropes graphite, diamond, or amorphous carbon can exist as bulk volumes and contain more than 85 at% carbon. The presence of diamond can certainly be ruled out, as this requires high combined pressures and temperatures, which are not met in bearings. For example, diamond formation in the Fe-Co-C system requires a temperature of 1190 °C and a pressure of 6 GPa [133]. This leaves graphite and amorphous carbon as possible allotrope being present in carbon deposits.

The formation of graphite can occur even in low carbon steels with low sulfur and phosphorous contents. Okamoto [134] showed that graphite forms by nucleation and growth inside voids created by cementite particles cracked during cold deformation. As graphite formation from cementite is accompanied by a volume expansion, Okamoto concluded that voids must be present that facilitate the graphitization of cementite. Similarly, a volume expansion must take place during graphite formation from supersaturated ferrite. Gridnev and Gavrilyuk [135] investigated deformed pearlite by Mößbauer spectroscopy and dilatometry. They conclude that the formation of graphite occurs at micro-cracks, which are introduced during deformation hence also supporting the hypothesis of graphite formation in the current case. In the scenario of carbon-supersaturated WEAs adjacent to WECs, this volume expansion can be easily accommodated at the surface of an open crack inside the material. Carbon being exposed to tribological contact situations can transform into graphite as was shown by Stoyanov et al. [136], who investigated dry sliding contact of diamond-like carbon and tungsten using micro Raman spectroscopy while on the virgin samples, no graphite could be identified. Graphite formation was also detected in tribological contacts of high-carbon CoCrMo metal-on-metal hip implants in-vivo [137]. Thus, graphite can form at surfaces exposed to cyclic frictional loads already at 37 °C body temperature [137]. Furthermore, the graphitization of carbon materials is promoted by shear strains [138, 139]. These processes are likely close to the wear scenario during WEC crack surface rubbing. The typical temperatures in bearings during service are between 60 °C and 90 °C and thus significantly

higher. Hence, one can readily assume that graphite formation is in principle possible in the case of subsurface WECs. On the other hand, amorphization of carbon can occur, as graphitic carbon can become amorphous through the accumulation of defects through severe mechanical loading [140]. Thus, intense surface rubbing could generate a mixture of graphite and amorphous carbon. However, providing experimental evidence for the structure of the carbon deposits has proven challenging as FIB milling during sample preparation, and high energy electrons used for TEM investigations are known to alter the structure of carbon-rich material such as graphite [131].

4.3.2. Formation of carbon deposits

In this section, a mechanism is outlined, which explains the formation of carbon deposits as a part of the WEC failure scenario. Thermodynamically, it is favorable that the excess carbon from the WEA enriches at the WEC crack surface. There is a thermodynamic driving force for carbon to leave the WEA that scales with the level of carbon supersaturation in ferrite [126]. Due to the operating temperatures below 100°C, carbide precipitation inside the WEAs does not occur. This conclusion is confirmed by soft X-ray emission spectroscopy [18] and the results from TEM analyses in Figure 4.4. Carbon diffusion into the bainitic matrix adjacent to the WEA also cannot take place since this region is already supersaturated in carbon. In contrast, the WEC crack surface presents an energetically favored location for carbon migration. Carbon segregation to iron surfaces has been investigated in several studies in literature, both theoretically and experimentally. Carbon segregation to bcc iron surfaces was experimentally observed under vacuum conditions in alloys with carbon compositions as low as 90 ppm leading to full carbon coverage of the surface [141, 142]. Jiang and Carter employed density functional theory simulations and calculated a net driving force for carbon to segregate to free surfaces and form graphite [143]. Furthermore, it was shown by Auger spectroscopy and low energy electron diffraction that carbon surface segregation and graphite formation can occur on ferrite (100) [142, 144] and (111) surfaces [145]. Carbon surface segregation is only reported to occur on pure iron surfaces. Oxide layers at the crack surfaces or diffusion of sulfur to this free surface might prevent the process. However, in the present case, oxide formation can be excluded due to the subsurface location of WECs and their isolation from atmospheric oxygen. Further, modern bearing steels contain low amounts of sulfur, which is mostly bound in MnS inclusions. No sulfur could be detected in any APT dataset from the matrix or the WEA in the investigated bearing. Hence, the rejection of carbon atoms by a site-competition effect between sulfur and carbon atoms at the crack surfaces can also be excluded.

The aforementioned investigations on carbon surface segregation were conducted at comparatively high temperatures providing high mobility for carbon (e.g., 450-700 °C [142, 144]), which are not

present in this case. However, the mobility of carbon atoms in the present scenario is surely still high enough for diffusion to the free WEC surface. Even at room temperature, carbon atoms can diffuse several nm per year in martensite [130]. Hence, for typical bearing operation temperatures of 60-90 °C and long operating times in the order of years, carbon diffusion towards the crack surfaces is feasible on kinetic grounds. Additionally, it has been shown in a previous study on the same failed bearing that crack surface rubbing even results in redistribution of substitutional alloying elements across several microns [102]. This occurs through mechanical mixing as substitutional elements such as chromium are not mobile enough solely via diffusional mechanisms. Similarly, the redistribution of carbon is initially supported by transport along with moving dislocations during crack surface rubbing. Once nanocrystalline WEA is formed, grain boundary diffusion is likely to facilitate carbon migration towards the crack. Even carbon bulk diffusion in nanocrystalline iron can be sufficient to cover nanoscale distances [130] towards the crack. Furthermore, it was shown that WECs might exhibit a particular crack propagation behavior [102]; they do not only extend but in addition also continuously change their location in the microstructure normal to their crack plane. Alternating crack opening and rewelding, as well as severe plastic deformation induced by crack surface rubbing, cause continuous atomic-scale material transfer from one side of the crack to the other during each loading cycle. This results in a µm-scale crack movement during very high cycle RCF. During this process, the original microstructure decomposes and leaves behind WEAs [102], which also explains the formation of butterflies [28]. This movement of WECs normal to their crack plane makes it possible for the crack surfaces to collect carbon on their way through the microstructure. Even though the diffusion of carbon to the WEC is possible, it would not be required for carbon accumulation at the WECs. The movement of WECs additionally can explain the finding of carbon deposits inside WEAs. Not all of the carbon atoms collected by the WEC can be stored permanently at the crack. A fraction of the carbon content gets trapped in nm-scale asperities at the WECs. When the crack moves on, these are left behind as nm-scale deposits in the WEA.

To conclude, it is proposed that carbon decoration at WEC surfaces is responsible for the formation of carbon deposits. This means that both the presence of carbon deposits in WEA as well as preceding carbon agglomeration at crack surfaces compensate for the observed carbon depletion in WEAs as measured in EPMA and APT measurements.

4.3.3. Estimation of carbon layer thickness at a WEC

Based on 20 APT measurements, an average carbon content of ~ 2 at% is found in WEAs. However, a full homogenization of carbon in WEAs would yield the nominal alloy composition of ~ 4 at% C. This

means that depletion of ~ 50 % inside the measured volumes is present. If one assumes that this amount of carbon (~ 2 at%) leaves the WEA and transforms into graphite with a density of 2.26 g cm^{-3} results in a volume increase of ~ 1.7 %. As discussed above, the missing carbon content is present either in the form of deposits in the WEA or at a crack. Assuming that all missing carbon is present at the crack, for a WEA with a width of ~ 6 µm as shown in Figure 4.2, a carbon layer of ~ 100 nm thickness would be expected. This value is visualized with a 100 nm scale bar in the inset in Figure 4.2 (d) and roughly corresponds to the extent of crack opening in this area. However, part of the carbon will be stored as carbon deposits, and hence ~ 100 nm of carbon layer thickness at the crack is an upper bound for a 6 µm wide WEA. Many WEAs are significantly narrower, as can be seen in Figure 4.1, and the upper bound of the carbon layer thickness will be correspondingly reduced. The thin nature of these films the fact that they consist primarily of carbon make their detection challenging. SEM-EDX and EPMA measurements are compromised by edge artifacts since X-ray spectroscopy requires a flat surface [123]. Therefore, these techniques cannot provide reliable data. APT is not suitable due to limitations with regard to preparation. During FIB-based TEM specimen preparation, the much softer carbon films are preferentially milled away, and also redeposition of carbonaceous matter occurs. Conventional TEM specimen preparation by electropolishing is not possible due to the localized nature of the WECs, and as the specimen would contain cracks and fixation by carbon-containing resins must be avoided. Attempts to probe the carbon films by Raman spectroscopy on the surfaces of specimens that were fractured to expose the WECs were so far unsuccessful. On the one hand, hydrocarbon contamination occurs when the specimens are not fractured under vacuum; on the other hand, locating the WEC-containing regions on the crack surface is challenging.

4.3.4. Crack initiation and propagation in RCF and the effect of carbon

Last, it is discussed how crack initiation and propagation in RCF can be altered by the presence of carbon at the crack surfaces. WECs were shown to initiate below the surface [82], i.e., in the absence of atmospheric oxygen. Hence, during compressive loading, non-oxidized iron surfaces get in contact with strong cohesive forces between them. Considering that the contact in combination with shear between non-oxidized metal surfaces leads to cold-welding [146], it is questionable whether WECs could propagate under such conditions. Certainly, high friction would exist between such crack surfaces in a vacuum, thereby impeding the observed crack surface rubbing. The presence of a carbon layer at the WEC crack surfaces separates the Fe surfaces, thereby reducing friction between them. Graphite and amorphous carbon are significantly softer than the surrounding WEA, martensite, or bainite and would easily comply with the imposed sliding motion between the crack surfaces.

In the following, the effect of carbon-decorated crack surfaces on the propagation of WECs is discussed. In high strength steels as used in bearings, the plastic zone at the crack tip is small (< 1 µm [96]), and therefore cracks of several µm lengths already behave as long cracks according to linear elastic fracture mechanics [147]. This is because of the small size of the microstructural features; the martensite laths and bainite sheaves have a width in the order of a few 100 nm [148]. In such a scenario, long-range stress fields govern crack propagation. Crack initiation in RCF usually takes place at non-metallic inclusions, especially at oxides containing Al and Ca, MnS, and TiN [48], due to compressive mode I loading. In the case of bearings, this results in the formation of butterfly-shaped cracks and WEA arrangements around non-metallic inclusions ([16] and references therein), which upon linking together and form extended WEC networks that finally cause failure.

Although mode I loading causes crack initiation at inclusions, further mode I crack propagation is limited to the typical dimensions of butterflies (i.e., several tens of µm). This is because tensile stress fields around inclusions fade out at this distance [50]. In consequence, fatigue life is not primarily determined by crack initiation as would be the case for high cycle fatigue cracks driven by less complex stress states (e.g., push-pull or rotating bending) [59]. Instead, it is governed by the crack propagation rate. Hence, any effects on the propagation rate are of particular importance. After crack initiation, further crack propagation is driven by shear, namely modes II/III. This was shown by Makino et al., who investigated crack initiation and propagation in RCF experiments with artificial indents and calculated mode I, II, and III stress intensity factors (SIFs), which represent the driving force for crack propagation, using finite element analysis [60]. Their results show minima and maxima of the mode II and III SIFs before and after the rolling element reaches the position right above the crack tip. This suggests that crack propagation occurs by mode II/III before and after the rolling element reaches the position above the crack tip. In this qualitative assessment, no distinction between mode II and mode III is undertaken, since the complex WEC geometry, microstructure, and stress states make it virtually impossible to discriminate between the two. In either way, friction between the crack surfaces plays a crucial role in crack propagation. Under RCF conditions, the effective SIFs are diminished by interactions between the crack surfaces [91, 149]. This effect, which is also referred to as crack tip shielding, is extrinsic, i.e., not a material property, and is caused by the interlocking of asperities or by frictional attenuation [150]. It reduces the crack tip displacement and can lead to an ever decreasing propagation rate [151]. A layer of carbon at the crack surfaces will significantly decrease friction between them, thereby enabling the applied mode II/III loads to act effectively at the crack tip leading to crack propagation. Thus, carbon films at the WECs increase crack tip displacement, lead to a higher SIF, and increase the driving force for crack propagation. Ultimately, these effects lead to an accelerated

crack growth rate. This line of reasoning might also explain why this phenomenon is only observed in high carbon steels.

The proposed effect is illustrated in Figure 4.7. Three consecutive positions of a rolling element during one cycle are shown in Figure 4.7 (a). Figure 4.7 (b) shows a graph that schematically describes the evolution of the stress intensity factor for shear modes II/III during one cycle. Minima and maxima of the SIF occur before and after the rolling elements reach the position exactly above the crack. The red and black lines in Figure 4.7 (b) schematically characterize the behavior of a crack with and without carbon 'lubrication', respectively; the presence of carbon increases the effective SIF and hence raises the crack growth rate. The numbers above the individual positions of the rolling element in Figure 4.7 (a) refer to the minimum, zero-crossing, and maximum values of the SIFs in Figure 4.7 (b).

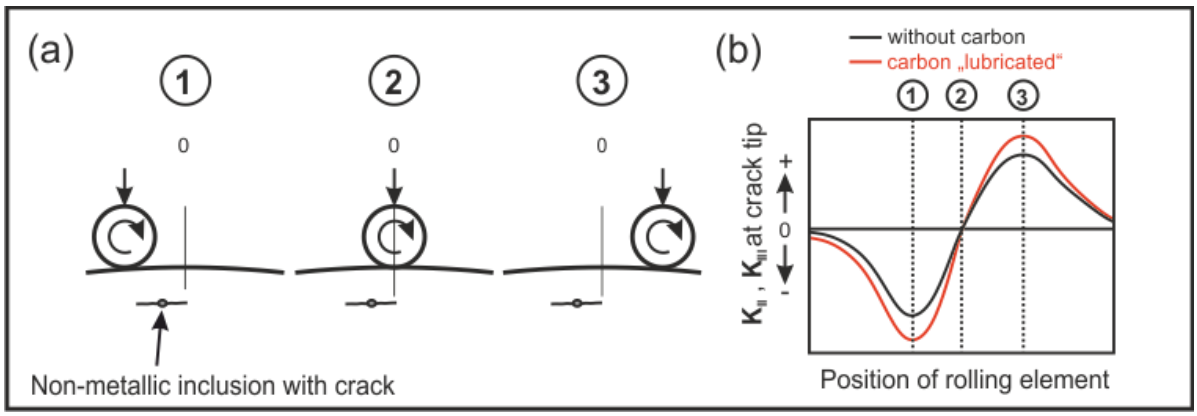

Figure 4.7: Schematic of the proposed mechanism leading to enhanced crack propagation of WECs. (a) Schematic sequence of a load cycle and (b) the possible carbon effect on the shear mode stress intensity factor at the tip of an elliptical crack in RCF.

The present author fully agrees with earlier assessments that consider WEAs as the consequence of WECs than as the cause [74, 105, 109]. First, a crack must form to facilitate crack surface rubbing, which can create WEAs. However, the potential importance of WEAs for the WEC failure phenomenon must be emphasized. WEAs may be the source of carbon that provides the WEC with a lubricating carbon film, which then accelerates the fatigue crack growth rate. In this scenario, WECs obtain their particular properties from the WEAs. A rough estimate of the magnitude of the effect is presented in the following, which is based on investigations of threshold values for mode II crack propagation by Matsunaga et al. [91] and Okazaki et al. [93], who both investigated martensitic 52100 bearing steel, albeit employing different approaches. Matsunaga et al. performed torsion tests on rods with axial notches. They used different notch geometries with varying fractions of crack surface contact. The approach of Okazaki et al. utilized pipes with axial notches on the outer shell surface. Hydraulically applied internal pressure was then used to create hoop stresses, which cause static crack opening (i.e.,

a positive mode I stress intensity factor). For this estimation, only experiments that showed microstructural alterations (similar to WEA) were taken into account. If such alterations are not found, no contact between crack surfaces has taken place, which means that comparison to WECs does not make sense. In both cited studies, decreasing threshold values for mode II crack propagation were observed with decreasing crack surface interference while the reverse trend is noticed for mode I, respectively. The reductions of the threshold stress intensity factors for fully closed and slightly opened cracks (that still show microstructural alterations) can be estimated to be ~ 8 % [91] and ~ 16 % [93]. However, these experiments were conducted in air, while WECs propagate subsurface under vacuum conditions. It is, therefore, noteworthy that Murakami et al. [152] reported higher threshold stress intensity factors under vacuum conditions than in air for mode II, which means propagation under vacuum is slower than in air. This is explained in terms of lower friction in the case of oxidizing surfaces in the experiments conducted in air. Contrary to this observation WECs are subsurface cracks (i.e., under vacuum), which exhibit accelerated instead of slowed down propagation. A carbon film at WECs is a reasonable explanation for this and might be the crucial element in explaining the premature nature of the WEC phenomenon. Still, the proposed accelerated crack propagation by the presence of carbon films at the crack requires further research to quantify the magnitude of this effect.

4.4. Conclusion

WECs in a 100Cr6 wind turbine gearbox bearing with a focus on the nano- and micron-scale carbon redistribution involved in the formation of WEAs were investigated.

- Large parts of WEAs are carbon-depleted in comparison to the surrounding matrix, as shown by EPMA and APT measurements.
- Nanoscale carbon deposits with carbon composition above 85 at% are heterogeneously distributed across WEAs, as shown by multi-scale SEM, TEM, and APT analysis.
- It is proposed that excess carbon from carbon-supersaturated WEAs segregates to the WEC crack surfaces. Upon crack surface rubbing, carbon agglomerates at asperities of the WEC. When the WECs move through the microstructure, these agglomerates are left behind in the form of carbon deposits in the WEA.
- Carbon films at the WECs supposedly reduce friction between the crack surfaces, thereby decreasing crack tip shielding and increasing crack tip displacement. This results in accelerated crack propagation contributing to bearing failures that cannot be predicted according to conventional fatigue laws.

Chapter 5 Correlation between grain size and carbon content in white etching areas in bearings

This chapter is a modified version of a paper by the author of the present thesis: Mayweg, D.; Morsdorf, L.; Li, Y..; Herbig, M.: *Correlation between grain size and carbon content in white etching areas in bearings*, which is under review at Acta Materialia.

5.1. Introduction

Recently, a mechanism that explains the generation of WEAs through crack surface rubbing of WECs in combination with crack movement through the material has been described [102]. This localized severe plastic deformation leads to complete decomposition of the initial microstructure and transformation into fine-grained ferrite with grain sizes as small as 10 nm. As the formation of WEAs by crack surface rubbing involves the redistribution of alloying elements by mechanical mixing, it could thus be expected that WEAs have the nominal carbon content of the alloy. However, this is not the case [113, 119-122]. In most cases, WEAs are found to be carbon-depleted. In the present scenario, carbide precipitation is hindered due to the kinetic limitations at bearing operating temperatures. No carbide precipitation was found in WEA microstructures via APT and TEM in the present and the previous Chapter 4. This is in agreement with the work by Curd et al. [120] as elucidated via soft X-ray emission spectroscopy.

Thermodynamic stabilization of nanocrystalline materials by solutes is known for several alloy systems, e.g., Co-P [153], Ni-P [154], and Ni-W [155], as well as Fe-C [124, 156]. By using APT, detailed insights into the local composition of WEAs of various grain sizes and carbon contents are provided. Quantitative carbon analysis is employed, showing that the local grain size is largely scaling inversely with the local carbon content. Finally, the WEA microstructure evolution is discussed, and the results are compared with theoretical concepts on nanostructure stabilization developed by Weissmüller [157, 158] and Kirchheim [159-161] and results from model experiments on Fe-C alloys [124].

5.2. Experimental

For statistical reasons, data from a WEC-affected washer fatigued in an FE-8 test rig [18] were additionally used in the current analysis. The compositing of this washer is 4.43 at% C, 1.52 at% Cr, 0.48 at% Si and 0.35 at% Mn, respectively (section 2.1). The concentration of further trace elements is below 0.1 at% in each case. The washer was martensitically through-hardened.

5.3. Correlation between grain size and carbon content

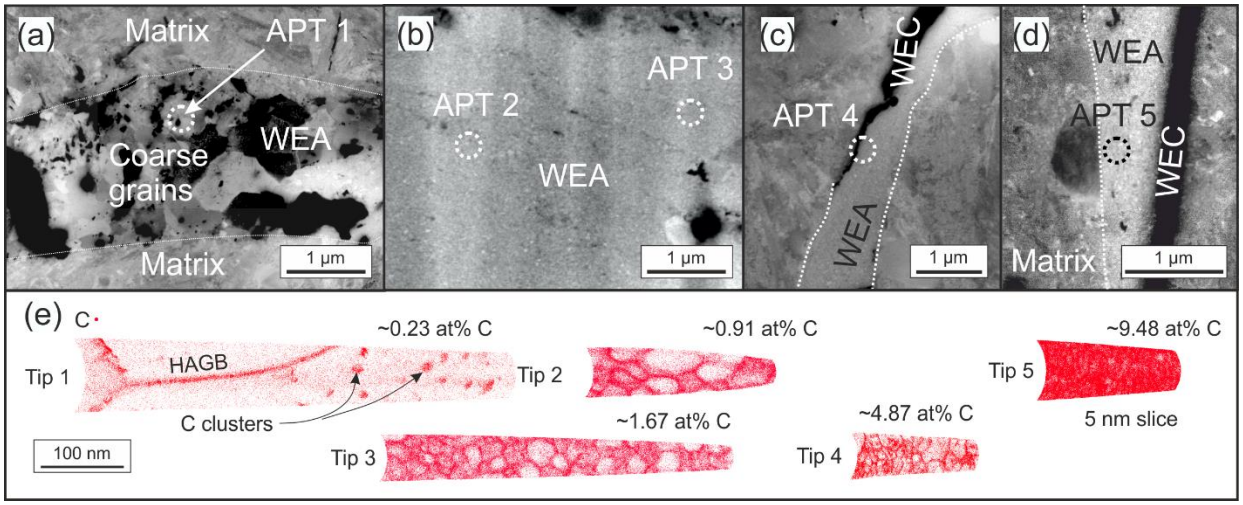

Figure 5.1: Carbon content in WEAs of varying grain size: Four SEM micrographs showing WEAs with decreasing grain sizes from left to right: (a) >100 nm, (b), (c) ~15-70 nm, and (d) ~10 nm.. (e) 10 nm thick slices of carbon atom maps from APT measurements (tips 1, 2, 3 & 4) from the positions marked in (a), (b) and (c) and 5 nm thick slice (tip 5) from the position marked in (d). All detected carbon ions are displayed, and the average carbon content for each tip is noted.

Figure 5.1 (a)-(d) show BSE images of three WEAs with different mean grain sizes (d_m): (a) >100 nm, (b), (c) ~15-70 nm and (d) ~10 nm. APT specimens were extracted by site-specific FIB lift-outs from the locations indicated by dashed circles. All reconstructions were calibrated using [110] ferrite poles in the detector hit maps and adjusting the lattice spacing to the known value of 0.202 nm for {110} bcc iron planes [162]. 2D slices of 10 nm thickness (tip 5 - 5nm slice) from the reconstructed volumes displaying all detected carbon atoms are depicted in Figure 5.1 (e). Individual ferrite grains are revealed by carbon grain boundary (GB) segregation. In tip 1, nanosized carbon clusters are also present in the grain interior. When the mean grain size is below ~100 nm, the APT datasets contain multiple grains (tips 2-5). This allows the quantification of the mean grain size directly by APT. For extremely fine WEAs, the identification of individual grains is less reliable because of the limits of spatial resolution in APT and possible measurement artifacts. For coarse-grained WEA, the mean grain size was determined from BSE micrographs close to the respective lift-out positions. A general trend of increasing mean grain size with decreasing carbon content in WEAs is evident from the series of APT measurements in Figure 5.1.

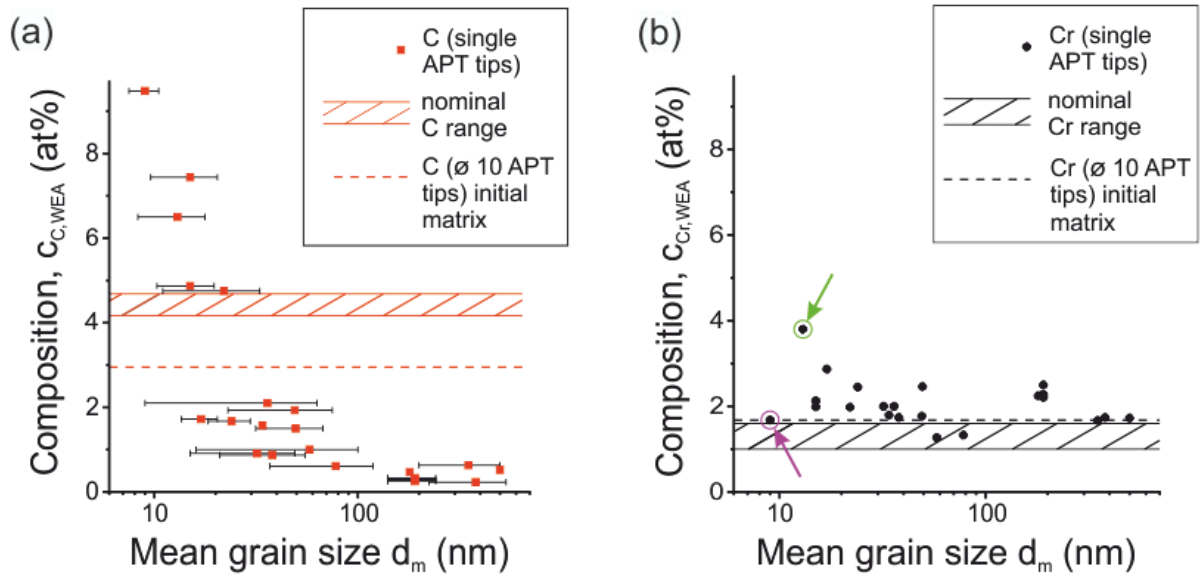

Figure 5.2: Relationship between grain size and composition: (a) and (b) are plots of average carbon and chromium contents $c_{C,WEA}$ and $c_{Cr,WEA}$ from 20 APT measurements as a function of d_m. $c_{C,WEA}$, and d_m show an inversely proportional relationship (a), while $c_{Cr,WEA}$ and d_m do not exhibit such relation (b). Hatched areas in (a) and (b) indicate the nominal carbon and chromium content range of 100Cr6 according to the DIN standard; dashed lines mark average compositions of 10 APT data sets from the bainitic matrix (excluding spheroidized cementite precipitates). Two data points are specifically marked in (b): the highest value of $c_{Cr,WEA}$ (green arrow) and the smallest grain size (magenta arrow).

Figure 5.2 (a) and (b) display the relation between mean grain size and both carbon and chromium contents ($c_{C,WEA}$ and $c_{Cr,WEA}$). The plots include data from 20 APT measurements. The error bars mark standard deviations of measured mean grain sizes. The statistical errors for carbon and chromium contents quantified by APT are smaller than 0.01 at% because of the large number of detected ions and are therefore not indicated in the graphs. The dashed lines indicate the measured matrix contents of carbon and chromium, i.e., the initial bainitic microstructure excluding spheroidized $(Fe,Cr)_3C$-precipitates. The solid horizontal lines mark the compositional range for 100Cr6 steel specified by the DIN standard (DIN EN ISO 683-17). From the data points in Figure 5.2 (a), it is evident that most WEAs are depleted in carbon with respect to the nominal carbon content, as it was also shown in [119, 120, 122] and explained in[113]. The origin of the significantly higher carbon content in some measurements will be addressed later in the following section 5.4. Figure 5.2 (a) exhibits an inversely proportional relationship between mean grain size and carbon content, while Figure 5.2 (b) shows that the same correlation is not observed for Cr. The scatter that is present in chromium content is not directly related to the WEA grain size. Regarding the distribution of chromium within the APT reconstructed volumes, no segregation to GBs is observed (not shown in detail). This is in agreement with results from the work of Li et al. [163], where after annealing at 400 °C for 30 min, no Cr

segregation at nanocrystalline ferrite grain boundaries is observed. This is expected since chromium exhibits a high solubility in ferrite (~8 at% [164]), which provides no significant driving force for GB segregation. It is found that the average amount of chromium in the measured WEAs lies slightly above the nominal chromium content as well as the one measured on the bulk samples by optical emission spectroscopy. The observed deviation is likely related to an underestimation of iron by APT by detector pile up as well as direct current evaporation. Detector pile up is more severe in voltage pulsed APT [165, 166] and leads to an overestimation of the other elements. Since carbon contents deviate strongly from the average content in the alloy, this is not taken into account in the present analysis. Also, locally increased chromium contents due to macro- or micro-segregation from casting can cause deviation from the nominal values [167, 168]. The arrows (purple and green) in Figure 5.2 (b) denote datasets of similar grain sizes (9±1.5 and 12.7±4.7 nm) that exhibit strongly differing chromium compositions (1.7 and 3.8 at%). These data points show that extremely small grain sizes can coexist with both high and low amounts of chromium being present.

5.4. Origin of carbon and chromium peak compositions in WEAs

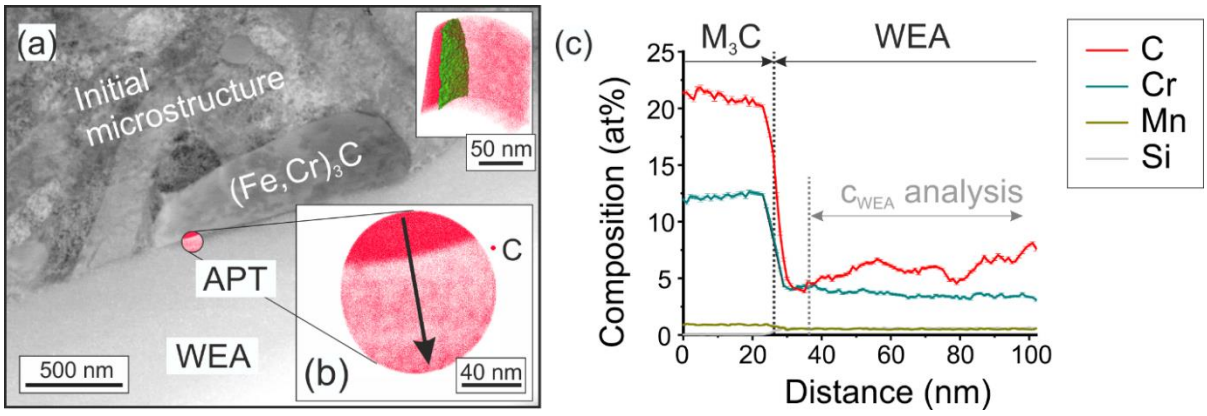

Figure 5.3: Composition of decomposing $(Fe,Cr)_3C$ and adjacent WEA: (a) SEM-BSE image of WEA and a partially decomposed cementite precipitate. (b) 20 nm thick slice from the reconstructed APT probe volume along the WEA-cementite interface (shown in the inset in (a)). (c) 1D composition profile across the $(Fe,Cr)_3C$-WEA interface along the arrow in (b). c_{WEA} analysis corresponds to the region of interest for determining the matrix carbon content.

Figure 5.1 and Figure 5.2 (a) show that in some positions, the local carbon content in WEAs significantly deviates from the nominal alloy composition. Next, the origin of these high carbon contents that are (in some cases) also accompanied by high local chromium contents, is addressed. Such measurements originate from WEA locations that are in the immediate vicinity of decomposing spheroidized $(Fe,Cr)_3C$ cementite precipitates. The data point that is marked by a green arrow in Figure 5.2 stems from such a location, as shown in Figure 5.3, which is an SEM-BSE micrograph revealing

fine WEA right next to a partially decomposed $(Fe,Cr)_3C$ cementite precipitate. The 20 nm slice of the APT measurement depicted in Figure 5.3 (b) captures the WEA-$(Fe,Cr)_3C$ interface and shows all detected carbon atoms. A 3D carbon map is shown in the inset and highlights the interface between matrix and precipitate by a 12 at% carbon isocomposition surface. Figure 5.3 (c) shows a 1D composition profile along the arrow in (b) and demonstrates the highly confined decomposition process that is reflected in the sharp decrease in the carbon and chromium profiles at the interface. The plateau of the elevated chromium and carbon profiles corresponds to the intact $(Fe,Cr)_3C$ precipitate. The carbon content in the adjacent WEA lies in the range of ~4-7 at%, whereas the amount of chromium steadily decreases from the interface into the matrix volume. For the highest accuracy in composition determination, smaller sub-volumes were individually analyzed, which includes individual ranging of the mass spectra and peak deconvolution [169]. This analysis reveals a carbon content of ~ 23.9 at% (stoichiometric value 25 at%), a chromium content of ~12 at % inside the $(Fe,Cr)_3C$ cementite precipitate, and an average carbon content of ~ 6.7 at% in the WEA about 10 nm and further away from the interface. The respective section is marked with a grey line in the 1D composition profile in Figure 5.3 (c). This observation clarifies the origin of simultaneously high carbon and chromium contents in WEA. These are present in the direct vicinity of decomposing or decomposed $(Fe,Cr)_3C$ cementite precipitates. Conversely, very high carbon contents in conjunction with lower chromium contents can be found as represented by the data set that is marked by the magenta arrow in Figure 5.2 (b). In contrast to the Cr-rich spheroidized cementite precipitates, the smaller carbides (transition carbides and cementite) are not enriched in chromium [170]. Thus, the decomposition of such temper carbides can result in WEA with high local carbon contents and correspondingly small grain sizes without increased chromium content. Carbon atoms stabilize the ultrafine ferritic grains by segregating to GBs, while chromium atoms do not primarily interact with microstructure defects. In consequence, it is the local carbon content that determines the corresponding grain size in WEAs and not the chromium content.

5.5. Carbon partitioning between grain boundary and grain interior

5.5.1. Qualitative analysis

The focus has thus far primarily been put on the correlation between grain size and local carbon content in WEAs. In the following, the partitioning of carbon in WEAs between GB and grain interior for a given local carbon content ($c_{C,WEA}$) and a given ferrite grain size is described. Carbon at GBs is also designated interfacial excess (Γ) and carbon in the bulk of ferrite grains is denoted as grain interior carbon content ($c_{C,gi}$). The separation of the total carbon content into these two contributions is illustrated by the 2D carbon content maps from APT measurements shown in Figure 5.4. The displayed

data stems from the same APT measurements as depicted in Figure 5.1 but are now quantitatively displayed in Figure 5.4. Note that the color codes in Figure 5.4 (a-c) and (d, e) are scaled differently due to the much higher average carbon content in Figure 5.4 (d, e). In Figure 5.4, GBs are visible as carbon-enriched regions, while, in comparison, the grain interior is carbon-depleted. With increasing total carbon content, an increase of both the carbon content in the grain interior and as interfacial excess is evident from Figure 5.4 (a-e). Note that in the case of Figure 5.4 (e), the grain size is smaller than 10 nm, so that it becomes challenging to clearly differentiate between GBs and grain interior.

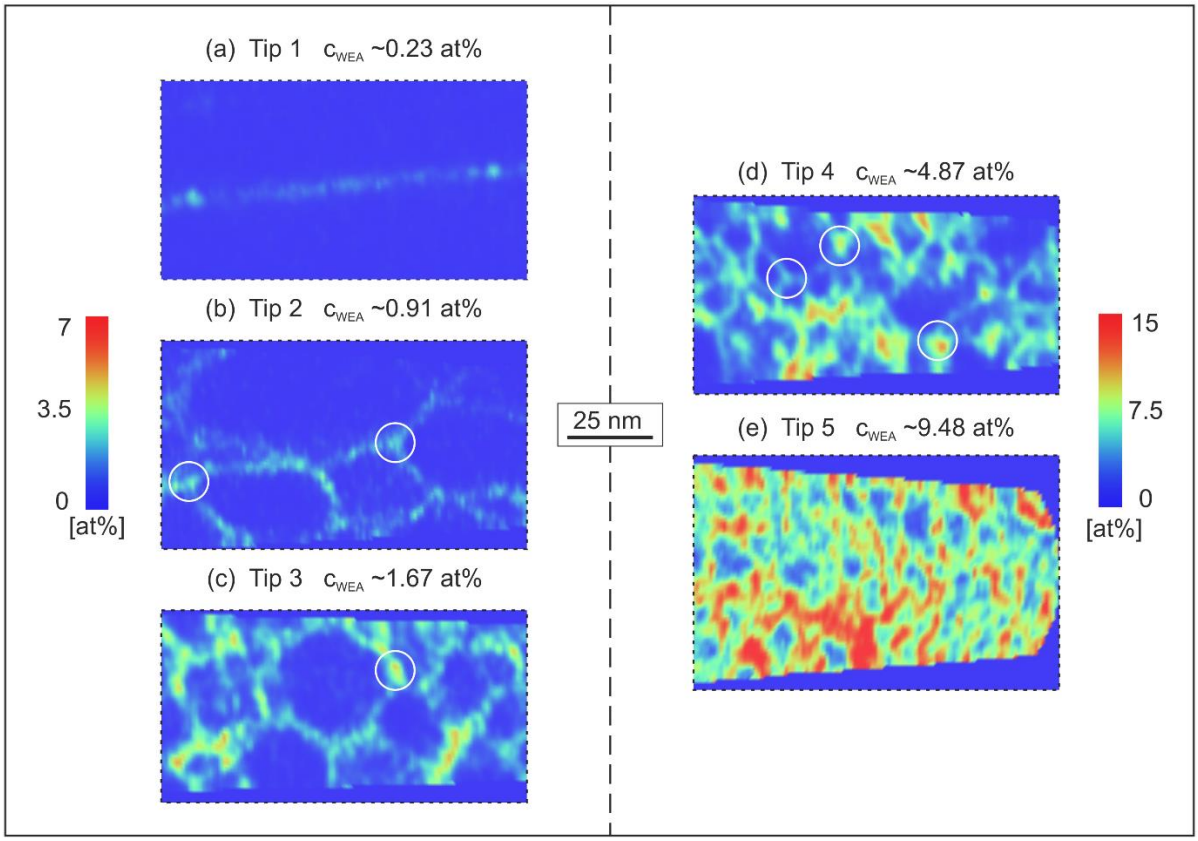

Figure 5.4: Partitioning of carbon between GBs and grain interior: 2D carbon content maps from segments of the APT reconstructions shown in Figure 5.1(a), (b), and (c) show segments of tips 1, 2, 3 with the same color-coding. Subfigures (d) and (e) depict segments of tip 4 and 5 with adjusted color-coding because of elevated $c_{C,WEA}$. An increase in carbon at GBs as well as in the grain interiors with rising total carbon content is observed. Additionally, carbon is enriched beyond the GB content at some triple junctions (white circles in (b), (c), and (d))

5.5.2. Quantitative analysis, limitations, and measurement artifacts

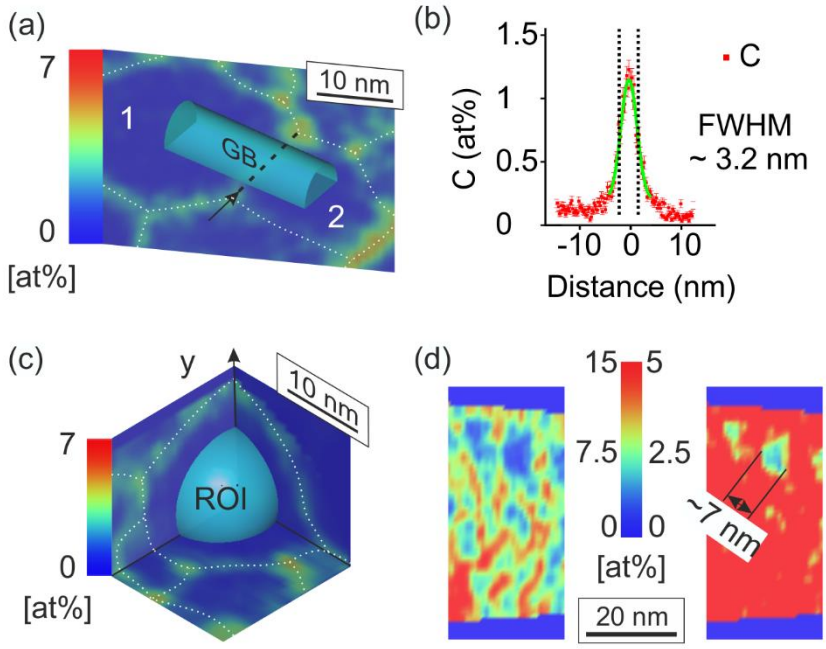

Figure 5.5: Quantification of GB excess carbon and carbon grain interior content. White dashed lines in (a) and (c) mark GBs. (a) cylindrical ROI across a GB (dashed black line) between grains 1 and 2 in tip 3. (b) depicts a 1D composition profile across the HAGB in tip 1 (Figure 5.1(e)) with prominent enrichment of carbon at the GB up to ~1.3 at% (ROI diameter 15 nm) The FWHM was calculated to be ~3.2 nm, and the peak width is at least about ±5 nm across the GB. Subfigure (c) displays an example of an ROI from tip 3 used to determine the grain interior carbon content; (d) shows 2D composition maps from tip 5 in Figure 5.4 (e) where the diffuse carbon profiles across GBs start to overlap in the grain interior.

Average values of interfacial excess and carbon grain interior content were determined from five reconstructed APT volumes covering a range of total carbon contents between ~ 0.23 at% and ~ 9.48 at% with the respective mean grain size ranging from 380 ± 156 nm to 9 ± 1.5 nm. The obtained values are summarized in Table 5.1. The procedure of carbon interfacial excess determination is illustrated in Figure 5.5 (a). It shows a cylindrical volume across a GB marked by a dashed black line used for interfacial excess calculation along its axis. The 1D carbon content profile along this axis is then used to calculate the interfacial excess by means of a so-called 'ladder' diagram [26]. The bin size was 0.5 nm, and the position of the interface was defined as the position where the composition profile deviates from the constant bulk composition.

The amount of interfacial excess depends on the GB misorientation [171], and hence individual GBs will naturally experience different amounts of carbon segregation. Low-angle GBs (LAGBs) are built up of dislocations, which attract carbon atoms analogous to Cottrell atmosphere formation in the bulk

lattice. As the dislocation density in the LAGB plane is linked to the misorientation between adjacent grains, carbon segregation increases with increasing misorientation. Note that the in-plane distribution of segregating solutes at LAGBs is strongly inhomogeneous, as discussed by Jenkins et al. [172], who report a 6-fold scatter in the GB excess using the approach for the same LAGB (< 1°) depending on whether the region of interest across the GB included a dislocation or not. Ferrite grains in WEAs, are mostly separated by HAGBs. Random HABGs accommodate most carbon atoms because of large interatomic spacing within the GB volume. However, high lattice coincidence (e.g., across twin boundaries) significantly decreases the amount of carbon segregation.

To evaluate the scatter of carbon segregation to a single GB, the interfacial excess was determined at four random positions using 20 nm diameter cylindrical ROIs for the HAGB in tip 1 displayed in Figure 5.4 (a) (this HAGB is also visible in Figure 5.1 (e)). Obtained values scatter between approximately 2 and 5 atoms/nm^2. For best possible accuracy, the ROI is constructed as large as possible across a planar segment of the GB. For example, if the ROI is extended to cover 85x72 nm^2 (i.e., ~ 19 times the area of the cylindrical ROIs) of grain boundary area, the interfacial excess yields ~4.4 atoms/nm^2, and the FWHM of the carbon content profile across this interface is only slightly larger than from a cylindrical ROI of 15 nm diameter (~3.9 nm compared to ~3.2 nm in Figure 5.5 (b)).

For increasingly smaller grain size, it is not possible to use multiple ROIs for the interfacial excess analysis of a single GB due to the spatial constraints (usually, the area is several tens of nm^2). However, the number of GBs in the reconstructed volume and average values from a number of GBs in each tip are calculated. As no information about the local GB crystallography is available, interfacial excess values obtained from each tip are averaged, which is assumed to be representative of the individual tips. In the smallest grain size regime, only a small number of GBs establish planar sections making a reliable determination of the interfacial excess increasingly difficult. The values obtained by this methodology are presented in Table 5.1. They are in a range of ~3-19 atoms/nm^2, showing a high scatter, especially for the smallest grain sizes (< 15 nm). Comparison to literature values can only be made in a qualitative manner due to the differences in microstructure as well as the locally different chemical composition. In [171], cold-drawn pearlitic wires with similar nominal carbon content (4.4 at% C, tempered for 2 min at 400 °C) were investigated, and values of Γ across random HAGBs were found to be in in the range of ~ 4-16 atoms/nm^2 with a mean of 8.4±3.2 atoms/nm^2. This mean value originates from 79 HAGBs in a columnar nanocrystalline ferritic structure with a grain size of ~ 30 nm normal to the drawing direction and is similar to the present results for the grain size range from ~ 20-30 nm in tip 2 and 3, with 4.6 ± 1 and 8.3 ± 7.3 atoms/nm^2, respectively. For smaller grain sizes (< 15 nm) that are accompanied by significantly higher local carbon contents, the interfacial excess reaches higher values

(tip 4 and 5 with 16.3 ± 5.2 and 14.4 ± 2.7 atoms/nm^2). In a simplified approach, the maximum coverage of a GB is assumed to be in the range of about one monolayer [154, 158]. Here, interfacial free volume and additional strain around the GB [126] (which increases the amount of carbon that can stay in solid solution) are neglected [157]. Assuming then, a GB to be a two-dimensional plane, this amounts to ~12 and ~14 atoms/nm^2 in the case of ferrite (100) and (111) surfaces/GBs. The latter of these was found to be the saturation value on free ferrite (111) surfaces [145]. The highest measured interfacial excess values in the present work (16.3 ± 5.2 and 14.4 ± 2.7atoms/nm^2) are close to those for idealized monolayers. They are also clearly higher than the values reported in the literature.

Next, the quantification of grain interior carbon contents was carried out. Figure 5.5 (c) illustrates one example of a ferrite grain in tip 3. In order to avoid any incorporation of segregated carbon from GBs (the interfacial excess) into the analyzed volumes for the grain interior, sub-volumes were separated as follows: 2D carbon content maps were used to specify the dimensions of ellipsoids such that these only include the grain interior staying ~5 nm away from the GBs (indicated by dashed white lines in Figure 5.5 (c)). An average grain interior content ($c_{C,gi,m}$) for each tip was then calculated as the mean value of four to eleven grains (see Table 5.1). Figure 5.5 (d) shows a 2D carbon content map of a segment from tip 4. It demonstrates that the carbon content exceeds 5 at% in almost the entire region. This is largely due to the local magnification effect [173], which causes delocalization of carbon atoms by several nm in the reconstruction as compared to their initial position at GBs. However, grains in the present size regime do not contain large amounts of dislocations [174, 175] or vacancies (fraction of 10^{-5}-10^{-4} in severely deformed ferrite [176]), and therefore could not account for such high carbon contents. The delocalization is illustrated by the 1D composition profile along the longitudinal axis of a 15 nm diameter cylindrical region of interest (ROI) across a high angle (HAGB) in Figure 5.5 (d), where the FWHM of the peak of carbon enrichment at the GB is ~ 3.2 nm. Although an actual width must be ascribed to the GB (~ 1-2 nm [177]), the remaining aberration in the 1D composition profile is caused by the local magnification effect, which causes an artificial broadening of the carbon locations. When comparing the measured width of the carbon segregation zone and the grain size, it becomes evident that such GB composition profiles begin to significantly overlap with the grain interior if grains are smaller than ~10 nm. Also, the sub-volumes for calculating $c_{C,gi}$ become as small as ~ 12 nm³ and are hence subjected to larger errors due to limited counting statistics. The mean value of 1.1 ± 0.3 at% (tip 5) for $c_{C,gi}$ was obtained in the smallest grain size regime by carefully defining non-overlapping sub-volumes of a small number of grains for which the approach was applicable. Due to this limitation, only measurements on grains larger than 10 nm are possible; it is therefore not clear whether smaller grains contain even more carbon. This value is in close agreement with the value of 0.9 ± 0.2 at%,

which has been obtained in a comparable nanocrystalline ball-milled Fe-C alloy with a total carbon content of ~6.2 at% and mean grain size d_m= 7.5 nm material [124]. The latter value was determined through the change in the ferrite lattice parameter obtained from X-ray diffraction (XRD) experiments. This method avoids the difficulty in the present approach, where a clear distinction between GB and bulk is challenging for the smallest grain sizes. WEAs investigated in the present work are not accessible by XRD because they are small, irregular-shaped volumes that cannot be extracted in appropriate dimensions for integral XRD measurements.

Table 5.1: Summary of carbon partitioning between GBs and grain interior in WEAs based on the five APT reconstructions depicted in Figure 5.1 and Figure 5.4.

Tip no.	d_m *(nm)*	$c_{C,WEA}$ *(at%)*	$c_{gi,m}$ *(at%), average of* c_{gi}	Γ*, (at nm*$^{-2}$*), average*
1	380±156	~ 0.23	0.11±0.08	4.4
2	32.1±16.9	~ 0.91	0.21±0.12	4.6±1
3	22.1±8.1	~ 1.67	0.41±0.13	8.3±7.3
4	15±4.7	~ 4.87	0.82±0.44	16.3±5.2
5	9±1.5	~ 9.48	1.1±0.3	14.4±2.7

5.5.3. Evolution of carbon interfacial excess and grain interior carbon content with total carbon content

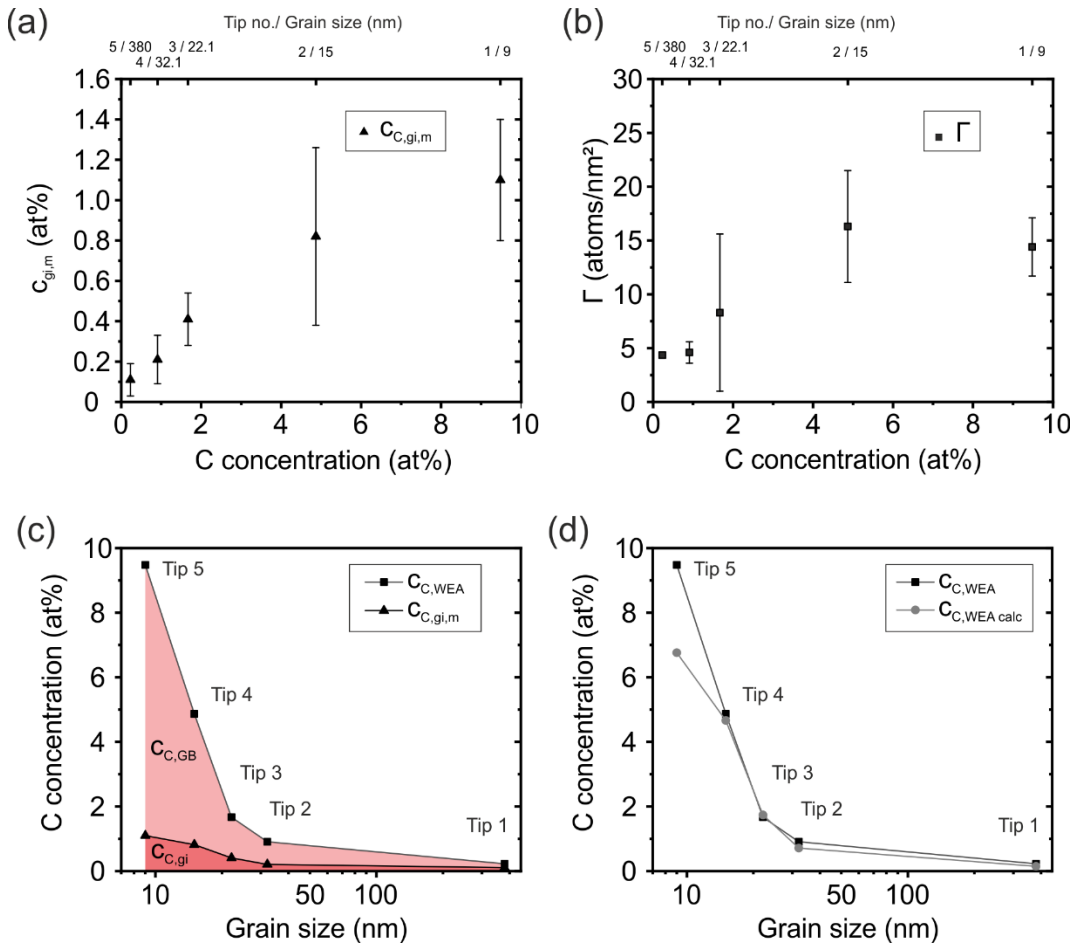

Figure 5.6: Quantification of carbon partitioning between grain interior and GBs: plots of (a) carbon content in the grain interior $c_{C,gi,m}$ and (b) interfacial excess Γ over average carbon content $c_{C,WEA}$ in five reconstructed APT volumes. The APT tip numbers and the measured grain size are indicated above the plots. The plot in (c) provides an overview of the contributions of the carbon at GBs and in the grain interior to the total content inside a WEA tip. A comparison between the total measured carbon content in WEAs and a comparison between the values calculated with the values from APT analyses ($c_{C,gi,m}$, d_m, and Γ_m) is shown in (d).

In Figure 5.6 (a), the averaged values for the grain interior carbon content are plotted over the average carbon content of the respective APT measurement. Figure 5.6 (b) is a plot of interfacial excess (squares) over the average carbon content for the respective APT volume. Figure 5.6 (a) shows that the grain interior carbon content initially rises approximately linearly with increasing average carbon content in the WEA. Towards higher WEA carbon contents, the increase becomes significantly less and appears to exhibit asymptotic behavior, while a clear saturation value cannot be derived from the presented data. A similar trend is observed for interfacial excess values, as shown in Figure 5.6 (b). Here, it is

noteworthy that the measured value of the interfacial excess for the WEA with the highest carbon content (tip 5, 9.48 at% C) is lower than the one determined from a WEA with only half the carbon content (tip 4, 4.87 at% C). This is likely due to the mentioned limitations of APT, and hence the apparent value of the interfacial excess might be reduced due to a false increase of carbon inside the grains. Some triple junctions are observed to show higher carbon segregation than the GBs close to them, as seen in Figure 5.4 (b)-(d). Such a tendency cannot be observed in tip 5 in Figure 5.4 (e) due to the limitations discussed. It is, however, reasonable to expect that the large number of triple junctions accommodate significant amounts of carbon and, therefore, the trend of increasing interfacial excess does not continue in the same manner.

Figure 5.6 (c) is a plot of the grain interior carbon content (triangles) and the total carbon content of the respective WEA (squares). The area underneath the connected values visualizes the contribution to the total carbon content. The fraction of grain interior carbon decreases with increasing average carbon content. In tip 1, about half of the carbon is located inside the grains and the other half at the GB, while in tip 3 ~ 25 % of carbon atoms are located at GBs, and in tip 5 finally only ~12 % of the total carbon remains in the grain interior the majority hence being situated at GBs. The strongest influence – especially towards small grain sizes – is exerted by the reduction in grain size since the GB area/volume is proportional to its inverse. In other words, GBs dominate the accommodation of carbon with increasing total carbon content in WEAs. The plot in Figure 5.6 (d) provides a comparison of the average carbon value of each tip as measured on the entire APT tips with the one calculated[10] using the individual parameters ($c_{C,gi,m}$, d_m, and Γ_m) obtained from the individual data sets (see Table 5.1). An approximate agreement can be observed for tips 1-4. The calculated value for tip 5 yields a clear underestimation, which is likely caused by an underestimation of the interfacial excess due to APT artifacts discussed above.

5.5.4. Thermodynamic considerations

The nanocrystalline microstructure of WEAs is a result of severe plastic deformation [27, 102]. Large numbers of vacancies, dislocations, and grain boundaries are created during this process and provide the driving force for subsequent recovery, recrystallization, and grain coarsening [178]. However, carbon atoms can stabilize such defects in WEAs [124, 179]. Carbon segregation lowers the defect energy and hence reduces the driving force for recovery, recrystallization, and grain coarsening. This effect is best illustrated through comparison with severely deformed pure iron. The smallest grain size that was obtained in high purity iron by high pressure torsion is about ~ 300 nm, as the high defect

[10] This calculation is performed using a simple mass balance equation: $c_{C,WEA} = c_{C,gi} + \frac{3\Gamma}{d_m}$

densities cause dynamic recrystallization during deformation [156]. Conversely, adding only ~ 2 at% carbon results in stabilization of grain sizes of ~ 20 nm after ball-milling and annealing [124]. Higher carbon contents inhibit grain coarsening of the nanocrystalline Fe-C alloys even at moderately elevated temperatures [124].

The theoretical concepts of thermodynamic grain size stabilization by solutes (as opposed to kinetic inhibition of grain growth as described by Cahn [180]) were first formulated by Weissmüller [157, 158]. Kirchheim extended this theoretical framework and described the general stabilization of defects by solutes [159, 160]. These concepts are based on the Gibbs adsorption isotherm and assume a dilute solution, saturation of GBs, and suppressed precipitation of additional phases. In general, an increasing total solute content leads to increased solute segregation to interfaces as well as increased solute content in the grain interior. However, the amount of carbon that can be accommodated in ferrite and at GBs is limited. According to Weissmüller [157], a thermodynamically metastable equilibrium state with representative grain size is obtained when the interfacial excess reaches a saturation value, and solute contents at the GB and in the grain interior are in thermodynamic equilibrium. Such a metastable equilibrium can be reached through grain growth towards a specific equilibrium grain size, if kinetically possible. Upon grain growth, the total GB area decreases and, accordingly, the amount of solute per GB area increases towards the saturation value of interfacial excess.

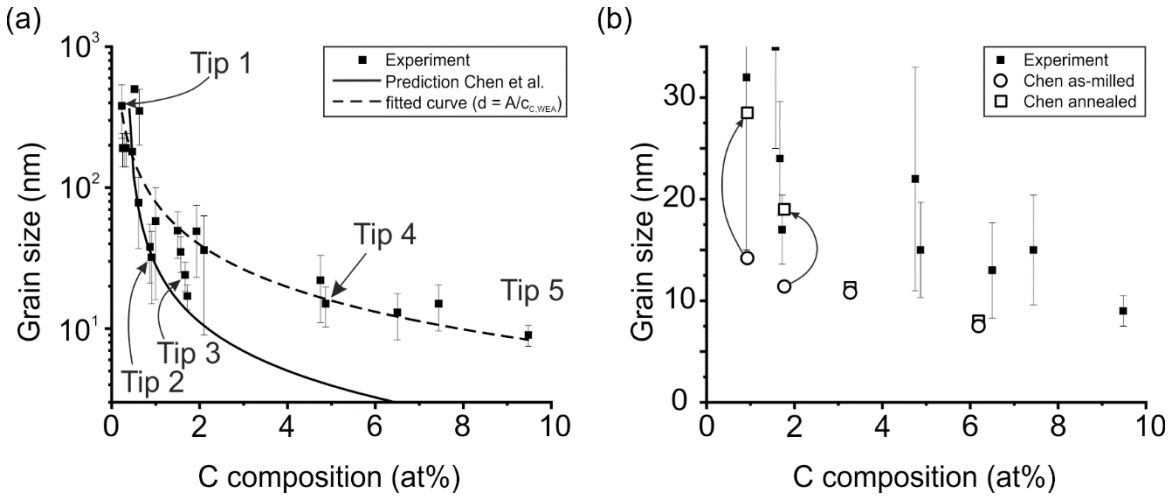

Figure 5.7: Grain size over total carbon content. All experimental values from APT analyses are plotted as filled squares in (a), while only such with grain sizes smaller than 35 nm are shown in (b). The solid line represents a quantitative prediction of grain size by Chen et al., while the dashed line is a fitted curve with a single parameter (A ~ 79). Subfigure (b) includes some data points (open symbols) from ball-milled Fe-C alloys of Chen et al. in the as-milled and annealed condition.

Figure 5.7 (a) shows a plot of grain size over total carbon composition for all obtained APT data sets in this chapter, while (b) only shows data points with grain sizes smaller than 35 nm. The dashed line

Figure 5.7 (a) is a fitted curve that does not have a physical basis. It is, however, useful for a rough estimation of carbon contents inside WEAs when only the grain size can be determined, and compositional analysis cannot be performed, as is usually the case. In addition, a solid curve used to describe metastable equilibrium conditions in Fe-C alloys obtained by Chen et al. is shown.

While there is a reasonable agreement for low carbon contents (< 2 at% C), deviations between the prediction and the experimental values are obvious in the higher carbon regime (>3 at% C). This is because in high carbon WEAs grain interior carbon content and interfacial excess (refer to Figure 5.6) increase well beyond the saturation values assumed by Chen et al. in their prediction [11] (Γ = 7.8 atoms/nm^2, $c_{C,gi,m}$ = 0.35 at% C, compare with *Table 5.1*). The deviation is related to the fact that solute-solute interactions come into play at higher carbon contents, rendering the assumption of a dilute solution invalid. The dilute solution assumption, however, is a precondition in the mentioned thermodynamical models. A comprehensive quantitative description based on the invoked concepts, therefore, fails in the present scenario. Conversely, excellent agreement between some WEA data points (which were only exposed to typical bearing operation temperatures ranging between 60-90 °C) with the Fe-C model alloys (which had undergone a heat treatment of 1 hour at 300°C after milling to reach equilibrium conditions) are found as shown in Figure 5.7 (b) and Table 5.2. Open symbols in Figure 5.7 (b) represent the data from Chen et al. (circles: as-milled; squares: annealed). The low carbon model alloys (< 2 at%) exhibit grain growth upon annealing (see arrows in Figure 5.7). The final grain sizes are comparable to the ones found for some WEAs with similar carbon contents.

Table 5.2: Comparison of carbon content and accompanying grain size in WEAs and ball-milled and annealed Fe-C model alloys.

WEAs		*Fe-C model alloys (300 °C/1 h)*	
$c_{C,WEA}$ (at%)	d_m (nm)	$c_{C,tot}$ (at%)	d_m (nm)
0.91	32	0.93	28
1.72	19	1.77	17

In the case of carbon contents > 3 at%, where the Fe-C model alloys – which are assumed to be in equilibrium – exhibit smaller grain sizes than WEAs of similar carbon content (see Figure 5.7 (b)), it remains unclear how an equilibrium state could be reached. A reduction in grain size or a lowering of the carbon content would be necessary to reach values similar to the model alloys (i.e., equilibrium

[11] This prediction is made using a rearranged form of the mass balance equation used before: $d_m = \frac{3\Gamma}{c_{C,WEA} - c_{C,gi}}$.

condition). The first case cannot be brought about without further grain refinement, and the latter makes massive carbon diffusion necessary. Such high carbon WEAs might therefore be stable due to kinetic limitations. In these WEAs, interfacial excess and carbon grain interior content are then expected to exceed equilibrium values, and kinetic limitations only allow the establishment of local equilibria between grain interior and boundaries, not for carbon redistribution over larger distances by diffusion. That kinetic limitations play a role here is indicated by the fact that although very high carbon contents of almost 10 at% are found, no carbide precipitation was observed

As shown in Section 5.4, high carbon WEAs originate from decomposing cementite precipitates. It is caused by severe plastic deformation, which can be viewed as 'non-equilibrium processing' accordingly leading to non-equilibrium microstructures. The present high local carbon contents are approached from even higher values (25 at%) and decrease as carbon is redistributed during ongoing deformation. Thus, the formation mechanism is different from the processing route applied by Chen et al., which is based on ball milling of iron and graphite powders. Here, the amount of carbon contained in the alloy is accommodated by defects created through deformation, i.e., carbon is being taken up as defect density increases. Heterogeneity in terms of carbon distribution throughout different segments of WEA is significantly more pronounced than in the largely homogenous nanocrystalline microstructures obtained by ball milling. This is a consequence of the directional carbon redistribution through inside WEAs and the low temperatures strongly restricting diffusional homogenization.

In conclusion, it is shown that nanocrystalline WEAs – which formed in bearings during service in the technical alloy 100Cr6 – are stabilized by carbon. Close agreement with model experiments indicates that stabilization in this regime can be thermodynamic for some WEAs with low carbon contents (i.e., equilibrium grain sizes are locally present). The conditions of WEAs with carbon contents higher ~ 4 at% are more complex. While GB energy is surely lowered in all cases by carbon GB segregation here, the presence of equilibrium states is likely not reached, and GBs are even oversaturated. Temperatures in bearings are not high enough to reach metastable thermodynamic equilibrium states – if these indeed exist – throughout the entire volumes of WEA. The predicted relationship of total carbon content and grain size based on simplified thermodynamical models cannot be applied in the case of WEAs. More complex models that take solute-solute interactions into account and allow for increasing interfacial excess to increase with increasing total solute content (i.e., there is no saturation of GBs) would need to be employed. These models, however, rely on thermodynamic data that are not readily accessible.

5.6. Implications for WEA-WEC formation mechanisms

The presented APT results confirm EPMA investigations are revealing carbon depletion in large portions of WEAs with respect to the nominal composition [113, 119-122]. Here, this effect was investigated in a quantitative manner on the sub-µm scale, and an inversely proportional relationship between local grain size and local carbon content is reported. The highest local carbon contents and smallest grain sizes are found next to decomposing cementite precipitates, which act as carbon sources. In contrast, the coarsest grain sizes are observed in the most carbon-depleted areas.

The previous Chapter 4 attempts to explain the origin of local carbon depletion in WEAs. Crack surface rubbing leads to the decomposition of the surrounding microstructure. In addition, WECs are continuously exerting influence on both matrix and WEA, which leads to the decomposition of the matrix and further deformation inside WEAs. During these processes, WECs collect carbon, thereby reducing friction between crack surfaces, which can potentially accelerate crack propagation. Upon continued reciprocating sliding of crack surfaces, residual nm-sized carbon deposits are incorporated into WEAs. Certain regions inside WEAs are correspondingly depleted in carbon. Here, less carbon is available to stabilize initially nanocrystalline WEAs, and grain coarsening takes place at bearing operating temperatures. This clearly shows the importance of the element carbon for the WEC phenomenon, which relies on these mechanisms that would not take place without its presence. Thus, ample evidence is provided that carbon plays a crucial role in the WEC phenomenon. The question why the WECs bind more carbon in some regions of the WEAs than in others (e.g. in the form of carbon deposits) – which leads to different corresponding grain sizes – still requires further investigation.

5.7. Conclusions

WEAs consist of ferritic grains with grain sizes ranging from several hundred to a few nanometers. Carbon distribution in WEAs with different grain sizes was analyzed by means of APT measurements, and the following conclusions are drawn:

- The local carbon contents and local grain sizes in WEAs are inversely related. This means that large-grained WEAs contain low carbon contents and vice versa. High chromium contents can remain in high carbon areas after decomposition of spheroidized cementite, but carbon is ultimately responsible for grain size stabilization in WEAs through extensive GB segregation.
- The total WEA carbon content partitions between carbon atoms segregated at GBs and bulk carbon in the grain interior. Both - interfacial excess and grain interior carbon – continuously increase with increasing total carbon content. Even in the regime of highest carbon contents (> 5 at% C) still a continued slight increase in both quantities takes place. However, the

increase in GB area per volume with decreasing grain size is the prime factor for the accommodation of extremely high carbon contents up to 9.48 at% without precipitation of carbides.

- No uniform saturation values for interfacial excess and grain interior carbon content could be observed across the entire range of analyzed nano-ferritic WEAs. This means that the nano-ferritic microstructures in WEAs are not generally exhibiting equilibrium grain sizes as described by the models invoked. Only local diffusional equilibria between carbon in the grain interior and at GBs are established.
- The amount of local carbon depletion and the resulting grain size varies significantly across different segments of WEA. The extent of carbon depletion and thus the possibility of grain growth depends on the amount of carbon segregation to the WEC fracture surfaces and the concurrent formation of carbon deposits in WEA upon further crack rubbing.

Chapter 6 White etching area formation at the nanoscale: confined severe plastic deformation through crack rubbing

This chapter is based on a manuscript by Mayweg, D.; Morsdorf, L.; Herbig, M.: *White etching area formation at the nanoscale: confined severe plastic deformation through crack rubbing*, which is in preparation for submission to Acta Materialia.

6.1. Introduction

Recently, Morsdorf et al. [102] proposed a WEA formation mechanism. It aims to explain the microstructure transformation into nanocrystalline ferrite in terms of a combination of crack surface rubbing and partial rewelding of these surfaces, which leads to material transfer as the crack reopens during unloading. Crack surface rubbing is essentially understood as a small scale fretting process due to the shear stress reversal under superimposed compressive loading during rolling contact fatigue. During this very high cycle fatigue phenomenon, transfer of material during a large number of successive loading cycles WEC are displaced with respect to the crack plane**.** This mechanism is able to explain the often observed asymmetric arrangement of WEA around WECs. WECs are therefore described to not only propagate but also move through the microstructure as the original microstructure is decomposed and WEA is left behind.

This chapter presents structural and chemical characterization of WECs on the nanoscale. APT and electron microscopy are employed to investigate crack surfaces as well as interfaces between WEA and matrix. WEA is found on both sides of WECs, which supports the understanding that cracks need to be present and hence precede WEA formation. The interfaces include such between nanocrystalline WEA and bainitic ferrite as well as such between WEA and spheroidized $(Fe,Cr)_3C$ precipitates. Based on the presented results, it is argued that WEAs extend into the matrix on both at the WEA matrix interfaces on both sides of the cracks. Deformation of matrix and inside WEAs occurs via a combination of dislocation activity and potentially grain boundary sliding for grain sizes below 10 nm. Since cracks can partially reweld, transfer of material can occur during reopening.

6.2. Results

6.2.1. Distribution of WEAs around WECs

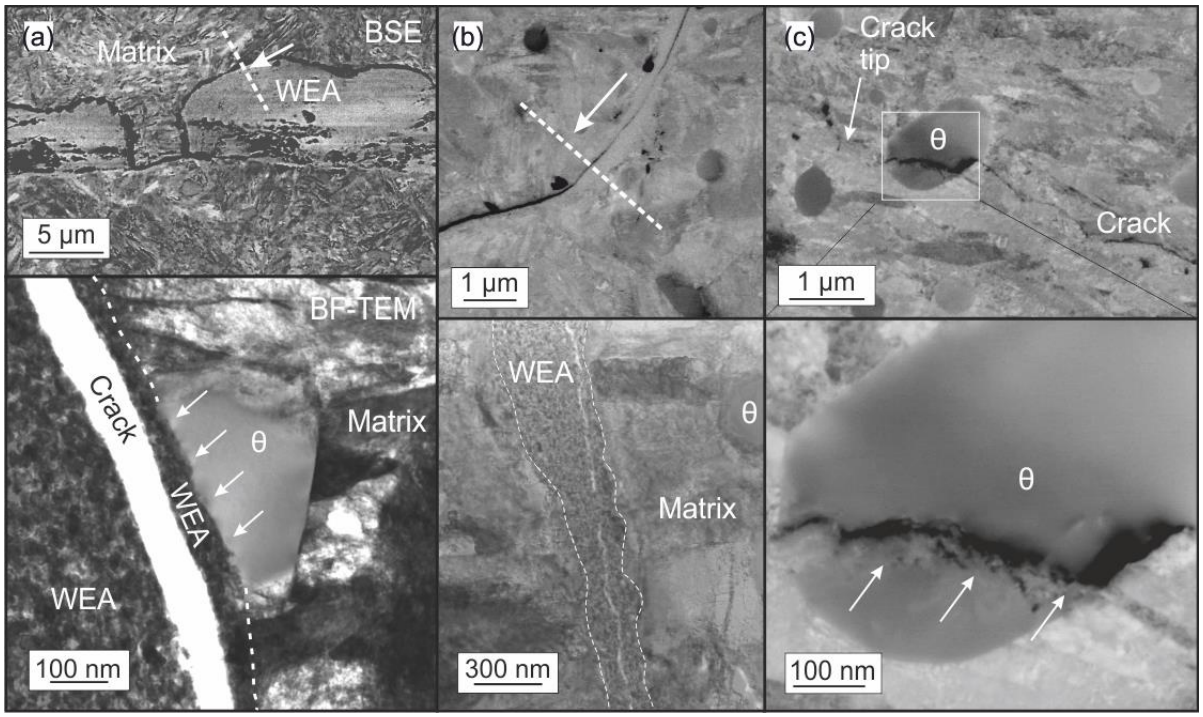

Figure 6.1: WECs with differing amounts and distribution of adjacent WEA. (a) BSE image of a WEC with asymmetric WEA, with ~ 5µm on one side and TEM image showing that a thin ~ 50 nm WEA on the opposite side as well. (b) BSE image of a WEC with narrow WEA (< 1 µm), the TEM image below shows WEA; smallest width of ~ 30 nm is found on the upper right-hand side. (c) BSE image of a WEC tip having propagated through a spheroidized $(Fe,Cr)_3C$ precipitate, which exhibits onset of decomposition as evident from the magnified view.

Figure 6.1 shows several SEM BSE and TEM images of WECs, which are bordered by varying amounts of WEA. Figure 6.1 (a) shows a portion of a WEC with a locally ~ 5 µm wide WEA, which appears to be only on one side of the crack. The region of the TEM lamella, which was lifted out from the position indicated in the SEM image and is depicted below, reveals that WEA is indeed present on both sides of the crack, albeit being only ~ 30-70 nm wide on one side. The spheroidized $(Fe,Cr)_3C$ cementite precipitate (θ) that is partially decomposed shows only minor signs of straining directly at the interface as pointed out by arrows. The WEC shown in the SEM image in Figure 6.1 (b) exhibits a much narrower WEA when compared to (a), which is more clearly visible in the TEM image below. Here too, the crack is asymmetrically decorated by WEAs as is especially visible in the upper part where WEA is only 10 nm wide on the right-hand side. Finally, in Figure 6.1 (c), a WEC tip is presented where the crack, even in the SEM BSE image, appears very narrow. The magnified view of

the spheroidized precipitate shows that the decomposition process has been initiated around the crack. This shows that the formation of WEA begins immediately after crack propagation.

6.2.2. Nanoscale crack morphology

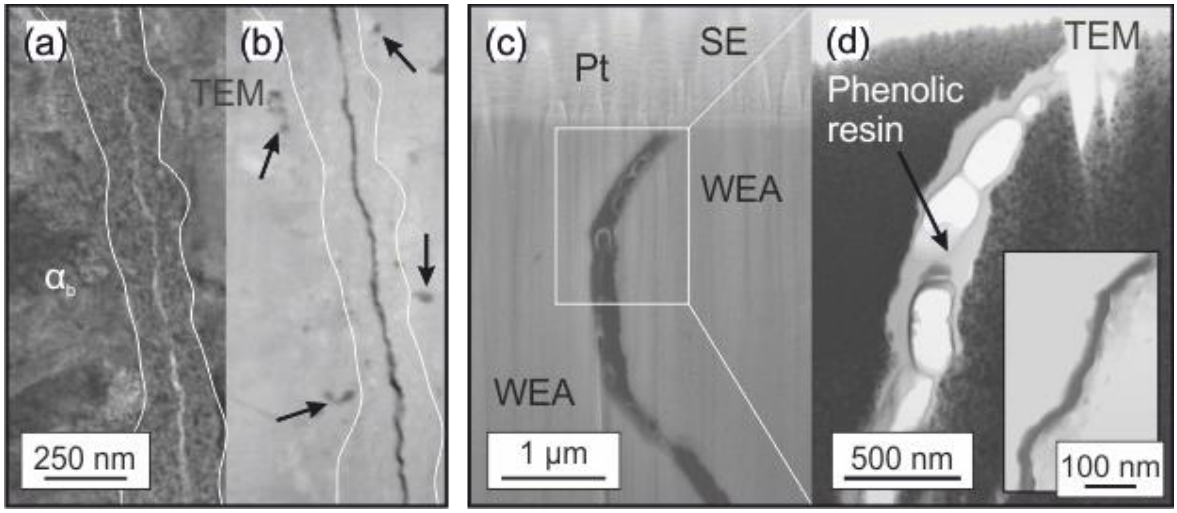

Figure 6.2: 2D morphology of sectioned WECs as observed in TEM. (a) BF and (b) HAADF STEM of the same segment of a narrow WEC. (c) SE image of a WEC with wide WEA during FIB preparation and (d) TEM BF and HAADF (inset) images of the region from the upper part depicted in (c). Note that the crack is filled with phenolic resin that was used to embed the sample.

Figure 6.2 shows micrographs displaying segments of two WECs. The crack depicted in Figure 6.1 (a) and (b) is only ~ 10 nm wide, and the WEA is very narrow (~200-300 nm). The depiction in (b) is a high angle annular dark-field (HAADF) STEM image, which is sensitive to density and proves that the crack is fully opened even if it looks like the crack surfaces have fused in the BF image in (a). In addition, Figure 6.2 (b) shows that the topology of the two crack surfaces in this section does not exhibit large asperities and sides fit together like puzzle pieces. It can also be observed that lower-density regions are present at the WEA-matrix interface (see arrows in Figure 6.2 (b)). Figure 6.2 (c) and (d) show images of a WEC that is much wider opened and surrounded by a several µm wide WEA on both sides. The SE image in Figure 6.2 (c) shows the platinum protection layer, which was deposited before FIB milling, and additionally provides evidence that the void between the crack surfaces is filled with matter. This material is phenolic resin, which was used for the embedding of this specific sample. In this case, it has the advantage that the crack surfaces are protected during FIB milling, and a section of the crack topography is preserved, as can be seen in the TEM micrographs. The crack opening at this position is roughly 200-300 nm. The two sides of the cracks fit together perfectly, as is especially

obvious from the HAADF inset[12]. This observation is remarkable in so far that WECs usually appear smooth, especially at moderate magnifications and due to edge artifacts even at 10,000-fold magnification in SEM, i.e., their morphology appears to be very different from faceted fatigue cracks (see Figure 3.4 and e.g. [181, 182]). The 2D crack morphology that is shown in Figure 6.2, however, shows that the profiles of two opposing WEC surfaces fit nearly perfect and that on the nanoscale, the cracks are facetted roughly in the order of individual WEA grains.

6.2.3. Confined plasticity at interfaces between WEA and matrix microstructure

Figure 6.3 (a) shows a BSE image of a WEC tip in a lower bainite matrix that consists of bainitic ferrite and carbides shown in the magnified inset on the lower left (marked with white arrows) and spheroidized $(Fe,Cr)_3C$ cementite (red outlines). These spheroidized cementite precipitates of ~ 0.5-1 µm diameter are single crystals and make up about 3-5 vol% of the material [170]. Cementite is significantly harder than bainitic ferrite. Fe_3C has a hardness ~ 1000 HV [183][13] and bainitic 100Cr6 yields about 780 HV [98][14]. The chromium enrichment will lead to a higher hardness of $(Fe,Cr)_3C$ in comparison to Fe_3C [184]. The spheroidized precipitates do not undergo a phase transformation during the bainitic reaction. This explains why the kernel average misorientation (KAM) is lower in cementite than in ferrite and has a lower spread, as can be seen in the graph in (d). These values were obtained from a larger area of several 1000 μm^2. The spheroidized precipitates grow ~ 10 nm during the transformation of the bearing material into lower bainite, i.e., they acquire a structure with a chromium-rich core ($(Fe,Cr)_3C$ with ~ 10-15 at% Cr) and a thin shell grown under near paraequilibrium conditions during the final heat treatment step that consists of Fe_3C without significant Cr partitioning due to kinetic restrictions. The metal sublattice composition is inherited from the austenite. The chemical composition of spheroidized ($(Fe,Cr)_3C$ precipitates is well defined and, they are single crystals. Any sign of plasticity or change in chemical composition can therefore be analyzed and used to discern the underlying mechanisms, which cause decomposition and hence transformation into WEA.

[12] In this image, the contrast was strongly enhanced to allow the clear identification of the edges. In addition, the HAADF image was cropped, and the crack surfaces are moved towards each other to make a comparison of their topology easier.
[13] Data obtained from bulk cementite.
[14] This value describes the average hardness of the lower bainitic microstructure, including bainitic ferrite and bainitic carbides, as well as spheroidized $(Fe,Cr)_3C$ precipitates.

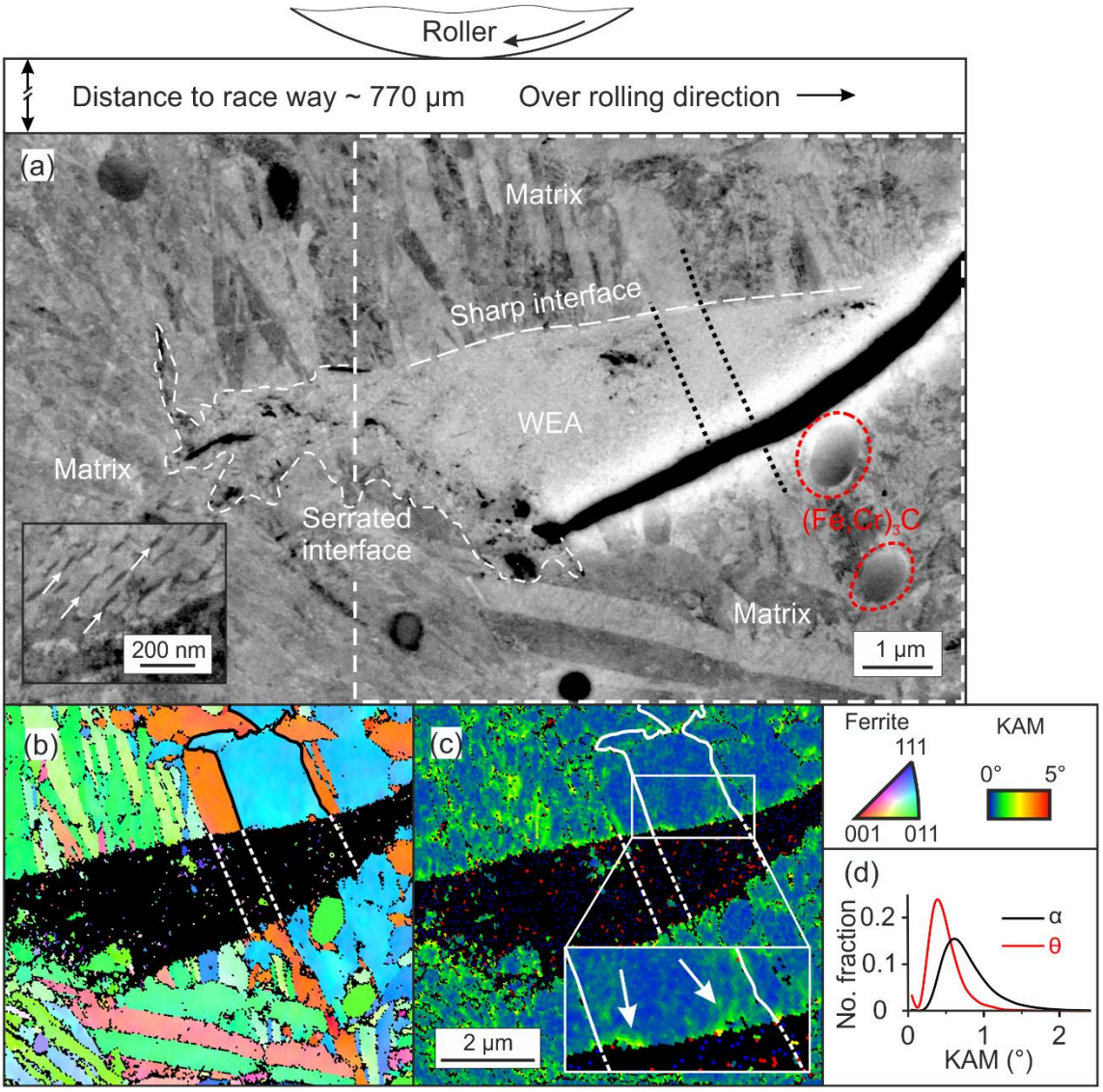

Figure 6.3: Comparison of initial microstructure and WEA around a WEC tip. (a) BSE image of a WEC tip within a bainitic matrix comprising bainitic ferrite and carbides (spheroidized $(Fe,Cr)_3C$ and bainitic carbides (inset)). The WEA-matrix interface, which is approximately parallel to the crack, is sharper than the one ahead of the crack. Subfigure (b) and (c) show EBSD IPF and KAM maps indicating higher misorientations at the sharp WEA-WEC interface when compared to adjacent bulk of the grain. The graph in (d) shows that ferrite exhibits higher KAM than $(Fe,Cr)_3C$.

The interface of WEA and matrix that is aligned parallel to the crack is comparatively sharp, while the interface ahead of the crack tip is not well defined. This can also be observed in the inverse pole figure (IPF), and the kernel average misorientation (KAM) maps in Figure 6.3 (b) and (c). There, the three white lines across the WEA represent the initial grain boundaries prior to the decomposition of the microstructure. One bainitic subunit above the WEA is outlined in black (b) and white (c). Assumed positions of the subunit grain boundaries are marked by white dashed lines. The map in (c) shows that in the center of the outlined grain, KAM values are comparatively low. Therefore, the higher values at

the WEA-ferrite interface (white arrows in Figure1 (c)) are related to the decomposition process. This narrow zone only comprises a limited amount of EBSD data points, and the spatial resolution in EBSD has to be taken into account as well. The step size used was 40 nm, which is in the order of the lateral resolution of iron at 15 kV acceleration voltage, which is 30-35 nm [185]. Since the vertical resolution is ~ 90 nm, due to the 70° tilt angle during EBSD measurements, it is not clear if the comparatively high KAM intensities at the WEA-matrix interface are reliable. For this reason, confirming results from orientation imaging in TEM are shown in the next section.

Interfaces between WEA and bainitic ferrite

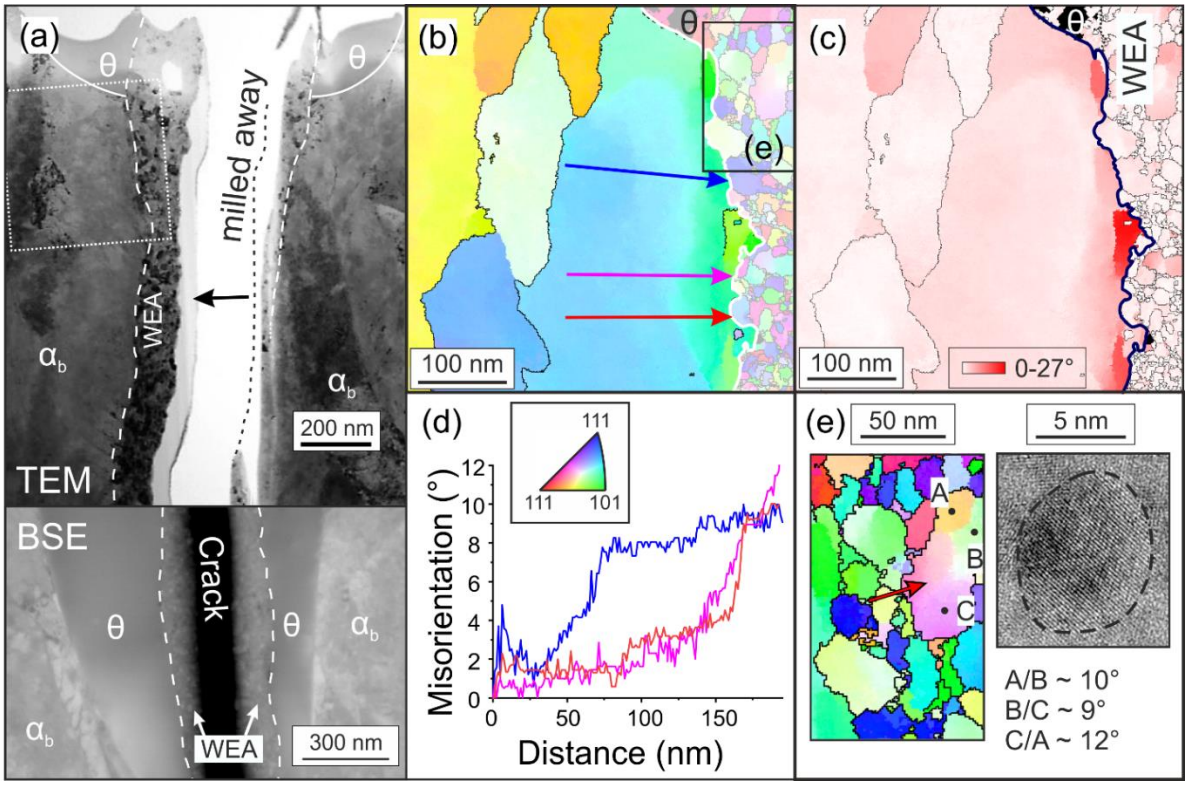

Figure 6.4: TEM investigation of WEA-matrix interface. (a) TEM BF image of a lamella lifted out from the position indicated in the BSE image below; ~ 50 nm layer of phenolic resin (marked by an arrow) the (b) and (c) IPF and GROD maps of the rectangular region marked in (a), HAGBs (< 15°) are marked by black lines; (d) misorientation profile; (e) magnified view of a region from (b) and HRTEM image of a ferrite grain (< 10 nm).

Figure 6.4 (a) shows images of a cracked spheroidized $(Fe,Cr)_3C$ cementite precipitate (labeled 'θ') that is partially decomposed directly adjacent to the crack. Here, nano-ferritic WEA has formed on both sides of the crack. This can be observed in the BSE image in the lower part as well as in the TEM BF image above, which depicts a TEM lamella cut across the crack and the precipitate. In the upper part, the two remaining segments of the precipitate are visible. While on the left-hand side, the WEA and

the crack topology are still visible, this is not the case on the right as the crack opened during FIB thinning and a fraction of the WEA was milled away. Figure 6.4 (b) is an IPF map from the region indicated by a white square in the upper left of (a). It spans across the interface between bainitic ferrite and WEA. It is clearly visible that the grains on the left show no intragranular orientation spread. The largest grain in the center, however, lying directly adjacent to the WEA, shows a significant change in coloring and hence higher misorientations. The presence of an orientation gradient is easily recognizable in the grain reference orientation deviation (GROD) map in Figure 6.4 (c) and in the misorientation profiles in Figure 6.4 (d). While it is obvious in the IPF and the GROD maps that the largest orientation changes are near the WEA, the profiles show that these reach 100-150 nm into the bainitic ferrite. The angular resolution of determining the orientation from spot diffraction pattern (here nano-beam diffraction) is around 2-3° [185] and inferior to EBSD. The template matching algorithm used for indexing might further lower this resolution [186]. The analyzed sample is thin[15], and the TEM used is equipped with a field emission gun that allows for a nominal probe size of 0.5 nm (measured probe size FWHM was ~ 1.5 nm). A step size of 1.25 nm was used for orientation mapping. It is, therefore, reasonable to assume an in-plane spatial resolution of the presented orientation maps of ~ 2-3 nm. This large improvement in comparison to EBSD observation makes it possible to assess the local misorientations more precisely. It is evident that plastic deformation occurs at the interface between WEA and bainitic ferrite. Figure 6.4 (e) is a magnified view of the region indicated by the rectangle in (b). It shows a segment of the WEA containing multiple grains. Small grains with sizes smaller than the lamella thickness cannot be reliably indexed due to overlapping spot patterns, which cannot be deconvoluted. However, grains with dimensions of several 10 nm can be indexed reliably. The largest grain depicted in (e) (see red arrow) exhibits several subgrains with orientation differences below 15°. The misorientations between the labeled points (A, B, and C) are listed in Figure 6.4 (e). The HRTEM image shows a grain, which is smaller than 10 nm, and does not appear to contain dislocations.

[15]The sample edge in this lamella close to the top is below ~ 40 nm thick as in a near two-beam condition no fringes were observed in ferrite {110} discs. Near the hole inside the WEA, the material was nearly fully amorphous due to FIB damage. Since amorphization occurs at the surface, this is further evidence of the low thickness.

Interfaces between WEA and spheroidized cementite

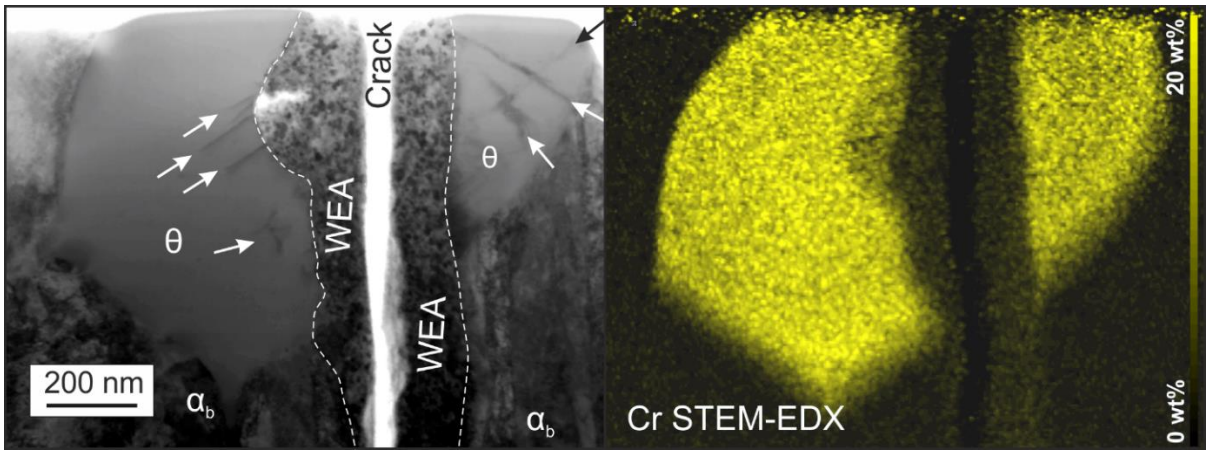

Figure 6.5: TEM investigation of a cracked spheroidized $(Fe,Cr)_3C$ precipitate that is partially transformed into WEA. (a) BF STEM image and (b) STEM EDX chromium mapping.

Figure 6.5 shows another case of a cracked spheroidized cementite precipitate, where WEA has formed at both crack surfaces. The arrows in Figure 6.5 (a) mark dislocations inside the cementite. Like in the WECs shown in Figure 6.1, the WEA formation is not perfectly symmetrical. Additionally, on the left-hand side, a region at the interface of WEA and precipitate a region of low mass thickness and therefore increased intensity is visible. The inset shows a SAD pattern from this region as marked by a circle. No reflections except the ferrite {110} ring are visible. This high-intensity region is not a hole, as was confirmed with higher resolution images (not shown). This leaves the presence of a void or carbon deposit (see Chapter 4) as the remaining possibilities. Since this lamella is comparatively thick, both of these could be contained within the material. Because of the thickness, EELS is not applicable, and EDX not sensitive enough for light elements, as discussed in Chapter 4. Furthermore, no enrichment of gallium or platinum could be detected by EDX, i.e., no redeposition has taken place during FIB milling. Since the region of interest is close to a decomposing precipitate containing 25 at% carbon, it is possible that a carbon deposit, as was shown in section 4.2.3 (see Figure 4.5), is present. The STEM-EDX chromium map in Figure 6.5 (b) clearly shows that the WEA is depleted in chromium as compared to the cementite but also exhibits larger chromium content than the adjacent unaltered bainitic ferrite, as also reported by Morsdorf et al. [102]. This means that a significant amount of chromium has been redistributed within the WEA over several µm. It can also be observed that the region around the presumed carbon deposit has higher chromium content than the WEA closer to the crack.

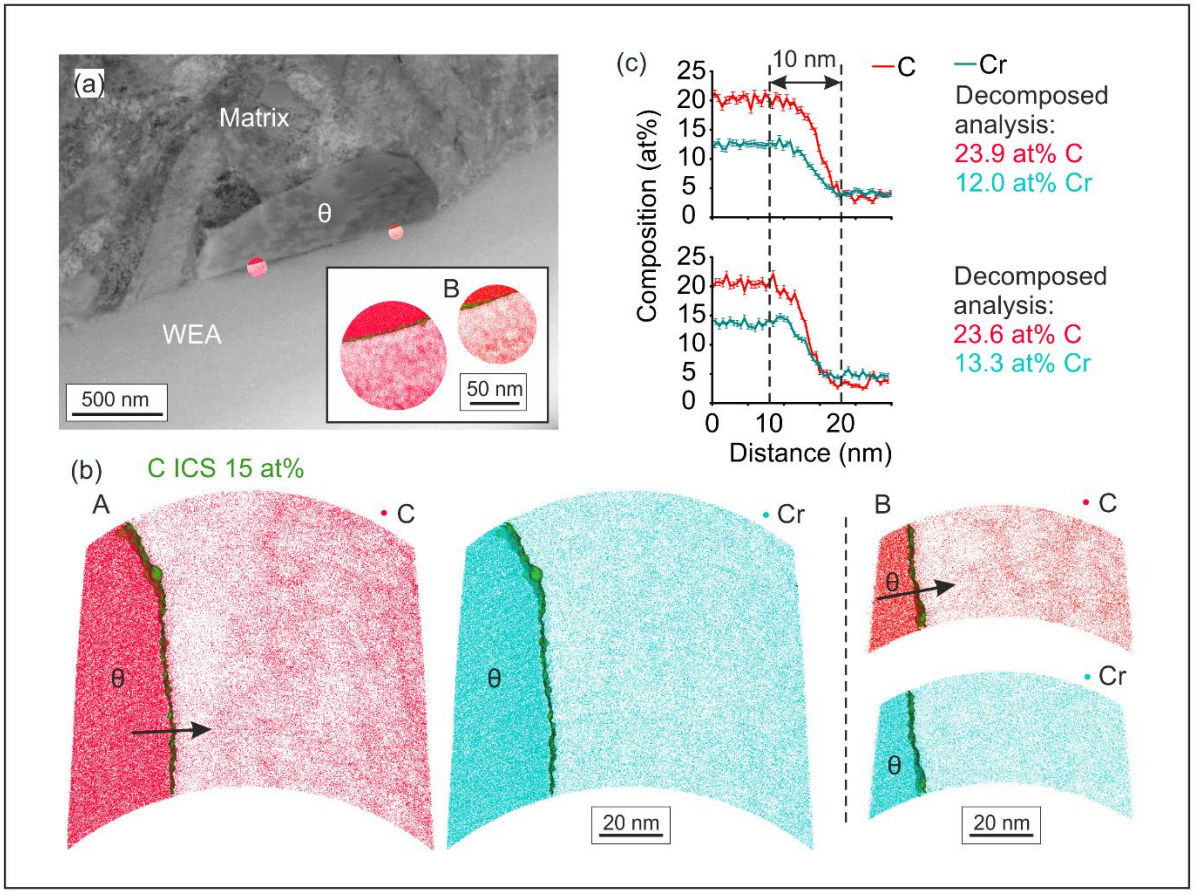

Figure 6.6: APT analysis of a WEA-$(Fe,Cr)_3C$ interface. (a) BSE image showing a $(Fe,Cr)_3C$ precipitate directly adjacent to a fine-grained WEA (< 20 nm), the inset shows 20nm slices from 3D carbon maps of the APT specimen obtained from this interface; (b) shows 8 nm slices of 3D carbon and chromium maps with viewing direction parallel to the interface; (c) presents 1D compositional profiles across the WEA-$(Fe,Cr)_3C$ interface.

Figure 6.6 (a) depicts a BSE image of a $(Fe,Cr)_3C$ precipitate, which is partially decomposed. The interface between precipitate and WEA appears sharp and is parallel to the WEC, which is located at a distance of ~ 1.7 µm on the opposite of the WEA (not shown in the depiction). Site-specific FIB lift-outs for APT analysis target the interface between WEA and precipitate. The inset depicts 20 nm slices of the 3D carbon maps from the obtained APT data sets in the direction parallel to the interface and normal to the image plane. Figure 6.6 (b) shows 3D carbon and chromium atom maps of 8 nm slices of these two APT reconstructions in a view parallel to the WEA cementite interface and perpendicular to the image plane in (a). In (c) 1D composition profiles across the interfaces in both APT reconstructions show that the transition from the intact chromium-rich $(Fe,Cr)_3C$ precipitate to the fully decomposed ferritic WEA happens within only about 10 nm. Since the compositional variation across the interface is affected by the local magnification effect in APT [173], the real transition zone is expected to be even smaller. APT analysis of an unaffected $(Fe,Cr)_3C$ precipitate in upper bainite showed a transition

zone of around 5 nm based on the 1D chromium profile presented in [170]. This implies that the decomposition of $(Fe,Cr)_3C$ precipitates into nanocrystalline ferrite takes place in a highly confined manner, leaving behind only a fraction of the carbon initially present (in Figure 6.6: decrease from 25 at% to ~ 6 at% C).

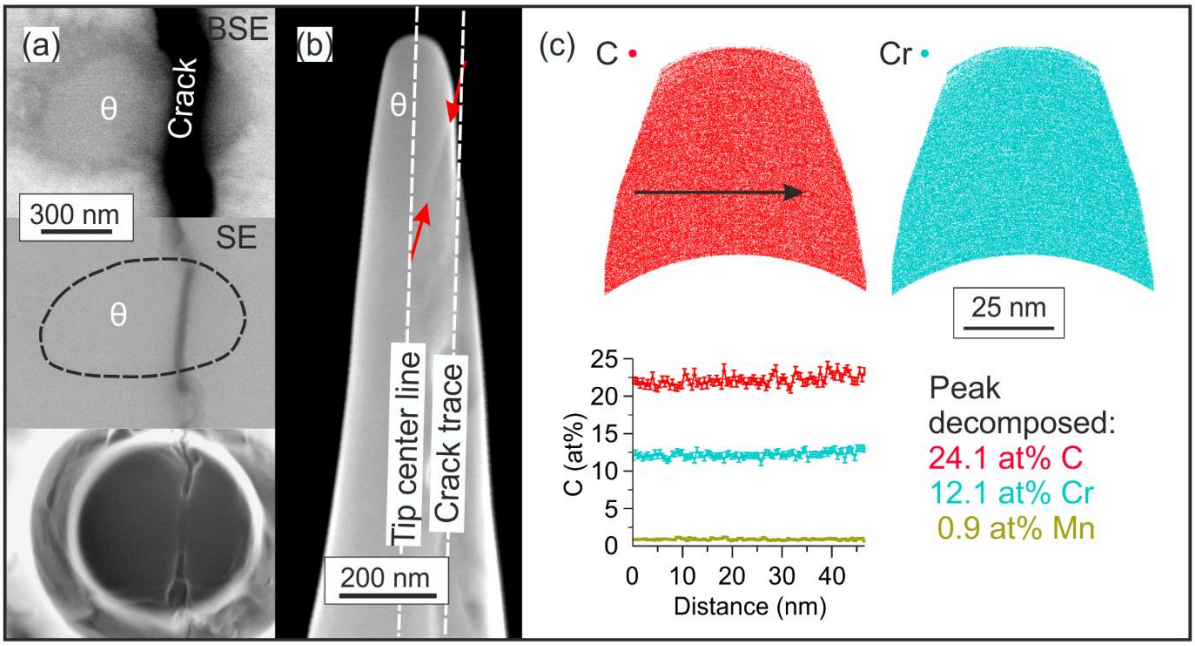

Figure 6.7: Cracked $(Fe,Cr)_3C$ precipitate near a WEC: (a) BSE and SE image of a cracked $(Fe,Cr)_3C$ precipitate; SE image at the bottom shows the same region during FIB milling. (b) SE image of the needle-shaped specimen for APT analysis. (d) APT reconstruction: 10 nm slices of carbon and chromium 3D maps as well as composition profiles showing the homogenous distribution of both elements.

Figure 6.7 (a) shows a BSE and two SE images of another cracked $(Fe,Cr)_3C$ precipitate. The upper two images show the precipitate before the sample preparation for APT analysis. The crack appears smoother inside the precipitate than in the matrix, which might be related to the high hardness and accompanying low ductility of cementite. The image at the bottom shows the crack position in the lifted out sample after the first milling steps during FIB preparation. Figure 6.7 (b) shows the tip at 52° tilt angle after the final milling step. Red arrows mark the position of the interface between $(Fe,Cr)_3C$ adjacent ferrite (WEA or more likely bainitic ferrite). The dashed lines show the crack's trace and the center of the tip specimen. Extrapolation of the crack trace is used to estimate that the distance between WEA at the apex and crack is < 100 nm. Figure 6.7 (c) shows 3D carbon and chromium atom maps from a 10 nm slice of the APT reconstruction; both exhibit homogenous distribution of the elements within the volume. This is confirmed by the composition profile. The composition is close to the ones reported in the previous section for both carbon and chromium. A slight underestimation of carbon

(stoichiometric 25 at% in cementite) is observed as in the previously presented $(Fe,Cr)_3C$ precipitate. These results agree very well with the work of Takahashi et al. [166], who performed measurements on undeformed cementite under virtually the same APT measurement conditions and also obtained a slight underestimation of carbon content. This measurement shows that the precipitate is compositionally intact and hence virtually unaffected by the stress raising capacity of the adjacent WEC.

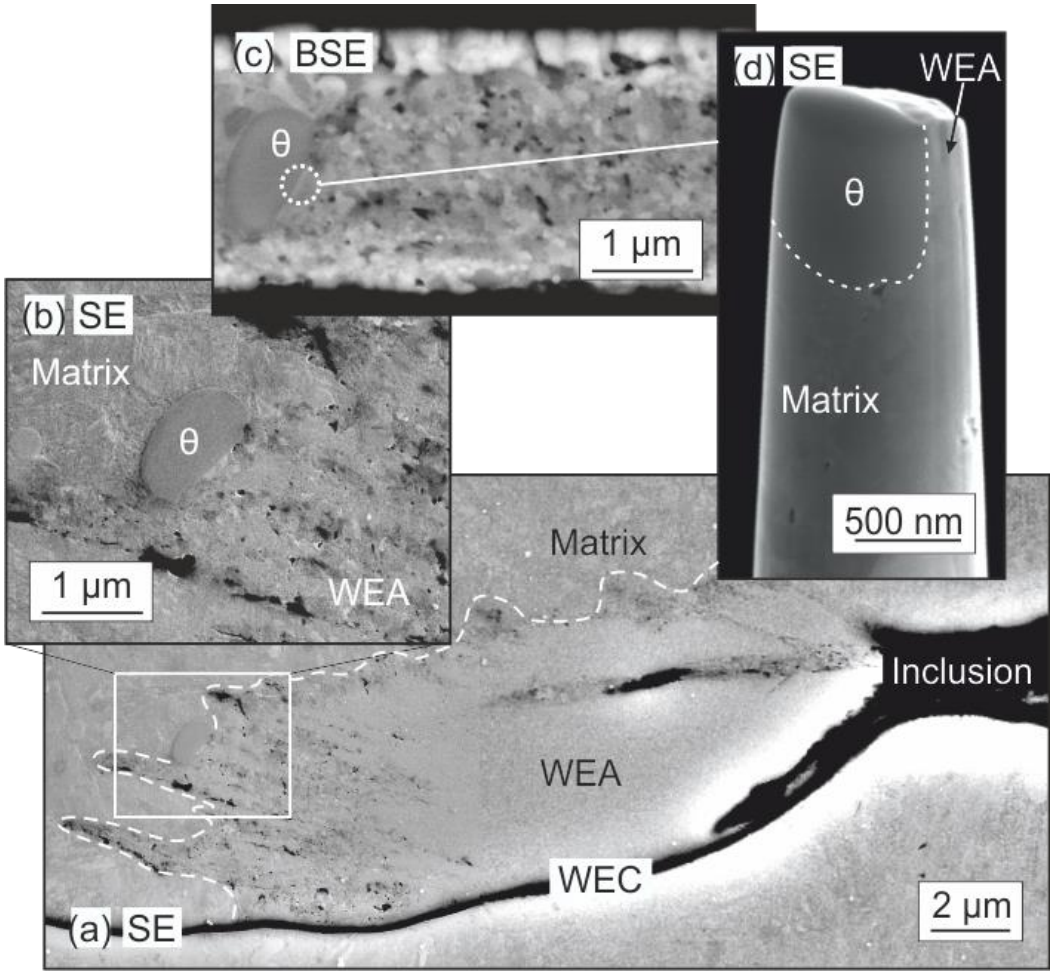

Figure 6.8: $(Fe,Cr)_3C$ precipitate at the serrated interface of WEA and matrix in a butterfly wing. (a) BSE image of WEA of a butterfly wing. (b) SE image of the ROI marked in (a). (c) BSE image of the lift-out in preparation for APT analysis. (d) SE image of the needle-shaped specimen with the $(Fe,Cr)_3C$ precipitate being located at the top.

Figure 6.8 (a) shows a butterfly wing emanating from a non-metallic inclusion. The WEA exhibits a heterogeneous grain size distribution. The butterfly is connected to a larger WEC network spanning across a region of about 400 x 450 μm^2 in the observed cross-section (not shown). The serrated interface outlined by dashed lines is typical for WEA matrix transition on the opposite side of butterfly cracks and is frequently seen at WEC tips, as, e.g., presented in Figure 6.3. Figure 6.8 (b) shows a magnified view depicting a $(Fe,Cr)_3C$ precipitate at the interface of WEA and matrix. The WEA contains a

significant amount of what could be identified as voids, but more likely are and carbon deposits, as was shown in section 4.2.3. This assumption corresponds well with the observed grain size in this particularly coarse WEA region, which is comparably coarse, covering a range to a few hundred nm, as can be seen in the BSE image in Figure 6.8 (c). For grain growth to occur, decarburization has to take place, as otherwise grain boundaries are stabilized by carbon Chapter 5. Figure 6.8 (d) is a SE image taken during FIB tip specimen preparation for APT analysis. The respective lift-out position is indicated by a circle in Figure 6.8 (c). At this step of preparation, the interface between $(Fe,Cr)_3C$ and WEA runs roughly along the tip center.

Figure 6.9 presents results of the analysis of an APT specimen that stems from the interface of WEA and matrix shown in Figure 6.8. In Figure 6.9 (a), two 3D carbon atom maps are shown with 12 and 5 at% carbon iso-composition surfaces (ICS). They show the carbon-rich precipitate (25 at% C) on the left-hand side and ferrite on the right locally containing only ~ 0.6 at% carbon in the outlined region. There are, however, several regions with higher carbon composition, as highlighted by arrows. They are partially aligned with positions where the ICSs are bulging out. Figure 6.9 (b) shows an enlarged view of a 5 x 10 x 4 nm^3 volume in which all detected iron atoms are displayed. {110} planes are visible in the z' direction as it is also shown in the spatial distribution map (SDM) below. The [110] direction is tilted ~ 15° off the length axis of the reconstructed volume. Figure 6.9 (c) is a stack of iron density maps that were extracted at 50 nm spacing. They all show a typical ferrite [110] pole, which shows that the entire ferrite region belongs to a single ferrite grain. The orientation of the planar carbon enriched features (that appear linear in this projected view) are well aligned with the {110} planes, which are the preferred glide planes in ferrite [187]**.** During cyclic loading, dislocations could therefore aid decomposition. As they pile up at a phase boundary, they provide energetically favorable sites and attract carbon atoms [188, 189]. During subsequent gliding, which is caused by cyclic reversed stresses from the rolling elements, they drag carbon atoms away from their initial location [135]. Figure 6.9 (d) comprises a 3D carbon and a 3D chromium atom map from slices of the data set that include carbon, chromium, and silicon ICSs. These views are rotated 30° about the length axis with respect to the depictions in (a) and show the phase boundary edge-on. The chromium ICS is shown in the carbon atom map and vice versa. This shows that chromium-rich $(Fe,Cr)_3C$ precipitate is surrounded by a roughly 10 nm thick shell of Fe_3C, which formed during the final tempering step of the heat treatment. This is also visible in the 1D composition profile in Figure 6.9 (e).

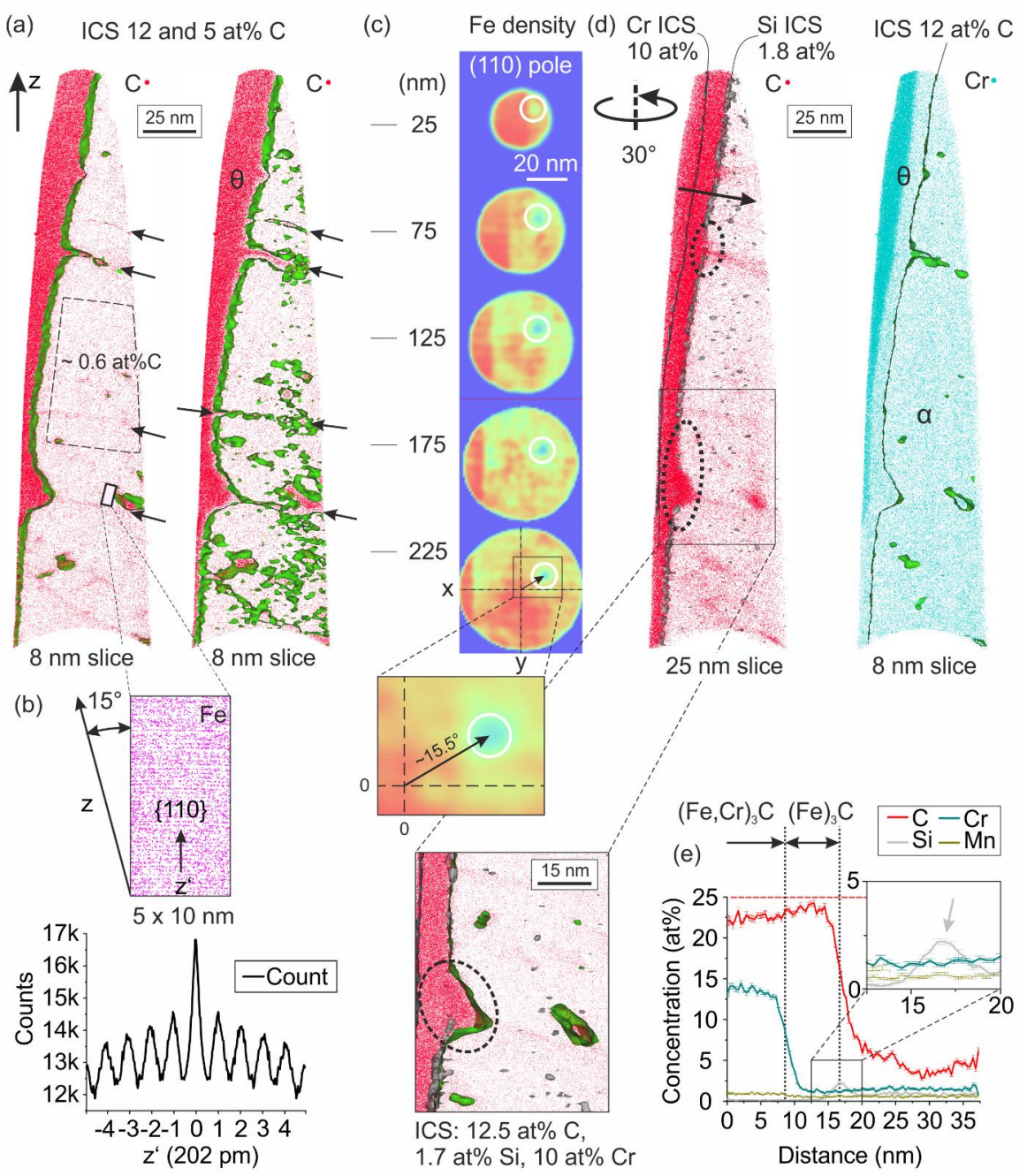

Figure 6.9: APT analysis of $(Fe,Cr)_3C$-$(Fe)_3C$ precipitate at serrated WEA-matrix interface. (a) 3D atom maps of carbon with isocomposition surfaces of 12 and 5 at%, respectively. (b) 5x10x4 nm ROI with all iron atoms displayed. Periodicity is visible and also shown by the spatial distribution map (SDM). (c) Fe density maps of 3 nm slices at positions along the length axis with 25 nm spacing. (d) 3D atom maps of carbon and chromium atoms with silicon, chromium, and carbon ICSs illustrating the chromium-enriched shell of spheroidized precipitates. Magnified view of bulging carbon ICS and 1D compositional profile across the precipitate-WEA interface.

During tempering[16], silicon partitions into the ferrite. Since it is not homogenized in ferrite, a silicon enriched region close to the interface is present. This can be seen in the carbon atom map in Figure 6.9 (d), where the silicon ICSs form a string of small volumes at the ferrite cementite boundary. The same can be observed in the composition profile in (e). However, in the carbon map in (d), it is important to note that at the position of the bulging carbon ICS the string of silicon-rich volumes is interrupted. This is especially clear from the magnified view of the largest bulge in the lower part of the reconstruction in Figure 6.9 (d). Determination of the $(Fe,Cr)_3C$ composition yields very similar results to the precipitates previously shown. The presented results provide evidence that this particular precipitate is mostly intact, while in several planar regions of only a few nm thickness, decomposition had been initiated.

6.2.4. Grain size and orientation differences inside WEA

Figure 6.10 (a) shows a WEA at the interface to a spheroidized $(Fe,Cr)_3C$ precipitate in the matrix microstructure. The interface is outlined by a dashed line. Note that straining effects indicating deformation are visible in the precipitate close to the interface. The WEA is inhomogeneous in terms of grain size and, therefore, carbon content (Chapter 5, sections 0and 5.5.2). While this can be observed in the BF image, it is more clearly revealed in the inset, which shows a centered dark-field (CDF) image that was obtained using a portion of the {110} ferrite ring. The ferrite grains are finest in the middle of the depicted region. The mean grain sizes estimated from energy-filtered CDF images[17] are 6 ± 2 nm and 12 ± 5 nm for the finest grain size and the slightly larger ones on the right-hand side of the depicted region, respectively. Figure 6.10 (b) is a SAD pattern from the region indicated by the circle in (a). Based on an estimated lamella thickness of 50 nm and a grain size of 6 nm, it contains information from around $5 \cdot 10^4$ individual grains[18]. Intensity variations along the {110} ring are not clearly visible in the SAD pattern. However, in the {200}, ring they are easily recognizable. Maxima are indicated by green arrows, minima by red arrows. In Figure 6.10 (c), the normalized intensities[19] along the azimuth are plotted and confirm the qualitative observation. While the {110} ring profile shows a ratio of maximum to minimum intensity of around 2, for the {200}-profile, the ratio is around 5.

[16] The tempering temperature of the analyzed component bearing is unknown. The lower bainite condition indicates that it is below ~ 300 °C.
[17] These estimations are based on averaging of measured long axes of identifiable grains in 440 x 440 nm large areas.
[18] The grains are assumed to have a cubic shape for this rough estimation.
[19] Linear background subtraction was performed.

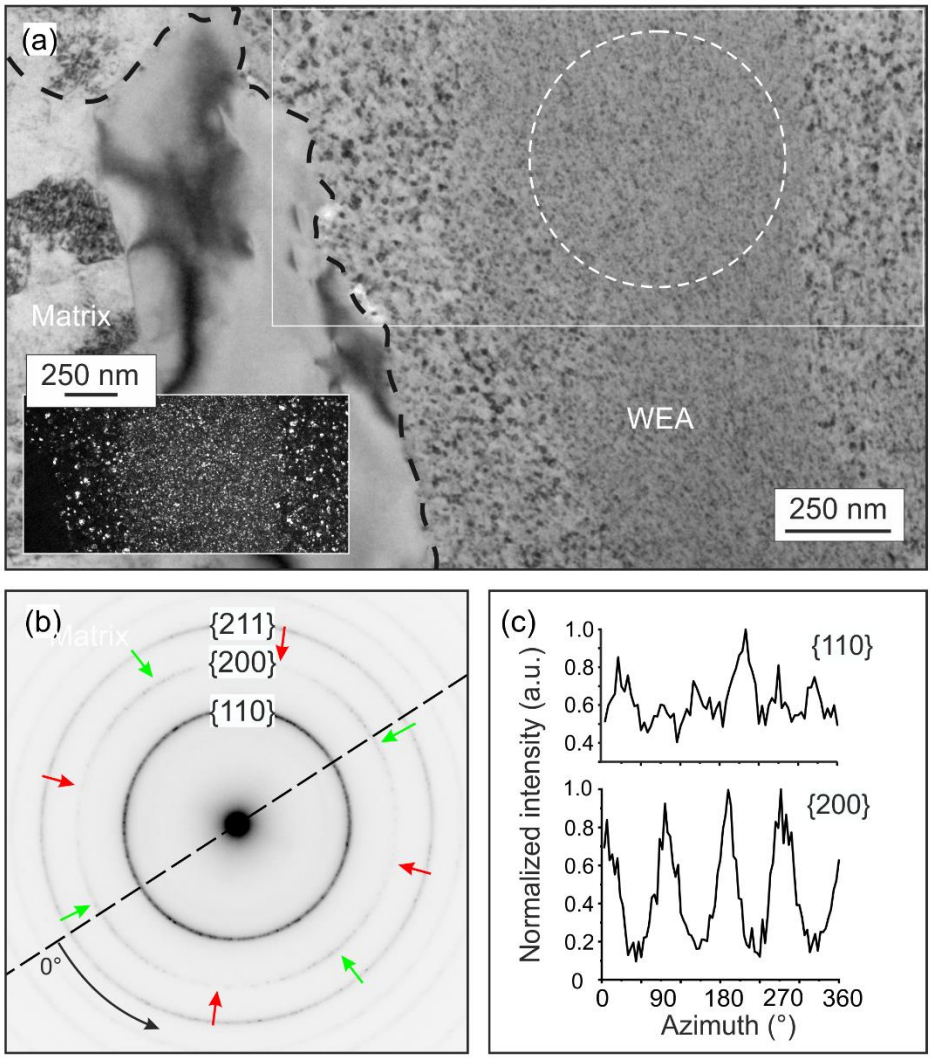

Figure 6.10: Inhomogeneity in WEAs in terms of grain size and grain orientation. (a) BF TEM image of WEA with different grain sizes. The inset shows the corresponding DF image. (b) SAD pattern from the circular area in (a), goniometer axis is indicated by the dashed line. (c) Intensity profiles along the {110} and {200} ring in (b).

6.3. Discussion

6.3.1. Chronology of WEC and WEA formation

This section discusses the question, whether WECs precede WEA formation or vice versa. Both standpoints have proponents in the literature, as was described in section 3.3. The results presented in the results section 6.2 are construed as support for the understanding that WECs form first and are hence a precondition for WEA formation.

In section 6.2.1, it was demonstrated that WEAs virtually always form on both sides of WECs. In Figure 6.1 (c), a precipitate in close vicinity to the crack tip (~ 1 µm) was shown that already exhibits signs of

decomposition and WEA formation. Further, narrow WEAs can also be observed in Figure 6.4 and Figure 6.5 inside cracked cementite precipitates. Still, it remains almost impossible to undoubtedly prove that WECs are always bordered by WEA[20]. However, at this point, there is no obvious reason to reject the claim that WECs are always bordered by WEA. In addition to the invoked cases, all other cracks that were observed in the present and previous work for this project [102, 113, 190] are bordered by WEA on both sides at high magnifications in the TEM even if they appeared to only exhibit WEA on one side at moderate magnifications in SEM images. This is also supported by results from other published investigations: for example, West et al. [191] used ion channeling contrast for imaging of WECs, and in their publication, WECs with strongly asymmetrical WEA distribution nevertheless exhibit WEA on both sides of the presented cracks. This is also the case for investigations of butterflies with sufficient resolution [27, 45]. As reasoned above, this is treated as a further indication that the presence of WEA on both sides of a crack is a general feature of WECs. Additional support for this hypothesis can be drawn from the following observations: horizontal cracks, which are the first to initiate and propagate [72, 81, 106, 192, 193], in general exhibit stronger WEA decoration. The amount of WEA bordering a crack is furthermore usually less pronounced towards the tip; the same is the case for vertically branched cracks, which emanate from the initial horizontally aligned cracks [72]. Continuing in this line of thought entails that WEAs are caused by the crack, which leads to larger WEA volumes around early formed cracks or crack segments.

There is additionally no obvious reason why a crack that would hypothetically appear *after* WEA formation should propagate inside a WEA and not along the WEA-matrix interfaces, which is the weakest point due to the strong discrepancy in material properties. If WEAs formed first, a crack should be found with WEA on one and matrix on the other side. On the contrary, not a single case has been observed where a WEC was in direct contact with the matrix, nor was such a clear case presented in the relevant literature to the best of the author's knowledge.

The high accumulated strains experienced by the material (which after all leads to the full decomposition of cementite) make it unlikely that the crystallographic orientation of the initial material is preserved. Instead, a preferred orientation is a result of the deformation process. The SAD ring pattern in Figure 6.10 shows that a deviation from random grain orientation is present, which is stronger in the {200} than in the {110} ring. Similar intensity distributions with six maxima in the {110} and four in

[20] One can visualize this by means of looking at how to prove a needle in a haystack. While its existence is comparatively easy to prove, its absence requires the investigation of every single blade of grass. Similarly, a whole WEC would need to be investigated with sufficient resolution that can only be provided by TEM investigation, which, however, can only be performed on thin foils and therefore cannot capture an entire WEC network.

the {200} were observed in further WEAs that have been investigated for the present work as well as in the literature [64, 116, 118, 191, 194]. Since TEM lamella planes are usually roughly perpendicular to the cracks and therefore to the assumed shear planes, the observation of similar orientation distribution in many cases might well be connected to the shear deformation. This, however, could not be confirmed due to the limited accessibility of orientations by TEM measurements in the nanocrystalline grain size regime. While SAD ring patterns provide statistically significant information, they can only be recorded over a limited tilt range, which results in incomplete pole figures. TEM based orientation mapping suffers from the limitation that a statistically significant number of grains cannot be measured as only very small regions can be thinned sufficiently to avoid grain (and therefore pattern) overlap. However, the fact that SAD patterns from WEAs stemming from multiple investigations exhibit the mentioned similarities points to a similar evolution of their structure. Taking into account that the crack orientations with respect to the loading direction differ in the reported cases (i.e., lift-outs stem from cracks with different angles to the surface tangent and hence the loading direction), it is argued that this is a further indicator for the view that WECs precede and cause WEAs.

The hypothesis that WEAs form early after a crack has propagated is additionally supported by results from uniaxial fatigue tests on 100Cr6. There it has been unequivocally accepted that cracks in the very high cycle fatigue regime initiate at subsurface non-metallic inclusions [59, 195, 196]. This means that microstructural alterations around cracks, which are emanating from non-metallic inclusions, are caused by these cracks. In these investigations, so-called fine granular areas (FGAs), which are very similar to WEAs, were observed in tests where crack closure leads to contact of crack surfaces [95, 97]. In addition, similar results were obtained from experiments emulating RCF conditions by superimposing shear loads during compressive portions of the applied loading cycles [99].

6.3.2. Proposed model of WEA formation and evolution

Recently, Morsdorf et al. [102] proposed a WEA formation mechanism that is associated with moving cracks. The key idea is that cracks do not merely propagate but additionally change their position in the lateral direction perpendicular to the crack plane. This is thought to take place by partial rewelding of the crack, which enables nanoscale material transfer across the crack surfaces and results in the mentioned lateral displacement. In Chapter 4 and Chapter 5, it was shown that WEAs are mostly depleted in carbon as compared to the average carbon content of the alloy. Due to the subsurface nature of WECs, it was concluded that no net loss of carbon the bearing component. This was supported by findings of pure carbon deposits, which are likely a result of crack surface interaction and lead to the observed local decarburization. The rewelding of crack surfaces and the local carbon contents are

thought to play a role in the formation and evolution of WEAs, as will be described in detail in the following sections.

Results presented in section 6.2.3 show that plastic deformation is taking place at the interface of WEA and matrix. As can be seen in Figure 6.4 (b) and (c), a small plastic zone (~ 100-150 nm) is present at the interface between WEA and bainitic ferrite. More confined and visible due to individual dislocations, plastic deformation also takes place at cementite WEA interfaces (see Figure 6.5). This very confined transition in such specific cases can also be inferred from the partially decomposed cementite precipitate in Figure 6.1 (a), where a slight variation in contrast at the interface to the WEA reveals strain inside the precipitate. The confined nature is additionally evident from the APT measurements in Figure 6.6. The smaller decomposition zone in cementite precipitates as compared to bainitic ferrite is due to the higher hardness of the former (~ 15 GPa $(Fe,Cr)_3C$ vs. ~ 10 GPa martensitic/bainitic ferrite [197]). The presented results show that the observed plasticity must be caused by highly localized stresses, which govern the decomposition process. These cannot be initiated only by external loads exerted on the raceway surface through the rolling elements. The only conceivable way is that localized plasticity is caused by stress raising effects through the interaction of crack surfaces. In the following, the mentioned work by Morsdorf et al. [102] describing the process of crack surface rubbing will be amended, complemented, and refined.

Interaction of crack surfaces and plasticity at WEA-matrix interface

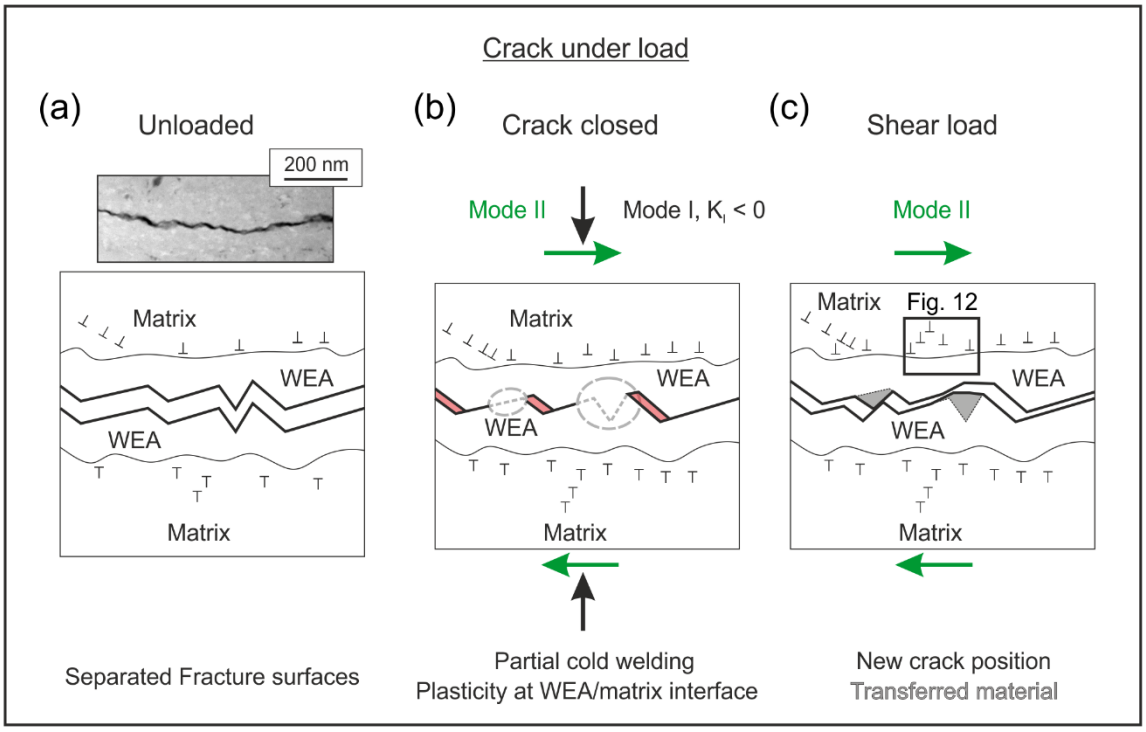

Figure 6.11: Schematic of the mechanism describing partial crack welding and reopening, and decomposition of matrix microstructure and WEA formation by plasticity at the WEA-matrix interface. (a) Unloaded WEC, (b) partially fused WEC under combined shear and compressive load, (c) WEC under shear load.

Figure 6.11 (a) depicts a schematic of an unloaded crack, which is slightly open. The actual dimensions of crack opening cannot be elucidated conclusively, as all observations are made on free-cut sections that allow for changes in stress and, therefore, also strain state as compared to the condition enclosed inside and intact bearing component. The removal of the surrounding material can result in an increased gap between the crack surfaces, as was, e.g., observed during the preparation of the TEM lamella shown in Figure 6.4. There, the embedding resin is approximately 50 nm thick. This likely marks the gap width before the lift out of the lamella, which might have been even smaller inside the intact component. The opening of a crack can be small, as visible in the HAADF image shown atop the schematic in Figure 6.11 (a), which shows a gap of only ~ 10-20 nm.

When a rolling element approaches a cracks' position, a combined compressive and shear load is exerted on the sub-surface material volume (see section 3.1), as indicated by black and green arrows in Figure 6.11 (b). The schematic indicates that upon close contact at some positions, crack surfaces partly reweld. These pure metal on metal contacts make it effectively indistinguishable from bulk material [198], which means that at such positions opposing crack surfaces are fused by cold-welding. This can

happen easily in WECs that are not connected to the surface [69-71], and hence oxidation cannot take place. However, even if thin oxide films were present, they should be easily removed and hence not act as a strong obstacle for rewelding when continued reciprocating sliding occurs [199]. In Chapter 4 is was reasoned that carbon could be present at crack surfaces. It is, therefore, necessary to address a potential objection, which could be raised in light of the presence of carbon covering the crack surfaces, namely, if this should not inhibit the formation of bonds between the crack surfaces. This, however, need not be the case since – as was just mentioned – oxides also do not fully inhibit its occurrence and, since cracks are not flat but exhibit topology, displacement leads to inhomogeneous contacts at and caused by asperities. In consequence, it is reasoned that comparatively soft carbon matter can likely be displaced and, therefore, partially agglomerate in free volumes formed by the sliding crack surfaces [150]. The formation of such free volumes is illustrated in Figure 6.11 (b) as shaded areas (light red). If these free volumes are facilitating agglomeration of carbon, which are incorporated into the WEA during continued deformation and, e.g., folding of asperities [200], this would be a potential explanation of the formation of carbon deposits that were reported in Chapter 4. As the compressive load is reduced, and the maximum shear amplitude is reached, the crack partially opens again due to wedging (Figure 6.11 (c)). In this scenario, the unfused crack segments act as initiation sites for the crack to reopen and as this takes place, the change in a crack's position results in a lateral displacement. This can be interpreted in analogy to a net material transfer from one side of the crack to the other, as illustrated by the shaded areas in Figure 6.11(c) (grey areas). Taking into account the results from Figure 6.4 (b)-(d), which have shown increased misorientation in the bainitic ferrite bordering the WEA, it is assumed that in addition to deformation taking place at the crack surfaces, the shear stresses acting at the crack surfaces are transferred through the WEA and cause plastic deformation at the WEA-matrix interface. This is illustrated by the increase in dislocation density at these interfaces from Figure 6.11 (a) to (b). Nanocrystalline WEAs[21] are harder than the bainitic ferrite [64]. As a result, plastic deformation is induced at such interfaces. This process occurs in a cyclic manner during RCF loading. Therefore, the bainitic microstructure is continuously undergoing deformation and is finally being decomposed, and WEA is created. The result is the extension of WEA normal to the crack plane.

Plasticity inside WEAs

Plastic deformation inside WEAs and the adjacent matrix is complex and likely involves different processes, as is inferred from the different WEA morphologies. On the one hand, very fine WEAs with grain sizes in the order of ~ 5-20 nm are frequently observed (Figure 5.1, Figure 5.4, Figure 6.10 and

[21] WEAs that have undergone strong decarburization lose a significant portion of their initial strength and hence plasticity is assumed to take place through the creation and glide of dislocations.

[26, 27, 30]). On the other hand, results in Figure 6.4 (b), (c), and in Figure 6.4 (e) exhibit dislocation activity in bainitic ferrite and inside the WEA, respectively. As deformation increases and LAGBs form, accommodating the misorientation between subgrains such a process can lead to the formation of HAGB [201], and hence new grains of smaller size can emerge. When such processes repeat, and the average grain sizes decrease, the hardness of the material increases as described by the Hall-Petch relationship [202]. The creation and movement of dislocations are increasingly limited due to the large numbers of GBs. This can lead to grain sizes, which do not allow for dislocation mediated plasticity, causing the break down of the description based on the Hall-Petch relationship [203]. Instead, plasticity is carried by grain boundary sliding (GBS) [204] and potentially leads to moderate softening with further decreasing grain size in nanocrystalline metals [205]. Most investigations of this effect have been conducted on pure fcc metals (e.g., Cu [203] [206]), and generalized theoretical descriptions have been presented for fcc and hcp metals (e.g. [207]). According to Argibay et al., the transition grain size for a deviation from Hall-Petch type behavior is estimated to be around 10-20 nm in pure fcc metals [199]. Investigation of alloyed fcc systems show that GB stabilization in some cases inhibits softening (e.g., Ni-Mo [208] or Ni-W [209]) and shifts the transition to smaller grain sizes (e.g., from ~ 12 nm in pure Ni [210] to ~ 8 nm Ni-P [211]). That being said, bcc metals should behave similar to fcc metals, and recent investigations by Chandross and Argibay [212] and Hinkle et al. [198] indicate that for pure tantalum, the transition from the Hall-Petch regime to GBS lies in the order of 30-40 nm (2-3 times that of fcc). This is in agreement with the strong decrease in dislocation density that was found in molybdenum in a TEM study by Cheng et al. [175] (from ~75 nm to ~35 nm grain size, an ~80 % reduction in dislocation density was reported). Alloying shifts the transition grain size to smaller values, e.g., for bcc $Fe_{85}Al_4Si_{11}$ ~ 13 nm is reported by Shen et al. [213]. In light of the cited investigations, it seems plausible to assume that WEAs, which exhibit small grain sizes as the ones shown in Figure 6.10 (~ 6-12 nm), are potentially affected by such a transition regarding deformation mechanisms, even if GBs are stabilized by carbon segregation.

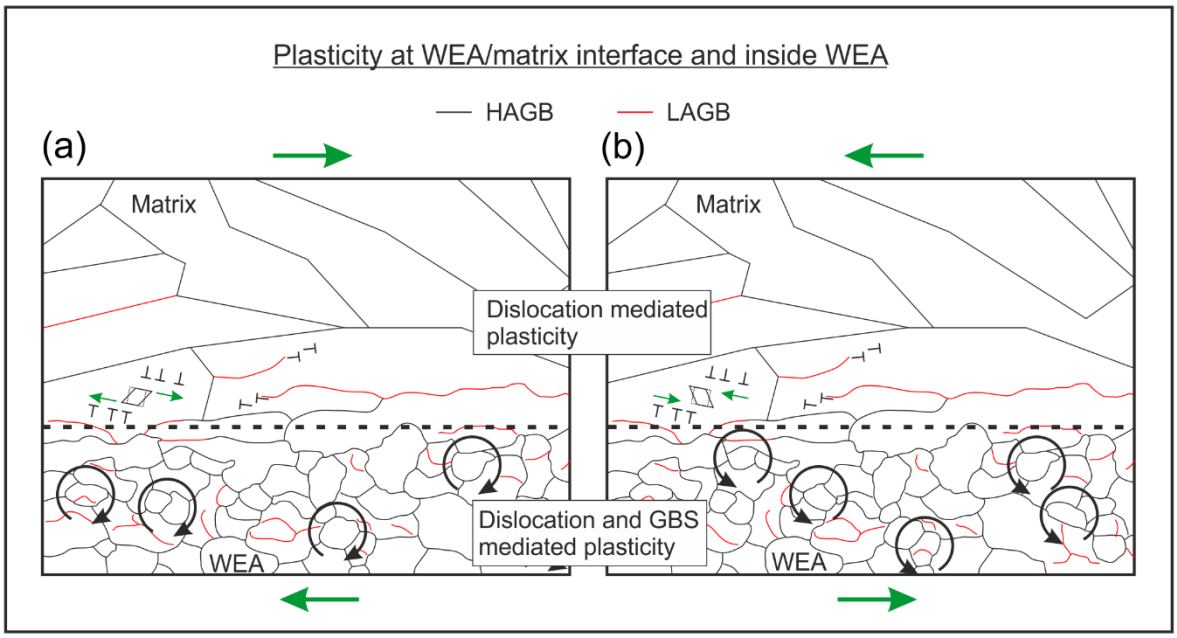

Figure 6.12: Schematic of plasticity inside WEAs and at the interface to the matrix microstructure: (a) and (b) depict the interface (dashed line) of WEA and matrix with a shear stress reversal from (a) to (b). Plastic deformation in the matrix close to the interface occurs via dislocation motion, while in the WEA, the grain size can become too small for dislocation-mediated plasticity and grain rotation by grain boundary sliding (GBS) occurs.

The results presented in Figure 6.4 (b)-(e) and Figure 6.10 point to the complexity in which plasticity takes place inside WEAs. Different mechanisms are active, which are additionally interacting with each other. A proposed mechanism of plasticity inside WEAs and at the interface of WEA and matrix is presented in Figure 6.12. There, (a) and (b) schematically depict an interface of the bainitic (or martensitic) matrix at the top and WEA below. HAGBs are outlined by black and LAGBs by red lines. Arrows at the top and bottom indicate the direction of shear, which is reversed between (a) and (b). Plastic deformation in the matrix occurs by the creation and movement of dislocations as outlined and discussed in section 0. Inside the WEA, plastic deformation is assumed to take place by a combination of GBS allowing grain rotation of small grains (< ~ 15 nm) [214] and continued dislocation creation and subsequent formation of subgrains/LAGBs within larger grains (> ~ 20 nm). During continued cyclic loading, these can evolve into HABG as well, leading to subdivision and hence an increased number of smaller grains. Once the size of these grains falls below the threshold for dislocation-mediated plasticity, deformation is carried by grain rotation and GBS.

Albeit the limitations of grain growth due to a combination of stabilization of GBs by carbon segregation (Chapter 5) as well as kinetic limitations due to comparatively low temperatures of 60-90 °C, some amount of recrystallization and grain growth occurs in WEAs**.** In addition, subgrain

formation as observed in Figure 6.4 (e) can be seen as evidence for recovery [215], as can the low amount of dislocations in grains of ~50-80 nm size (see APT tip 2 in Figure 5.1). While the formation of new grains will likely take place continuously, significant grain growth can only occur when carbon is expelled from regions of WEA and GB mobility is enhanced. The resulting grain size is then determined by the amount of carbon, which locally differs in a significant manner. As large grains (several 100 nm) are significantly easier to deform than fine-grained WEAs or the matrix, they experience continued plastic deformation leading to renewed grain refinement until the driving force, due to the energy stored in defects, is sufficient to initiate a new cycle of recovery and recrystallization. This cycle is thought to be repeated multiple times, depending on the alternating crack surface interaction that is governed by the external loads. Based on this understanding, it is possible that WEAs continually deform by different modes. If a WEA is layered like, e.g., seen in Figure 6.10, it might be possible that such layers – exhibiting different strengths – experience differing amounts of strain with the material being displaced within such layers parallel to the crack plane. That this type of transport is present is supported by the observed chromium redistribution parallel to WECs over several µm (Figure 6.5 and [102]). Such a partitioning of intra-WEA deformation also leads to dissipation of a portion of the shear transferred by the WEA to the interface with the matrix and potentially reduces the extension of WEAs.

Cementite decomposition

The process of cementite decomposition, as observed in this chapter, is discussed on the basis of the relevant literature. Comparisons to mechanisms of cementite decomposition (often also referred to as ‘dissolution’ since carbon is brought into solution in the surrounding ferrite), as discussed there, have to be evaluated based on the respective deformation conditions. In the case of WEA, these are significantly different compared to the deformation of pearlitic steel in, e.g., wire drawing or high pressure torsion (HPT). WEAs are formed by accumulated cyclic strains (with no macro-scale change in the shape of the deformed volumes) HPT and wire drawing are usually monotonic processes. In addition, significant shape changes are taking place in the case of wire drawing, where large elongation goes along with significant reductions in diameter, and at least some shape change takes place in HPT. For 100Cr6 in the hardened condition, this, for example, amounts to a thickness reduction of 20% [216] due to the high applied pressure, which is necessary for hardened steels to prevent slipping between anvil and disc sample while achieving significant shear strains. Decomposition of cementite in lamellar pearlite has been extensively investigated in the literature, e.g. [135, 163, 217-221]. One explanation of cementite decomposition during deformation of pearlitic wires by Sauvage et al. [221] is based on the Gibbs-Thomson effect, namely that the increase of total interfacial area, which causes a higher

solubility of carbon in ferrite, destabilizes cementite and causes carbon loss. This scenario differs significantly from the present case where no large increase in the interfacial area occurs[22] and can therefore be rejected as an explanation for the presented cases.

A decomposition mechanism based on the interaction of carbon atoms with dislocations described by Gridnev and Gavriljuk in their review [135] is closer to the present WEA scenario. According to their description, it is energetically favorable for carbon to be located at dislocations rather than in cementite. Carbon atoms sitting at dislocations in ferrite have an energy of ~ -0.75 eV [222]/ -0.84 eV [223] lower than carbon in strain-free Fe_3C (the energy barrier to escape Fe_3C is 0.4 eV [189]). If the dislocation density is high near the interface of cementite and ferrite, this can lead to a net carbon transport into the ferritic WEA. Additionally, inside fine-grained WEAs near decomposing $(Fe,Cr)_3C$ precipitates (see for example Figure 6.5 and Figure 6.10), large GB areas are present that can locally accommodate high amounts of carbon (up to ~ 9.5 at% C, see Chapter 4). If dislocation-based plasticity is dominant, moving dislocations will drag along carbon atoms as described by Ivanisenko et al. [218] for HPT experiments on lamellar pearlite where a ferrite grain size of 10 nm is reported. Li et al. [219] showed evidence of Cottrell atmospheres around dislocations in ferrite of cold-drawn pearlitic wires by APT, demonstrating strong evidence for this proposed dislocation drag mechanism. Nematollahi et al. [189] specified this mechanism based on theoretical assessments. By means of different scale bridging calculation methods, they showed that at low temperatures, which also apply to the case of WEA formation, the transport of carbon takes place along with moving dislocations as opposed to pipe diffusion, which is only relevant at higher temperatures. Accordingly, GB diffusion may also not present a significant factor for carbon redistribution. With an increase in dislocation density and hardness of the ferrite, a wear-like process inside a confined region is feasible [218]. This agrees well with a recent study by Qin et al. [216], which is best suited to be compared to cementite decomposition associated with WECs because the same steel grade in similar condition (martensitically hardened 100Cr6) was used. There, decomposition of spheroidized cementite in martensitic 100Cr6 during HPT was investigated with the conclusion that an interfacial wear process takes place. The martensitic matrix flows around the precipitates and transports carbon as well as chromium into the matrix. This was observed to be supported by (size-dependent) plasticity inside the cementite, creating slip steps that

[22] The obvious deviation of the WEA/cementite interface from a planar arrangement is neglected here. However, this simplification seems justified if one considers an example of a pearlitic wire with an initial diameter of 0.54 mm that is drawn to a strain of $\varepsilon = 2$, which causes a roughly seven-fold increase in interphase area (calculated using equations from [222]). Additionally, fragmentation is observed for higher strains ($\varepsilon > 3$-4), which further increases the interfacial area. No similar process that leads to a larger interfacial area is taking place in the cementite to WEA transformation process, as can be seen, for example, in Figure 6.1, Figure 6.5, and Figure 6.6.

enhance interfacial wear. It is important to note that - neither in this case nor in the case of WEA formation - chromium transport is controlled by diffusion but takes place by material flow and mechanical mixing. This was demonstrated in the case of a cracked $(Fe,Cr)_3C$ partially transformed into WEA by Morsdorf et al. [102]. In turn, this means that shear-induced mixing must take place, leading to redistribution not only of small interstitial elements but also of much larger substitutional elements [224].

There are, however, some further differences between the decomposition processes described here and the ones addressed in the literature. They will be briefly addressed in the following. In light of the results shown in section 6.2.3, it can be stated that in the cases of decomposing $(Fe,Cr)_3C$ precipitates shown in Figure 6.5 and Figure 6.6, where the crack is parallel to the WEA-precipitate interface, a similar decomposition process through the adjacent WEAs takes place. This occurs due to the presence of a large number of defects (large GB area, dislocations, and vacancies) that act as carbon sinks and destabilize the precipitates. Since $(Fe,Cr)_3C$ was shown to be worn by a martensitic matrix in [216], it is reasonable to assume that fine-grained WEAs (hardness up to 15 GPa [64]) might even be more effective in this process than a martensitic or bainitic ferritic matrix in 100Cr6 (~ 10 GPa [197]). Additionally, the decomposition process takes place in a cyclic manner caused by compressive stress and reversing shear stresses during each over rolling. The amplitude of the crack surface displacement can be estimated by the maximum displacement of chromium inside the WEA in a decomposing precipitate to be in the single-digit µm range [102]. Although the deformation does not lead to a visible shape change, very high accumulated strains are achieved. Ivanisenko et al. [218] reported that after HPT of pearlite, full dissolution of cementite lamellae of 40 nm thickness occurred at shear strains of 200-300. Since in lamellar pearlite, the interfacial area is much larger than in the case of a spheroidized $(Fe,Cr)_3C$ precipitate and its dimensions are also larger than the lamellae, it is reasonable to assume that the accumulated shear strain necessary for full decomposition is higher than 300.

Interaction of $(Fe,Cr)_3C$ with the WEA at the serrated interface, which is usually found close to crack tips, is significantly different from the process that takes place at WEA-matrix interfaces, which are approximately parallel to a WEC. This was shown in Figure 6.8 and Figure 6.9. Although butterfly wings are likely formed prior to the development of WEC networks, this $(Fe,Cr)_3C$ precipitate is not strongly attacked, as is proven by the largely intact Fe_3C shell. This is all the more noteworthy as some regions of the adjacent ferrite grain are strongly depleted in carbon, which means that significant accumulated plastic straining has occurred here. Only low carbon contents allow grain coarsening. In this context, it is therefore argued that the comparatively coarse grains constitute an ‘old’ WEA next to the $(Fe,Cr)_3C$ precipitate (Figure 6.9 (b) and (c)). Although the 3D geometry of the crack and the

interface is not known, it is clear that while the WEA has likely undergone a significant change at the serrated interface, no continued effective transformation has occurred. Based on this line of reasoning and the proposed model, it is concluded that the shear displacement driven wear process that leads to crack surface rubbing, which takes place parallel to WECs, is more effective in leading to microstructural alterations than those brought about ahead of a WEC tip.Since the presented process is effective in decomposing $(Fe,Cr)_3C$ precipitates, it is not clear whether more stable carbides or nitrides alone will create a WEC resistant steel. Small grain sizes in the range of 20-30 nm are stabilized by only ~1-2 at% carbon (see Chapter 5). A significant overall reduction in carbon content also inside the matrix is more promising to yield successes. This could be achieved by means of replacing carbon (partially) with nitrogen.

6.4. Conclusions

In this investigation, nanoscale analyses of WEAs and adjacent microstructure, which consists of lower bainite with spheroidized $(Fe,Cr)_3C$ precipitates, are presented. Characterization of crystallographic structure and chemical composition using electron microscopy and APT have provided the following insights:

- WEAs are present on both sides of WECs. The minimum thickness is some 10 nm. This observation is viewed as further evidence of the chronological order in which WECs precede WEAs.
- WEC surfaces have a near-perfect fit. Although WECs appear smooth at moderate magnifications – which they are in comparison to many other fatigue cracks – they show topology in 2D sections at higher magnifications with asperity heights of several 10 nm. This fact hints at crack-rewelding and reopening during subsequent load cycles. If this was not the case, debris would be observed as crack surfaces are becoming smoother during high numbers of cycles as asperity height is strongly reduced. This is evident from the comparison of faceted WEC tips and smooth segments of fully formed WECs.
- Plastic deformation takes place in different manners parallel to a crack and ahead of a crack tip. In the first case, a plastic zone of up to~ 150 nm at the interface between WEA and matrix was shown by increased misorientation in bainitic ferrite. Plastic deformation is also observed at the interface of WEA and $(Fe,Cr)_3C$. Based on the chemical composition around the interface as measured by APT, the decomposition zone is ~ 10 nm wide. Decomposition is less effective ahead of the crack tip as was shown by a nearly intact $(Fe,Cr)_3C$ precipitate, which upon interaction with dislocations only showed minor signs of break down. This is understood as

further support for the “crack first” hypothesis as only crack surface rubbing induced SPD can transform the volumes associated with WECs.

- Transformation into WEA mainly takes place at the interface to the matrix. This occurs through decomposition caused by the relative movement of the crack surfaces, where shear stresses are transferred through the WEA into the matrix. At the same time, cracks partially reweld and upon reopening are displaced, potentially causing a lateral movement of the crack normal to its plane.
- WEAs often exhibit grain sizes in a regime where the break-down of Hall-Petch description is likely, i.e., deformation inside WEAs can occur by combined dislocation mediated and GB dominated plasticity. This leads to continuous plasticity inside WEAs as indicated by the chromium redistribution near decomposing $(Fe,Cr)_3C$ precipitates.

Summary and conclusion

The results presented in this thesis underline the complexity of the WEC phenomenon. It remains the objective to understand the root cause of formation and propagation comprehensively. This is far from being accomplished, and it may be that the underlying mechanisms are not the same in different applications. Here, investigations of WECs, which emerged in a bearing from a real application in a wind turbine gearbox, are presented. This thesis, therefore, provides new insights for the case of 'conventional' (i.e., non-artificial) WECs in a large scale bearing. These insights are mainly regarding the role of carbon and are presented in Chapters 3 and 4.

Chapter 4 presents results of scale-bridging analyses from the µm to the nm scale by combined EPMA and APT characterization, demonstrating carbon deficiency in a WEA extending over several µm. The presence of carbon deposits is revealed within particularly coarse-grained WEAs. Due to their small size, these carbon deposits are virtually invisible in SEM imaging and spectroscopy. In addition, they are most probably preferentially removed or contaminated during conventional metallographic preparation. Therefore, sample preparation by ion milling provides the advantage that deposits are persevered and can be observed by TEM and APT. The results obtained with STEM-EELS and APT indicate that the deposits most likely consist of pure carbon, although their crystallographic structure could not be determined. It is argued that carbon deposits form by continued plastic deformation of WEAs during crack surface rubbing causing significant decarburization, which then allows for grain growth. Due to the finding of pure carbon, it is deemed possible that excess carbon can be present at the crack surfaces. If this is the case, it can have a dramatic effect on crack propagation, which could be enhanced as friction is significantly lowered, and cracks are therefore able to propagate via shear modes with relative ease.

In Chapter 5, WEAs of varying grain size (ranging from < 10 nm to several hundred nm) are characterized by combined SEM and APT. Evidence is provided that WEA grain sizes are inversely proportional to the respective local carbon contents, and carbon is the grain boundary stabilizing and hence grain size determining factor. According to these findings, a quarter of the nominal alloy carbon content of ~ 4 at% is sufficient to stabilize a mean grain size of roughly 30 nm. It is demonstrated that the same effect is not observed for chromium. Detailed analyses of GB segregation and bulk carbon concentration show that both increase with rising total carbon content inside a WEA. Specifically, no saturation value is found, indicating that simplified models of thermodynamic grain size stabilization via GB segregation are non-applicable at high solute contents (> ~ 2 at%). Nevertheless, correlation of carbon contents of around 1-2 at% and their respective grain sizes are in excellent agreement with ball-

milled and annealed Fe-C model alloys. This provides evidence for the significant carbon redistribution, albeit low operating temperatures in bearings and potentially thermodynamically stabilized WEA microstructures in some regions.

Chapter 6 is an attempt to shed light on details of the formation of WEAs through crack surface rubbing. It builds on previous work that the present author has contributed to but aims at amending and specifying a proposed mechanism describing WEA formation through severe plastic deformation. The present work provides insights that stem from nanoscale analyses of interfaces between WEA and the unaltered base material of the bearing. In order to assess the structural changes, TEM based orientation mapping was carried out, taking advantage of the increased resolution compared to EBSD. The obtained results indicate that in the specific case investigated; plastic deformation takes place in a ~100-150 nm wide region inside bainitic ferrite adjacent to a WEA. TEM and APT results obtained from spheroidized $(Fe,Cr)_3C$ precipitates, which have partially been decomposed and transformed into WEA, demonstrate that in these cases, the transformation zone width is smaller than 10 nm.

Outlook

As one might expect, there is no easy solution to make steels widely available, which exhibit reduced propensity or even resistance to premature failures by WECs. Coatings of different varieties are claimed to reduce WEC prevalence, but it is not clear why such measures are beneficial and how so. Resorting to other steels (e.g., X30CrMoN15-1 [23]) is a viable alternative for specific applications and comparatively small bearings. For large bearings, costs are significantly higher, not only due to material cost but also for production. However, when put in the context of the total cost of a nacelle of a wind power plant (e.g., around 3,700,000 USD for a 5 MW onshore turbine nacelle [1]) and also considering the costs of a possible gearbox replacement, this cost increase for some individual components is likely bearable. The challenge lies in the limited availability of X30CrMoN15-1 (only produced by *Energietechnik Essen* and *Voestalpine Böhler Edelstahl*) and also in the change of processes in bearing manufacturing. The integrated production lines and processing steps that have been established for standard bearing steels and need to be modified, which is not embraced with enthusiasm by manufacturers.

Alongside the main work, the results of which are presented in this thesis, RCF tests on commercially available 100Cr6 thrust washers were carried out on a self-built test rig. These tests confirmed the

[23] The high WEC resistance of this high nitrogen steel is attributed to the unique combination of a) strongly enhanced cleanliness (due at least two remelting steps and additionally pressurized electro-slag remelting, which is used for nitrogen alloying) that largely inhibits crack initiation, b) reduced carbon content, c) high chromium content (this leads to the formation particularly of passive layer, that prevents hydrogen ingress).

findings from the literature, namely that WECs are not easily (re)produced in laboratory experiments. During the analysis of the tested washers, it became evident that the size, distribution, and positions of non-metallic inclusions are drastically different from the ones observed in the WEC affected gearbox bearing ring, which was analyzed for the main body of this thesis. Therefore, it is essential to reevaluate many activities within the research community where it is implicitly assumed that nominally identical alloys, can, in actuality, exhibit microstructural differences that lead to starkly differing performances. Taking into account the microstructure, processing, and size of components, it is quite straight forward to explain the starkly differing WEC prevalence. It is a consequence resulting from dissimilar properties caused by differences in size, shape, and distribution of non-metallic inclusions, which are a consequence of the manufacturing process. Rings of large scale bearings are produced by radial-axial hot rolling. During this process, the radial and, depending on the specific dimensions, sometimes the axial ring thickness, is strongly reduced while the diameter increases. During deformation, MnS inclusions, which are ductile at hot forming temperatures, are aligned with the tangential direction and are furthermore flattened in the axial direction (this is not the case for aluminum, magnesium, and calcium oxides and titanium nitrides due to their higher melting points). The radial load exerted on the raceway during bearing operation is aligned with the direction that is associated with the largest projected area of MnS inclusions, which means the conditions are most detrimental to fatigue lifetime [48]. Conversely, small bearings, which are manufactured from round bars, experience higher degrees of deformation, which also means MnS stringers have smaller dimensions and are aligned with the longitudinal axis, much like a string of pearls. Washers especially are then loaded in the direction least critical for crack initiation (in terms of projected area). In order to clarify this effect, tests are currently being carried out in which a commercially available 100Cr6 washer and a washer manufactured from an unused wind turbine gearbox bearing inner ring are run in a single experiment under virtually identical conditions. It is has been found in experiments using a three-roller test rig that gearbox bearing material exhibits higher numbers of butterflies and WECs and fails earlier than commercially available material of small bearings [107].

Unsurprisingly, the number one measure to avoid WECs, at least in the case of wind turbine gearbox bearings, is most likely to make bearing steels cleaner by reducing the size and number of non-metallic inclusions to eliminate crack initiation. It is especially promising to reduce the number of MnS-inclusion, which are the inclusion type of largest dimensions in wind turbine gearbox bearings and also the ones most often found in connection with WECs. Improvement in this regard can be reached by electro-slag remelting (ESR) instead of vacuum arc remelting (VAR), as it was found to reduce the sulfur content and to generally improve rolling contact fatigue properties in thrust bearings [48]. A remedy could alternatively be brought about through incipient changes in primary steelmaking

processes. The reduction of iron ores is still mostly performed in blast furnaces (BF) using coke, which naturally contains sulfur [225], as energy source and reducing agent. Of the total crude steel production of roughly 43,000 t in Germany in 2017 (EU: 100,000 t), 70 % were produced in BFs, followed by blowing with oxygen (OBC) (EU: 60 %). This processing route is responsible for significant CO_2 emissions as coke is used to provide carbon for the reduction of ores. With the necessity to reduce CO_2 emissions (Chapter 1, section 1.2), replacing carbon with hydrogen as reducing agent can potentially eliminate such emissions. However, this is not straight forward due to several restrictions. Additional energy must be added for direct reduction with molecular hydrogen as this is an endothermic reaction [226]. In order to be effective in emission reduction, hydrogen production needs to be emission neutral, i.e., from renewable energy sources, which is currently not attainable [226]. Despite these challenges, direct reduction with hydrogen has the potential to reduce the content of undesirable elements such as sulfur compared to the BF-OBC process. Furthermore, using *only* hydrogen for direct reduction (not industry standard) can reduce the carbon content in crude iron. This would make decarburization and hence deoxidation mostly obsolete, or at least reduce the number of elements used in deoxidation that are a source of typical non-metallic inclusions, which are the origin of failures in very high cycle fatigue in hardened steels [48, 227]. Cleaner steels are promising candidates to improve the reliability of cyclically loaded components in general and wind power plant gearbox bearings in particular. The latter could be used in the production of blue hydrogen, which could, in turn, be used to produce cleaner steels.

WECs in wind turbine gearbox bearings almost exclusively initiate at MnS inclusions is seems unlikely that a way of mitigating the emergence of WECs can be the increased thermodynamic stability of carbides as was proposed by several researchers [105]. Since carbides are usually not initiating cracks, they only seem to play a minor role by potentially providing excess carbon as they are decomposing. However, as was shown in Chapter 5, only 1 at% of carbon is sufficient to stabilize a grain size of ~ 30 nm, and therefore carbon from spheroidized $(Fe,Cr)_3C$ is not necessary to form WEAs in 100Cr6. It is hence unlikely that reduced carbon supply, due to increased carbide stability, would have a significant positive effect. Also, even significantly more stable and thus harder carbides (or nitrides and carbonitrides for that matter) will likely not withstand the cyclic stresses. This means, they too will decompose, as HPT experiments[24] on X30CrMoN15-1 have shown similar deformation of $M_{23}(C,N)_6$ and $Cr(C,N)_2$ as was observed for $(Fe,Cr)_3C$ in 100Cr6 [216]. Reduction of the total carbon content and

[24] Unpublished work by Yu Qin.

replacement with nitrogen, however, might be a viable solution but poses the challenges described above.

Last, a brief outlook regarding the continuation of this work in a narrower sense, i.e., of carrying on some key experiments and analyses that have not been completed in this thesis, is undertaken. Several aspects have not been dealt with conclusively, and open questions remain:

- Is carbon present at crack surfaces? And if it is, which structure does it have? Although it is clear that carbon is missing from the WEAs, it remains yet to be proven that it indeed is located (partially) at the crack surfaces. To this end, cracks have to be located by ultrasound or X-rays inside the bulk. Fracture specimens have to be prepared with appropriate dimensions and positioning of the flaws inside a specimen volume. Then Auger electron spectroscopy (AES) can be utilized to analyze in situ fractured samples in an ultra-high vacuum (UHV) environment as these conditions rule out any sources of contamination. AES also allows conclusions regarding the binding state of carbon. If appropriate crack surface preparation can be ensured, EPMA measurements are feasible in detecting surface carbon, as was demonstrated in analyses of very high cycle fatigue tested specimens, which showed increased carbon signals at fine granular areas [228].
- Closely related to potential graphite formation is the decomposition of cementite as it was observed at cracked $(Fe,Cr)_3C$ precipitates (Chapter 6). To better understand the decomposition of cementite, pin-on-disc fretting experiments with bulk cementite are in preparation. Such an experiment is promising in providing information about the decomposition products, which are expected to be ferrite and graphite. The experiments will be conducted under ultra-high vacuum with the possibility to perform X-ray photoemission spectroscopy in the test chamber, which allows determining carbon bonding states.
- Finally, further insight into the formation mechanism could, in principle, be gained by analyzing textures of WEAs. As shown in subsection 6.2.4, WEAs show deviation from random orientation. Therefore, it is desirable to obtain appropriate data extending the current work, which, however, is not trivial due to several constraints. TEM allows for sufficient spatial resolution, but only partial pole figures can be obtained using SAD. TEM based orientation mapping is limited in capturing a statistically significant number of grains and poses the problem that grain overlap is present in fine-grained WEAs ($< \sim 50$ nm). As samples cannot be extracted for classical XRD texture measurements, using small beam diameters and a rotationally symmetric WEA sample (in micropillar dimensions) in transmission mode can solve this problem, as full pole figures can be measured. If the

hypothesis that WEAs are created through crack surface rubbing and hence WECs precede WEAs, is accurate, this should result in a shear texture. Textures of WEAs surrounding horizontal and vertical cracks should be similar with respect to the orientation of their crack plane (i.e., the approximate shear plane). Relating these textures to the assumed shear planes (and directions) could show if the 'crack first' hypothesis can be correct.

References

[1] Y. Guo, T. Parsons, K. Dykes, R.N. King, A systems engineering analysis of three-point and four-point wind turbine drivetrain configurations, Wind Energy 20(3) (2017) 537-550.
[2] C. Dao, B. Kazemtabrizi, C. Crabtree, Wind turbine reliability data review and impacts on levelised cost of energy, Wind Energy 22(12) (2019) 1848-1871.
[3] Status of Onshore Wind Energy Development in Germany - Year 2019, Deutsche WindGuard GmbH, 2020.
[4] Kraftwerksliste, Bundesnetzagentur, 2020.
[5] Renewable capacity statistics 2020, International Renewable Energy Agency, Abu Dhabi, 2020.
[6] In-depth analysis in support on the COM(2018) 773: A Clean Planet for all: A European long-term strategic vision for a prosperous, modern, competitive and climate neutral economy, European Comission, 2018.
[7] Preise Elektrizität für Haushaltskunden, Eurostat, L-2920 Luxembourg.
[8] C. Kost, S. Shammugam, V. Jülch, H.-T. Nguyen, T. Schlegl, Stromgestehungskosten Erneuerbare Energien, Fraunhofer-Institut für Solare Energiesysteme ISE, 2018.
[9] M. Jansen, I. Staffell, L. Kitzing, S. Quoilin, E. Wiggelinkhuizen, B. Bulder, I. Riepin, F. Müsgens, Offshore wind competitiveness in mature markets without subsidy, Nature Energy (2020).
[10] Windenergiereport Deutschland 2018, Fraunhofer-Institut für Energiewirtschaft und Energiesystemtechnik IEE, Stuttgart, 2019.
[11] T. Burton, N. Jenkins, D. Sharpe, E. Bossanyi, Wind Energy Handbook, 2nd ed., John Wiley & Sons2011.
[12] S. Wang, A.R. Nejad, T. Moan, On design, modelling, and analysis of a 10 - MW medium - speed drivetrain for offshore wind turbines, Wind Energy 23(4) (2020) 1099-1117.
[13] F. Spinato, P.J. Tavner, G.J.W.v. Bussel, E. Koutoulakos, Reliability of wind turbine subassemblies, IET Renewable Power Generation, Institution of Engineering and Technology, 2009, pp. 387-401.
[14] R. Bakhshi, P. Sandborn, Overview of Wind Turbine Field Failure Databases: A Discussion of the Requirements for an Analysis, ASME 2018 Power Conference collocated with the ASME 2018 12th International Conference on Energy Sustainability and the ASME 2018 Nuclear Forum, 2018.
[15] J. Carroll, S. Koukoura, A. McDonald, A. Charalambous, S. Weiss, S. McArthur, Wind turbine gearbox failure and remaining useful life prediction using machine learning techniques, Wind Energy 22(3) (2019) 360-375.
[16] M.H. Evans, White structure flaking (WSF) in wind turbine gearbox bearings: effects of 'butterflies' and white etching cracks (WECs), Materials Science and Technology 28(1) (2012) 3-22.
[17] M.H. Evans, An updated review: white etching cracks (WECs) and axial cracks in wind turbine gearbox bearings, Materials Science and Technology 32(11) (2016) 1133-1169.
[18] Y.J. Li, M. Herbig, S. Goto, D. Raabe, Atomic scale characterization of white etching area and its adjacent matrix in a martensitic 100Cr6 bearing steel, Materials Characterization 123 (2017) 349-353.
[19] H.K.D.H. Bhadeshia, Steels for bearings, Progress in Materials Science 57(2) (2012) 268-435.
[20] J.D. Verhoeven, The Role of the Divorced Eutectoid Transformation in the Spheroidization of 52100 Steel.
[21] W. Song, J. von Appen, P. Choi, R. Dronskowski, D. Raabe, W. Bleck, Atomic-scale investigation of ε and θ precipitates in bainite in 100Cr6 bearing steel by atom probe tomography and ab initio calculations, Acta Materialia 61(20) (2013) 7582-7590.
[22] J.M. Beswick, Fracture and Fatigue Crack Propagation Properties of Hardened 52100 Steel, Metallurgical Transactions A 20A (1989) 196111973.
[23] M. Perez, C. Sidoroff, A. Vincent, C. Esnouf, Microstructural evolution of martensitic 100Cr6 bearing steel during tempering: From thermoelectric power measurements to the prediction of dimensional changes, Acta Materialia 57(11) (2009) 3170-3181.

[24] T. Karsch, H. Bomas, H.W. Zoch, S. Mändl, Influence of hydrogen content and microstructure on the fatigue behaviour of steel SAE 52100 in the VHCF regime, International Journal of Fatigue 60 (2014) 74-89.
[25] S.-C. Lee, W.-Y. Ho, The effects of surface hardening on fracture toughness of carburized steel, Metallurgical Transactions A 20(3) (1989) 519-525.
[26] M.H. Evans, J.C. Walker, C. Ma, L. Wang, R.J.K. Wood, A FIB/TEM study of butterfly crack formation and white etching area (WEA) microstructural changes under rolling contact fatigue in 100Cr6 bearing steel, Materials Science and Engineering: A 570 (2013) 127-134.
[27] P.C. Becker, Microstructural changes around non-metallic inclusions caused by rolling-contact fatigue of ball-bearing steels, Metals Technology 8(1) (1981) 234-243.
[28] A. Grabulov, R. Petrov, H.W. Zandbergen, EBSD investigation of the crack initiation and TEM/FIB analyses of the microstructural changes around the cracks formed under Rolling Contact Fatigue (RCF), International Journal of Fatigue 32(3) (2010) 576-583.
[29] A. Muroga, H. Saka, Analysis of rolling contact fatigued microstructure using focused ion beam sputtering and transmission electron microscopy observation, Scripta Metallurgica et Materialia 33(1) (1995) 151-156.
[30] H. Harada, T. Mikami, M. Shibata, D. Sokai, A. Yamamoto, H. Tsubakino, Microstructural Changes and Crack Initiation with White Etching Area Formation under Rolling/Sliding Contact in Bearing Steel, ISIJ International 45(12) (2005) 1897-1902.
[31] F. Sadeghi, B. Jalalahmadi, T.S. Slack, N. Raje, N.K. Arakere, A Review of Rolling Contact Fatigue, Journal of Tribology 131(4) (2009).
[32] K.L. Johnson, Contact Mechanics, Cambridge University Press, Cambridge, 1985.
[33] O. Zwirlein, H. Schlicht, Werkstoffanstrenung bei Wälzbeanspruchung - Einfluß von Reibung und Eigenspannungen, Zeitschrift für Werkstofftechnik 11 (1980) 1-14.
[34] F. Sadeghi, Elastohydrodynamic lubrication, (2010) 171-226e.
[35] A.P. Voskampk, E.J. Mittemeijer, Crystallographic preferred orientation induced by cyclic rolling contact loading, Metallurgical and Materials Transactions A 27(11) (1996) 3445-3465.
[36] A.P. Voskamp, Material Response to Rolling Contact Loading, Journal of Tribology 107(3) (1985) 359-364.
[37] A.P. Voskamp, R. Österlund, P.C. Becker, O. Vingsbo, Gradual changes in residual stress and microstructure during contact fatigue in ball bearings, Metals Technology 7(1) (1980) 14-21.
[38] G. Lundberg, A. Palmgren, Dynamic Capacity of Rolling Bearings, Journal of Applied Mechanics (1949).
[39] N. Raje, F. Sadeghi, R.G. Rateick, Jr., M.R. Hoeprich, A Numerical Model for Life Scatter in Rolling Element Bearings, Journal of Tribology 130(1) (2007).
[40] N. Weinzapfel, F. Sadeghi, Numerical modeling of sub-surface initiated spalling in rolling contacts, Tribology International 59 (2013) 210-221.
[41] R. Tricot, J. Monnot, M. Lluansi, How Mircrostructural Alterations Affect Fatigue Properties of 52100 Steel, Metals Engineering Quarterly 12(7) (1972) 39-47.
[42] H. Styri, Fatigue Strength of Ball Bearings Races and Heat-Treated 52100 Steel Specimens, Proceedings of the American Society for Testing and Materials 51 (1951) 682-700.
[43] K. Sugino, K. Myamoto, M. Nagumao, A. K., Structural Alterations of bearing steels under rolling contact fatigue, Tansactions ISIJ 10 (1970) 98-111.
[44] R. Österlund, O. Vingsbo, L. Vincent, P. Guiraldenq, Butterflies in fatigued ball bearings – formation mechanism and structure, Scand. J. Metall. 11 (1982) 23-32.
[45] A. Grabulov, U. Ziese, H.W. Zandbergen, TEM/SEM investigation of microstructural changes within the white etching area under rolling contact fatigue and 3-D crack reconstruction by focused ion beam, Scripta Materialia 57(7) (2007) 635-638.
[46] T. Lund, K. Törresvoll, Quantification of Large Inclusions in Bearing Steels, in: J.J.C. Hoo, W.B. Green (Eds.), ASTM International, West Conshohocken, PA, 1998, pp. 27-38.

[47] G. Auclair, F. Ruby-Meyer, R. Meilland, P. Rocabois, Cleanliness Assessment : A Critical Review and a Real Need to Predict Rolling Contact Fatigue Behaviour, in: J.J.C. Hoo, W.B. Green (Eds.), ASTM International, West Conshohocken, PA, 1998, pp. 39-54.
[48] Y. Murakami, Metal Fatigue: Effects of Small Defects and Nonmetallic Inclusions, 2nd ed., Academic Press 2019.
[49] S. Mobasher Moghaddam, F. Sadeghi, K. Paulson, N. Weinzapfel, M. Correns, V. Bakolas, M. Dinkel, Effect of non-metallic inclusions on butterfly wing initiation, crack formation, and spall geometry in bearing steels, International Journal of Fatigue 80 (2015) 203-215.
[50] M.W.J. Lewis, B. Tomkins, A fracture mechanics interpretation of rolling bearing fatigue, Proceedings of the Institution of Mechanical Engineers, Part J: Journal of Engineering Tribology 226(5) (2012) 389-405.
[51] M.H. Evans, A.D. Richardson, L. Wang, R.J.K. Wood, Effect of hydrogen on butterfly and white etching crack (WEC) formation under rolling contact fatigue (RCF), Wear 306(1-2) (2013) 226-241.
[52] S. Mobasher Moghaddam, F. Sadeghi, N. Weinzapfel, A. Liebel, A Damage Mechanics Approach to Simulate Butterfly Wing Formation Around Nonmetallic Inclusions, Journal of Tribology 137(1) (2014).
[53] X. Ai, A Comprehensive Model for Assessing the Impact of Steel Cleanliness on Bearing Performance, Journal of Tribology 137(1) (2014).
[54] S.M. Moghaddam, F. Sadeghi, K. Paulson, N. Weinzapfel, M. Correns, M. Dinkel, A 3D numerical and experimental investigation of microstructural alterations around non-metallic inclusions in bearing steel, International Journal of Fatigue 88 (2016) 29-41.
[55] R.H. Vegter, J.T. Slycke, J. Beswick, S.W. Dean, The Role of Hydrogen on Rolling Contact Fatigue Response of Rolling Element Bearings, Journal of ASTM International 7(2) (2009) 102543.
[56] K. Tanaka, Y. Akiniwa, Fatigue crack propagation behaviour derived from S–N data in very high cycle regime, Fatigue & Fracture of Engineering Materials & Structures 25(8‐9) (2002) 775-784.
[57] T. Sakai, B. Lian, M. Takeda, K. Shiozawa, N. Oguma, Y. Ochi, M. Nakajima, T. Nakamura, Statistical duplex S–N characteristics of high carbon chromium bearing steel in rotating bending in very high cycle regime, International Journal of Fatigue 32(3) (2010) 497-504.
[58] Y. Hong, X. Liu, Z. Lei, C. Sun, The formation mechanism of characteristic region at crack initiation for very-high-cycle fatigue of high-strength steels, International Journal of Fatigue 89 (2016) 108-118.
[59] H. Mughrabi, Specific features and mechanisms of fatigue in the ultrahigh-cycle regime, International Journal of Fatigue 28(11) (2006) 1501-1508.
[60] T. Makino, Y. Neishi, D. Shiozawa, Y. Fukuda, K. Kajiwara, Y. Nakai, Evaluation of rolling contact fatigue crack path in high strength steel with artificial defects, International Journal of Fatigue 68 (2014) 168-177.
[61] J. Lankford, Inclusion-matrix debonding and fatigue crack initiation in low alloy steel, International Journal of Fracture 12(1) (1976) 155-157.
[62] J. Lankford, Initiation and early growth of fatigue cracks in high strength steel, Engineering Fracture Mechanics 9(3) (1977) 617-624.
[63] H.K. Danielsen, F.G. Guzmán, K.V. Dahl, Y.J. Li, J. Wu, G. Jacobs, G. Burghardt, S. Fæster, H. Alimadadi, S. Goto, D. Raabe, R. Petrov, Multiscale characterization of White Etching Cracks (WEC) in a 100Cr6 bearing from a thrust bearing test rig, Wear 370-371 (2017) 73-82.
[64] V. Šmeļova, A. Schwedt, L. Wang, W. Holweger, J. Mayer, Microstructural changes in White Etching Cracks (WECs) and their relationship with those in Dark Etching Region (DER) and White Etching Bands (WEBs) due to Rolling Contact Fatigue (RCF), International Journal of Fatigue 100 (2017) 148-158.
[65] M. Oezel, A. Schwedt, T. Janitzky, R. Kelley, C. Bouchet-Marquis, L. Pullan, C. Broeckmann, J. Mayer, Formation of white etching areas in SAE 52100 bearing steel under rolling contact fatigue – Influence of diffusible hydrogen, Wear 414-415 (2018) 352-365.

[66] J. Gegner, W. Nierlich, Service Loading Analysis of Wind Turbine Gearbox Rolling Bearings Based on X-Ray Diffraction Residual Stress Measurements, Materials Science Forum 768-769 (2014) 723-732.
[67] A. Ruellan, F. Ville, X. Kleber, A. Arnaudon, D. Girodin, Understanding white etching cracks in rolling element bearings: The effect of hydrogen charging on the formation mechanisms, Proceedings of the Institution of Mechanical Engineers, Part J: Journal of Engineering Tribology 228(11) (2014) 1252-1265.
[68] J. Lai, K. Stadler, Investigation on the mechanisms of white etching crack (WEC) formation in rolling contact fatigue and identification of a root cause for bearing premature failure, Wear 364-365 (2016) 244-256.
[69] B. Gould, A. Greco, K. Stadler, X. Xiao, An analysis of premature cracking associated with microstructural alterations in an AISI 52100 failed wind turbine bearing using X-ray tomography, Materials & Design 117 (2017) 417-429.
[70] M.H. Evans, L. Wang, H. Jones, R.J.K. Wood, White etching crack (WEC) investigation by serial sectioning, focused ion beam and 3-D crack modelling, Tribology International 65 (2013) 146-160.
[71] S. Fæster, H.K. Danielsen, X-ray tomography data of White Etching Cracks (WEC), Data in Brief 27 (2019) 104531.
[72] B. Gould, A. Greco, K. Stadler, E. Vegter, X. Xiao, Using advanced tomography techniques to investigate the development of White Etching Cracks in a prematurely failed field bearing, Tribology International 116 (2017) 362-370.
[73] A.F. Bower, The Influence of Crack Face Friction and Trapped Fluid on Surface Initiated Rolling Contact Fatigue Cracks, Journal of Tribology 110(4) (1988) 704-711.
[74] F. Manieri, K. Stadler, G.E. Morales-Espejel, A. Kadiric, The origins of white etching cracks and their significance to rolling bearing failures, International Journal of Fatigue 120 (2019) 107-133.
[75] M. Kohara, T. Kawamura, M. Egami, Study on Mechanism of Hydrogen Generation from Lubricants, Tribology Transactions 49(1) (2006) 53-60.
[76] W. Kruhöffer, J. Loos, WEC Formation in Rolling Bearings under Mixed Friction: lnfluences and Friction Energy Accumulation as lndicator, Tribology Transactions 60(3) (2017) 516-529.
[77] B. Gould, N. Demas, R. Erck, M.C. Lorenzo-Martin, O. Ajayi, A. Greco, The effect of electrical current on premature failures and microstructural degradation in bearing steel, unpublished (2020).
[78] M. Zuercher, Early failure detection for bearings in electrical environments, WCCM 2017, 2017.
[79] H. Surborg, Einfluss von Grundölen und Additiven auf die Bildung von WEC in Wälzlagern, Fakultät für Maschinenbau, Universität Magdeburg, Aachen, 2014.
[80] A.D. Richardson, M.H. Evans, L. Wang, R.J.K. Wood, M. Ingram, B. Meuth, The Evolution of White Etching Cracks (WECs) in Rolling Contact Fatigue-Tested 100Cr6 Steel, Tribol Lett 66(1) (2018) 6.
[81] F. Gutiérrez Guzmán, M. Oezel, G. Jacobs, G. Burghardt, C. Broeckmann, T. Janitzky, Reproduction of white etching cracks under rolling contact loading on thrust bearing and two-disc test rigs, Wear 390-391 (2017) 23-32.
[82] M.H. Evans, L. Wang, R.J.K. Wood, Formation mechanisms of white etching cracks and white etching area under rolling contact fatigue, Proceedings of the Institution of Mechanical Engineers, Part J: Journal of Engineering Tribology 228(10) (2014) 1047-1062.
[83] K. Tamada, H. Tanaka, Occurrence of brittle flaking on bearings used for automotive electrical instruments and auxiliary devices, Wear 199(2) (1996) 245-252.
[84] N. Kino, K. Otani, The influence of hydrogen on rolling contact fatigue life and its improvement, JSAE Review 24(3) (2003) 289-294.
[85] D. Kürten, I. Khader, R. Raga, P. Casajús, N. Winzer, A. Kailer, R. Spallek, M. Scherge, Hydrogen assisted rolling contact fatigue due to lubricant degradation and formation of white etching areas, Engineering Failure Analysis 99 (2019) 330-342.

[86] H. Uyama, H. Yamada, H. Hidaka, N. Mitamura, The Effects of Hydrogen on Microstructural Change and Surface Originated Flaking in Rolling Contact Fatigue, Tribology Online 6(2) (2011) 123-132.
[87] S.W. Ooi, P. Yan, R.H. Vegter, Black oxide coating and its effectiveness on prevention of hydrogen uptake, Materials Science and Technology 35(1) (2019) 12-25.
[88] A.M. Diederichs, A. Schwedt, J. Mayer, T. Dreifert, Electron microscopy analysis of structural changes within white etching areas, Materials Science and Technology 32(16) (2016) 1683-1693.
[89] Y. Murakami, N.N. Yokoyama, K. Takai, Effect of Hydrogen Trapped by Inclusions on Ultra-Long Life Fatigue Failure of Bearing Steel, Journal of the Society of Materials Science, Japan 50(10) (2001) 1068-1073.
[90] S. Fujita, S. Matsuoka, Y. Murakami, G. Marquis, Effect of hydrogen on Mode II fatigue crack behavior of tempered bearing steel and microstructural changes, International Journal of Fatigue 32(6) (2010) 943-951.
[91] H. Matsunaga, N. Shomura, S. Muramoto, M. Endo, Shear mode threshold for a small fatigue crack in a bearing steel, Fatigue & Fracture of Engineering Materials & Structures 34(1) (2011) 72-82.
[92] Y. Murakami, K. Takahashi, R. Kusumoto, Threshold and growth mechanism of fatigue cracks under mode II and III loadings, Fatigue & Fracture of Engineering Materials & Structures 26(6) (2003) 523-531.
[93] S. Okazaki, K. Wada, H. Matsunaga, M. Endo, The influence of static crack-opening stress on the threshold level for shear-mode fatigue crack growth in bearing steels, Engineering Fracture Mechanics 174 (2017) 127-138.
[94] P. Grad, B. Reuscher, A. Brodyanski, M. Kopnarski, E. Kerscher, Mechanism of fatigue crack initiation and propagation in the very high cycle fatigue regime of high-strength steels, Scripta Materialia 67(10) (2012) 838-841.
[95] D. Spriestersbach, A. Brodyanski, J. Lösch, M. Kopnarski, E. Kerscher, Very high cycle fatigue of bearing steels with artificial defects in vacuum, Materials Science and Technology 32(11) (2016) 1111-1118.
[96] D. Spriestersbach, E. Kerscher, The role of local plasticity during very high cycle fatigue crack initiation in high-strength steels, International Journal of Fatigue 111 (2018) 93-100.
[97] S. Averbeck, D. Spriestersbach, E. Kerscher, Mechanism of fine granular area and white etching crack formation in AISI 52100 bearing steel, Theoretical and Applied Fracture Mechanics 108 (2020) 102664.
[98] D. Spriestersbach, P. Grad, E. Kerscher, Threshold values for very high cycle fatigue failure of high-strength steels, Fatigue & Fracture of Engineering Materials & Structures 40(11) (2017) 1708-1717.
[99] S. Averbeck, E. Kerscher, Influence of multiaxial fatigue loading conditions on white etching crack formation, Engineering Fracture Mechanics 174 (2017) 180-195.
[100] W. Holweger, M. Wolf, D. Merk, T. Blass, M. Goss, J. Loos, S. Barteldes, A. Jakovics, White Etching Crack Root Cause Investigations, Tribology Transactions 58(1) (2015) 59-69.
[101] K. Hiraoka, M. Nagao, T. Isomoto, Study on Flaking Process in Bearings by White Etching Area Generation, Journal of ASTM International 3(5) (2006) 1-7.
[102] L. Morsdorf, D. Mayweg, Y. Li, A. Diederichs, D. Raabe, M. Herbig, Moving cracks form white etching areas during rolling contact fatigue in bearings, Materials Science and Engineering: A 771 (2020) 138659.
[103] M. Ščepanskis, A. Jakovičs, I. Kaldre, W. Holweger, B. Nacke, A.M. Diederichs, The Numerical Model of Electrothermal Deformations of Carbides in Bearing Steel as the Possible Cause of White Etching Cracks Initiation, Tribology Letters 59(2) (2015) 37.
[104] P.Y. Tung, E. McEniry, M. Herbig, The role of electric current in the formation of white-etching-cracks, (2020).
[105] H.K.D.H. Bhadeshia, W. Solano-Alvarez, Critical Assessment 13: Elimination of white etching matter in bearing steels, Materials Science and Technology 31(9) (2015) 1011-1015.

[106] M.H. Evans, A.D. Richardson, L. Wang, R.J.K. Wood, Serial sectioning investigation of butterfly and white etching crack (WEC) formation in wind turbine gearbox bearings, Wear 302(1) (2013) 1573-1582.
[107] B. Gould, N.G. Demas, A.C. Greco, The influence of steel microstructure and inclusion characteristics on the formation of premature bearing failures with microstructural alterations, Materials Science and Engineering: A 751 (2019) 237-245.
[108] Y. Kadin, M.Y. Sherif, Energy dissipation at rubbing crack faces in rolling contact fatigue as the mechanism of white etching area formation, International Journal of Fatigue 96 (2017) 114-126.
[109] W. Solano-Alvarez, H.K.D.H. Bhadeshia, White-Etching Matter in Bearing Steel. Part II: Distinguishing Cause and Effect in Bearing Steel Failure, Metallurgical and Materials Transactions A 45(11) (2014) 4916-4931.
[110] H. Sato, T. Murase, T. Fujii, S. Onaka, Y. Watanabe, M. Kato, Formation of a wear-induced layer with nanocrystalline structure in Al–Al3Ti functionally graded material, Acta Materialia 56(17) (2008) 4549-4558.
[111] C. Greiner, Z. Liu, L. Strassberger, P. Gumbsch, Sequence of Stages in the Microstructure Evolution in Copper under Mild Reciprocating Tribological Loading, ACS applied materials & interfaces 8(24) (2016) 15809-19.
[112] X.C. Liu, H.W. Zhang, K. Lu, Strain-Induced Ultrahard and Ultrastable Nanolaminated Structure in Nickel, Science 342(6156) (2013) 337-340.
[113] D. Mayweg, L. Morsdorf, X. Wu, M. Herbig, The role of carbon in the white etching crack phenomenon in bearing steels, Acta Materialia 203 (2021) 116480.
[114] H. Mikami, T. Kawamura, Influence of electrical current on bearing flaking life, SAE Technical Paper 2007-01-0113 (2007) 7-12.
[115] J. Loos, I. Bergmann, M. Goss, Influence of Currents from Electrostatic Charges on WEC Formation in Rolling Bearings, Tribology Transactions 59(5) (2016) 865-875.
[116] T. Haque, S. Korres, J.T. Carey, P.W. Jacobs, J. Loos, J. Franke, Lubricant Effects on White Etching Cracking Failures in Thrust Bearing Rig Tests, Tribology Transactions 61(6) (2018) 979-990.
[117] G.R. Speich, P.R. Swann, Yield Strength and transformation substructure of quenched iron-nickel alloys, Journal of the Iron and Steel Institute (1964) 480-485.
[118] W. Solano-Alvarez, E.J. Pickering, M.J. Peet, K.L. Moore, J. Jaiswal, A. Bevan, H.K.D.H. Bhadeshia, Soft novel form of white-etching matter and ductile failure of carbide-free bainitic steels under rolling contact stresses, Acta Materialia 121 (2016) 215-226.
[119] P.T. Pinard, M. Özel, M. Ploß, S. Richter, Quantitative image analysis of white etching areas in SAE52100 bearing steel, Microscopy and Microanalysis 21(S3) (2015) 459-460.
[120] M.E. Curd, T.L. Burnett, J. Fellowes, P. Yan, P.J. Withers, Redistribution of carbon caused by butterfly defects in bearing steels, Acta Materialia 183 (2020) 390-397.
[121] P.T. Pinard, Electron probe microanalysis of carbon containing steels at a high spatial resolution, Faculty of Georesources and Materials Engineering, RWTH Aachen University, Aachen, 2016.
[122] M.E. Curd, T.L. Burnett, J. Fellowes, J. Donoghue, P. Yan, P.J. Withers, The heterogenous distribution of white etching matter (WEM) around subsurface cracks in bearing steels, Acta Materialia 174 (2019) 300-309.
[123] J.I. Goldstein, D.E. Newbury, J.R. Michael, N.W.M. Ritchie, J.H.J. Scott, D.C. Joy, Scanning Electron Microscopy And X-Ray Microanalysis, Springer, New York, 2018.
[124] Y.Z. Chen, A. Herz, Y.J. Li, C. Borchers, P. Choi, D. Raabe, R. Kirchheim, Nanocrystalline Fe–C alloys produced by ball milling of iron and graphite, Acta Materialia 61(9) (2013) 3172-3185.
[125] Y.J. Li, M. Herbig, S. Goto, D. Raabe, Formation of nanosized grain structure in martensitic 100Cr6 bearing steels upon rolling contact loading studied by atom probe tomography, Materials Science and Technology 32(11) (2016) 1100-1105.
[126] G.A. Nematollahi, J. von Pezold, J. Neugebauer, D. Raabe, Thermodynamics of carbon solubility in ferrite and vacancy formation in cementite in strained pearlite, Acta Materialia 61(5) (2013) 1773-1784.

[127] J.H. Kang, B. Hosseinkhani, C.A. Williams, M.P. Moody, P.A.J. Bagot, P.E.J. Rivera-Díaz-del-Castillo, Solute redistribution in the nanocrystalline structure formed in bearing steels, Scripta Materialia 69(8) (2013) 630-633.
[128] Y.J. Li, A. Kostka, P. Choi, S. Goto, D. Ponge, R. Kirchheim, D. Raabe, Mechanisms of subgrain coarsening and its effect on the mechanical properties of carbon-supersaturated nanocrystalline hypereutectoid steel, Acta Materialia 84 (2015) 110-123.
[129] J. Takahashi, M. Kosaka, K. Kawakami, T. Tarui, Change in carbon state by low-temperature aging in heavily drawn pearlitic steel wires, Acta Materialia 60(1) (2012) 387-395.
[130] W. Lu, M. Herbig, C.H. Liebscher, L. Morsdorf, R.K.W. Marceau, G. Dehm, D. Raabe, Formation of eta carbide in ferrous martensite by room temperature aging, Acta Materialia 158 (2018) 297-312.
[131] H. Abe, H. Naramoto, C. Kinoshita, Amorphization of Graphite under Ion or Electron Irradiation, 1994, p. 383.
[132] F. Vurpillot, A. Bostel, D. Blavette, Trajectory overlaps and local magnification in three-dimensional atom probe, Applied Physics Letters 76(21) (2000) 3127-3129.
[133] T. Sugano, N. Ohashi, T. Tsurumi, O. Fukunaga, Pressure and temperature region of diamond formation in systems graphite and Fe containing alloy, Diamond and Related Materials 5(1) (1996) 29-33.
[134] A. Okamoto, Graphite Formation in High-Purity Cold-Rolled Carbon Steels, METALLURGICAL TRANSACTIONS A 20A (1989).
[135] V.N. Gridnev, V.G. Gavriljuk, Cementite Decomposition in Steel under Plastic Deformation (A Review), Phys. Metals 4(3) (1982) 531-551.
[136] P. Stoyanov, P.A. Romero, R. Merz, M. Kopnarski, M. Stricker, P. Stemmer, M. Dienwiebel, M. Moseler, Nanoscale sliding friction phenomena at the interface of diamond-like carbon and tungsten, Acta Materialia 67 (2014) 395-408.
[137] Y. Liao, R. Pourzal, M. A. Wimmer, J. J. Jacobs, A. Fischer, L.D. Marks, Graphitic Tribological Layers in Metal-on-Metal Hip Replacements, Science 334(1687-1690) (2011).
[138] D.-S. Wang, S.-Y. Chang, Y.-C. Huang, J.-B. Wu, H.-J. Lai, M.-S. Leu, Nanoscopic observations of stress-induced formation of graphitic nanocrystallites at amorphous carbon surfaces, Carbon 74 (2014) 302-311.
[139] T.-B. Ma, Y.-Z. Hu, H. Wang, Molecular dynamics simulation of shear-induced graphitization of amorphous carbon films, Carbon 47(8) (2009) 1953-1957.
[140] W.L. Zhou, Y. Ikuhara, W. Zhao, J. Tang, A transmission electron microscopy study of amorphization of graphite by mechanical milling, Carbon 33(8) (1995) 1177-1180.
[141] H.J. Grabke, Surface and Grain Boundary Segregation on and in Iron and Steels, ISIJ International 29(7) (1989) 529-538.
[142] H.J. Grabke, W. Paulitschke, G. Tauber, H. Viefhaus, Equilibrium surface segregation of dissolved nonmetal atoms on iron(100) faces, Surface Science 63 (1977) 377-389.
[143] D.E. Jiang, E.A. Carter, Carbon atom adsorption on and diffusion into Fe(110) and Fe(100) from first principles, Physical Review B 71(4) (2005).
[144] G. Panzner, W. Diekmann, The Bonding state of carbon segregated to alpha-iron surfaces and on iron carbide surfaces studied by electron spectroscopy, Surface Science 160 (1985) 253-270.
[145] W. Arabczyk, F. Storbeck, H.J. Müssig, Electron spectroscopy studies on carbon segregation from a mono-crystalline α-Fe(111) specimen, Applied Surface Science 65-66 (1993) 94-98.
[146] H.A. Mohamed, J. Washburn, MECHANISM OF SOLID-STATE PRESSURE WELDING, Weld. J. 54(9) (1975) S302-S310.
[147] S. Suresh, R.O. Ritchie, The Propagation of Short Fatigue Cracks, International Metals Review 29(6) (1984) 445.
[148] J. Chakraborty, P.P. Chattopadhyay, D. Bhattacharjee, I. Manna, Microstructural Refinement of Bainite and Martensite for Enhanced Strength and Toughness in High-Carbon Low-Alloy Steel, Metallurgical and Materials Transactions A 41(11) (2010) 2871-2879.

[149] R.O. Ritchie, Mechanisms of fatigue crack propagation in metals, ceramics and composites: Role of crack tip shielding, Materials Science and Engineering: A 103(1) (1988) 15-28.
[150] J. Tong, R. Yates, M.W. Brown, A model for sliding mode crack closure part I: Theory for pure mode II loading, Engineering Fracture Mechanics 52(4) (1995) 599-611.
[151] E.K. Tschegg, A contribution to mode III fatigue crack propagation, Materials Science and Engineering 54(1) (1982) 127-136.
[152] Y. Murakami, Y. Fukushima, K. Toyama, S. Matsuoka, Fatigue crack path and threshold in Mode II and Mode III loadings, Engineering Fracture Mechanics 75(3) (2008) 306-318.
[153] P. Choi, M. da Silva, U. Klement, T. Al-Kassab, R. Kirchheim, Thermal stability of electrodeposited nanocrystalline Co-1.1at.%P, Acta Materialia 53(16) (2005) 4473-4481.
[154] B. Färber, E. Cadel, A. Menand, G. Schmitz, R. Kirchheim, Phosphorus segregation in nanocrystalline Ni–3.6 at.% P alloy investigated with the tomographic atom probe (TAP), Acta Materialia 48(3) (2000) 789-796.
[155] A.J. Detor, M.K. Miller, C.A. Schuh, Solute distribution in nanocrystalline Ni–W alloys examined through atom probe tomography, Philosophical Magazine 86(28) (2006) 4459-4475.
[156] Setsuo Takaki, T. Tsuchiyama, K. Nakashima, H. Hidaka, K. Kawasaki, Y. Futamura, Microstructure Development of Steel during Severe Plastic Deformation, METALS AND MATERIALS International 10(6) (2004) 533-539.
[157] J. Weissmüller, Alloy thermodynamics in nanostructures, Journal of Materials Research 9(1) (1994) 4-7.
[158] J. Weissmüller, Alloy effects in nanostructures, Nanostructured Materials 3(1) (1993) 261-272.
[159] R. Kirchheim, Reducing grain boundary, dislocation line and vacancy formation energies by solute segregation. I. Theoretical background, Acta Materialia 55(15) (2007) 5129-5138.
[160] R. Kirchheim, Reducing grain boundary, dislocation line and vacancy formation energies by solute segregationII. Experimental evidence and consequences, Acta Materialia 55(15) (2007) 5139-5148.
[161] R. Kirchheim, Grain coarsening inhibited by solute segregation, Acta Materialia 50(2) (2002) 413-419.
[162] S.K. Suram, K. Rajan, Calibration of reconstruction parameters in atom probe tomography using a single crystallographic orientation, Ultramicroscopy 132 (2013) 136-142.
[163] Y.J. Li, P. Choi, S. Goto, C. Borchers, D. Raabe, R. Kirchheim, Evolution of strength and microstructure during annealing of heavily cold-drawn 6.3GPa hypereutectoid pearlitic steel wire, Acta Materialia 60(9) (2012) 4005-4016.
[164] F. Bergner, A. Ulbricht, C. Heintze, Estimation of the solubility limit of Cr in Fe at 300°C from small-angle neutron scattering in neutron-irradiated Fe–Cr alloys, Scripta Materialia 61(11) (2009) 1060-1063.
[165] G. Miyamoto, K. Shinbo, T. Furuhara, Quantitative measurement of carbon content in Fe–C binary alloys by atom probe tomography, Scripta Materialia 67(12) (2012) 999-1002.
[166] J. Takahashi, K. Kawakami, Y. Kobayashi, Study on Quantitative Analysis of Carbon and Nitrogen in Stoichiometric θ-Fe3C and γ'-Fe4N by Atom Probe Tomography, Microscopy and Microanalysis 26(2) (2020) 185-193.
[167] B.A. Rickinson, D.H. Kirkwood, Equilibrium partition coefficients for ferrite/liquid and austenite/liquid in Fe-Cr-C alloys, Metal Science 12(3) (1978) 138-146.
[168] C. Zhang, A. Loucif, M. Jahazi, R. Tremblay, L.-P. Lapierre, On the Effect of Filling Rate on Positive Macrosegregation Patterns in Large Size Cast Steel Ingots, Applied Sciences 8(10) (2018) 1878.
[169] Y.J. Li, P. Choi, C. Borchers, Y.Z. Chen, S. Goto, D. Raabe, R. Kirchheim, Atom probe tomography characterization of heavily cold drawn pearlitic steel wire, Ultramicroscopy 111(6) (2011) 628-32.

[170] W. Song, P.-P. Choi, G. Inden, U. Prahl, D. Raabe, W. Bleck, On the Spheroidized Carbide Dissolution and Elemental Partitioning in High Carbon Bearing Steel 100Cr6, Metallurgical and Materials Transactions A 45(2) (2013) 595-606.
[171] M. Herbig, D. Raabe, Y.J. Li, P. Choi, S. Zaefferer, S. Goto, Atomic-scale quantification of grain boundary segregation in nanocrystalline material, Physical review letters 112(12) (2014) 126103.
[172] B.M. Jenkins, F. Danoix, M. Goune, P.A.J. Bagot, Z. Peng, M.P. Moody, B. Gault, Reflections on the Analysis of Interfaces and Grain Boundaries by Atom Probe Tomography, Microscopy and microanalysis : the official journal of Microscopy Society of America, Microbeam Analysis Society, Microscopical Society of Canada 26(2) (2020) 247-257.
[173] M.K. Miller, M.G. Hetherington, Local magnification effects in the atom probe, Surface Science 246(1) (1991) 442-449.
[174] S. Ohsaki, K. Hono, H. Hidaka, S. Takaki, Characterization of nanocrystalline ferrite produced by mechanical milling of pearlitic steel, Scripta Materialia 52(4) (2005) 271-276.
[175] G.M. Cheng, W.W. Jian, W.Z. Xu, H. Yuan, P.C. Millett, Y.T. Zhu, Grain Size Effect on Deformation Mechanisms of Nanocrystalline bcc Metals, Materials Research Letters 1(1) (2013) 26-31.
[176] Y.Z. Chen, G. Csiszár, J. Cizek, C. Borchers, T. Ungár, S. Goto, R. Kirchheim, On the formation of vacancies in α-ferrite of a heavily cold-drawn pearlitic steel wire, Scripta Materialia 64(5) (2011) 390-393.
[177] Y. Buranova, H. Rösner, S.V. Divinski, R. Imlau, G. Wilde, Quantitative measurements of grain boundary excess volume from HAADF-STEM micrographs, Acta Materialia 106 (2016) 367-373.
[178] K. Edalati, Z. Horita, A review on high-pressure torsion (HPT) from 1935 to 1988, Materials Science and Engineering: A 652 (2016) 325-352.
[179] Y. Li, D. Raabe, M. Herbig, P.-P. Choi, S. Goto, A. Kostka, H. Yarita, C. Borchers, R. Kirchheim, Segregation Stabilizes Nanocrystalline Bulk Steel with Near Theoretical Strength, Physical review letters 113(10) (2014) 106104.
[180] J.W. Cahn, The impurity-drag effect in grain boundary motion, Acta Metallurgica 10(9) (1962) 789-798.
[181] T. Vojtek, J. Pokluda, A. Hohenwarter, R. Pippan, Three-dimensional morphology of fracture surfaces generated by modes II and III fatigue loading in ferrite and austenite, Engineering Fracture Mechanics 108 (2013) 285-293.
[182] J. Pokluda, R. Pippan, T. Vojtek, A. Hohenwarter, Near-threshold behaviour of shear-mode fatigue cracks in metallic materials, Fatigue & Fracture of Engineering Materials & Structures 37(3) (2014) 232-254.
[183] M. Umemoto, Z.G. Liu, H. Takaoka, M. Sawakami, K. Tsuchiya, K. Masuyama, Production of bulk cementite and its characterization, Metallurgical and Materials Transactions A 32(8) (2001) 2127-2131.
[184] B.C. Zheng, Z.F. Huang, J.D. Xing, Y.Y. Xiao, X. Fan, Y. Wang, Effects of Chromium Addition on Preparation and Properties of Bulk Cementite, JOURNAL OF IRON AND STEEL RESEARCH 23(8) (2016) 842-850.
[185] S. Zaefferer, On the formation mechanisms, spatial resolution and intensity of backscatter Kikuchi patterns, Ultramicroscopy 107(2) (2007) 254-266.
[186] P. Moeck, S. Rouvimov, E.F. Rauch, M. Véron, H. Kirmse, I. Häusler, W. Neumann, D. Bultreys, Y. Maniette, S. Nicolopoulos, High spatial resolution semi-automatic crystallite orientation and phase mapping of nanocrystals in transmission electron microscopes, Crystal Research and Technology 46(6) (2011) 589-606.
[187] D. Caillard, An in situ study of hardening and softening of iron by carbon interstitials, Acta Materialia 59(12) (2011) 4974-4989.
[188] R.A. Johnson, Clustering of carbon atoms in α-iron, Acta Metallurgica 15(3) (1967) 513-517.
[189] G.A. Nematollahi, B. Grabowski, D. Raabe, J. Neugebauer, Multiscale description of carbon-supersaturated ferrite in severely drawn pearlitic wires, Acta Materialia 111 (2016) 321-334.

[190] D. Mayweg, L. Morsdorf, Y. Li, M. Herbig, Correlation between grain size and carbon content in White Etching Areas in bearings, Unpublished (2020).
[191] O.H.E. West, A.M. Diederichs, H. Alimadadi, K.V. Dahl, M.A.J. Somers, Application of Complementary Techniques for Advanced Characterization of White Etching Cracks, Pract. Metallogr. 50(6) (2013).
[192] M.H. Evans, A.D. Richardson, L. Wang, R.J.K. Wood, W.B. Anderson, Confirming subsurface initiation at non-metallic inclusions as one mechanism for white etching crack (WEC) formation, Tribology International 75 (2014) 87-97.
[193] A. Ruellan, Tribological analysis of White Etching Crack (WEC) failures in Rolling Element Bearings, 2014.
[194] J.A. Martin, S.F. Borgese, A.D. Eberhardt, Microstructural alterations of rolling bearing steels undergoing cyclic stressing, Trans. ASME J. Basic Eng. 88 (1966) 555-567.
[195] T. Sakai, Review and Prospects for Current Studies on Very High Cycle Fatigue of Metallic Materials for Machine Structural Use, Journal of Solid Mechanics and Materials Engineering 3(3) (2009) 425-439.
[196] K. Shiozawa, Y. Morii, S. Nishino, L. Lu, Subsurface crack initiation and propagation mechanism in high-strength steel in a very high cycle fatigue regime, International Journal of Fatigue 28(11) (2006) 1521-1532.
[197] Y. Qin, J. Li, M. Herbig, Microstructural origin of the outstanding durability of the high nitrogen bearing steel X30CrMoN15-1, Materials Characterization 159 (2020) 110049.
[198] A.R. Hinkle, J.F. Curry, H. Lim, B.L. Nation, M.R. Jones, J. Wellington-Johnson, P. Lu, N. Argibay, M. Chandross, Low friction in bcc metals via grain boundary sliding, Physical Review Materials 4(6) (2020).
[199] N. Argibay, M. Chandross, S. Cheng, J.R. Michael, Linking microstructural evolution and macro-scale friction behavior in metals, J. Mater. Sci. 52 (2017) 2780.
[200] N. Beckmann, P.A. Romero, D. Linsler, M. Dienwiebel, U. Stolz, M. Moseler, P. Gumbsch, Origins of Folding Instabilities on Polycrystalline Metal Surfaces, Physical Review Applied 2(6) (2014).
[201] D.A. Hughes, N. Hansen, High angle boundaries formed by grain subdivision mechanisms, Acta Materialia 45(9) (1997) 3871-3886.
[202] E.O. Hall, The Deformation and Ageing of Mild Steel: III Discussion of Results, Proceedings of the Physical Society. Section B 64(9) (1951) 747-753.
[203] A.H. Chokshi, A. Rosen, J. Karch, H. Gleiter, On the validity of the hall-petch relationship in nanocrystalline materials, Scripta Metallurgica 23(10) (1989) 1679-1683.
[204] H. Hahn, P. Mondal, K.A. Padmanabhan, Plastic deformation of nanocrystalline materials, Nanostructured Materials 9(1) (1997) 603-606.
[205] J. Schiøtz, F.D. Di Tolla, K.W. Jacobsen, Softening of nanocrystalline metals at very small grain sizes, Nature 391(6667) (1998) 561-563.
[206] J. Schiøtz, K.W. Jacobsen, A Maximum in the Strength of Nanocrystalline Copper, Science 301(5638) (2003) 1357.
[207] R.J. Asaro, P. Krysl, B. Kad, Deformation mechanism transitions in nanoscale fcc metals, Philosophical Magazine Letters 83(12) (2003) 733-743.
[208] J. Hu, Y.N. Shi, X. Sauvage, G. Sha, K. Lu, Grain boundary stability governs hardening and softening in extremely fine nanograined metals, Science 355(6331) (2017) 1292-1296.
[209] C.A. Schuh, T.G. Nieh, H. Iwasaki, The effect of solid solution W additions on the mechanical properties of nanocrystalline Ni, Acta Materialia 51(2) (2003) 431-443.
[210] U. Erb, Electrodeposited nanocrystals: Synthesis, properties and industrial applications, Nanostructured Materials 6(5) (1995) 533-538.
[211] U. Erb, A.M. El-Sherik, G. Palumbo, K.T. Aust, Synthesis, structure and properties of electroplated nanocrystalline materials, Nanostructured Materials 2(4) (1993) 383-390.
[212] M. Chandross, N. Argibay, Ultimate Strength of Metals, Physical review letters 124(12) (2020) 125501.

[213] T.D. Shen, R.B. Schwarz, S. Feng, J.G. Swadener, J.Y. Huang, M. Tang, J. Zhang, S.C. Vogel, Y. Zhao, Effect of solute segregation on the strength of nanocrystalline alloys: Inverse Hall–Petch relation, Acta Materialia 55(15) (2007) 5007-5013.
[214] L. Wang, J. Teng, P. Liu, A. Hirata, E. Ma, Z. Zhang, M. Chen, X. Han, Grain rotation mediated by grain boundary dislocations in nanocrystalline platinum, Nature Communications 5(1) (2014) 4402.
[215] D. Raabe, Recovery and Recrystallization: Phenomena, Physics, Models, Simulation, in: D.E. Laughlin, K. Hono (Eds.), Physical Metallurgy (Fifth Edition), Elsevier, Oxford, 2014, pp. 2291-2397.
[216] Y. Qin, D. Mayweg, P.-Y. Tung, R. Pippan, M. Herbig, Mechanism of cementite decomposition in 100Cr6 bearing steels during high pressure torsion, Acta Materialia 201 (2020) 79-93.
[217] C. Borchers, R. Kirchheim, Cold-drawn pearlitic steel wires, Progress in Materials Science 82 (2016) 405-444.
[218] Y. Ivanisenko, W. Lojkowski, R.Z. Valiev, H.J. Fecht, The mechanism of formation of nanostructure and dissolution of cementite in a pearlitic steel during high pressure torsion, Acta Materialia 51(18) (2003) 5555-5570.
[219] Y.J. Li, P. Choi, C. Borchers, S. Westerkamp, S. Goto, D. Raabe, R. Kirchheim, Atomic-scale mechanisms of deformation-induced cementite decomposition in pearlite, Acta Materialia 59(10) (2011) 3965-3977.
[220] N. Maruyama, T. Tarui, H. Tashiro, Atom probe study on the ductility of drawn pearlitic steels, Scripta Materialia 46(8) (2002) 599-603.
[221] X. Sauvage, J. Copreaux, F. Danoix, D. Blavette, Atomic-scale observation and modelling of cementite dissolution in heavily deformed pearlitic steels, Philosophical Magazine A 80(4) (2000) 781-796.
[222] A.W. Cochardt, G. Schoek, H. Wiedersich, Interaction between dislocations and interstitial atoms in body-centered cubic metals, Acta Metallurgica 3(6) (1955) 533-537.
[223] L. Ventelon, B. Lüthi, E. Clouet, L. Proville, B. Legrand, D. Rodney, F. Willaime, Dislocation core reconstruction induced by carbon segregation in bcc iron, Physical Review B 91(22) (2015) 220102.
[224] W. Guo, E.A. Jägle, P.-P. Choi, J. Yao, A. Kostka, J.M. Schneider, D. Raabe, Shear-Induced Mixing Governs Codeformation of Crystalline-Amorphous Nanolaminates, Physical review letters 113(3) (2014) 035501.
[225] P. Grammelis, N. Margaritis, E. Karampinis, 2 - Solid fuel types for energy generation: Coal and fossil carbon-derivative solid fuels, in: J. Oakey (Ed.), Fuel Flexible Energy Generation, Woodhead Publishing, Boston, 2016, pp. 29-58.
[226] D. Spreitzer, J. Schenk, Reduction of Iron Oxides with Hydrogen—A Review, steel research international 90(10) (2019) 1900108.
[227] H. Mughrabi, On 'multi-stage' fatigue life diagrams and the relevant life-controlling mechanisms in ultrahigh-cycle fatigue, Fatigue & Fracture of Engineering Materials & Structures 25 (2002) 755-764.
[228] J.M. Zhang, S.X. Li, Z.G. Yang, G.Y. Li, W.J. Hui, Y.Q. Weng, Influence of inclusion size on fatigue behavior of high strength steels in the gigacycle fatigue regime, International Journal of Fatigue 29(4) (2007) 765-771.

Curriculum Vitae

David Mayweg

david.mayweg@gmail.com

Education

02/2021	Dr.-Ing., *Rheinisch-Westfälische Technische Hochschule Aachen*
05/2017	M.Sc. Materials Science and Engineering, *Universität Siegen*
07/2011	B.Sc. Mechanical Engineering, *Universität Siegen*
02-06/2010	Spring semester *Beijing University of Technology, Beijing, China*

Professional

06/2017-present	Research scientist *Max-Planck-Institut für Eisenforschung GmbH*, Düsseldorf Department of Microstructure Physics and Alloy Design
07/2011-09/2014	Design engineer *Achenbach Buschhütten GmbH & Co. KG*, Germany Procurement & Production Manager *Achenbach Asia Pacific*, Taicang, Jiangsu, VR China
08/2007-06/2011	Student trainee *Achenbach Buschhütten GmbH & Co. KG*, Germany

Publications

Mayweg, D.; Morsdorf, L.; Li, Y.J.; Herbig, M.: *Correlation between grain size and carbon content in white etching areas in bearings*, under review at Acta Materialia (2021)

Ikehata, H., **Mayweg, D.**; Jägle, E.A.: *Grain refinement of Fe-Ti alloys fabricated by laser powder bed fusion*, under review at Materials & Design (2021)

Wu, X.; **Mayweg, D.**; Ponge, D., Li, Z.: *Microstructure and deformation behavior of two TWIP/TRIP high entropy alloys upon grain refinement*, Materials Science and Engineering A 802, 140661 (2021)

Mayweg, D.; Morsdorf, L.; Wu, X.; Herbig, M.: *The role of carbon in the white etching crack phenomenon in bearing steels*, Acta Materialia 203, 116480 (2021)

Qin, Y.; **Mayweg, D.**; Tung, P.-Y.; Pippan, R.; Herbig, M.: *Mechanism of cementite decomposition in 100Cr6 bearing steel during high pressure torsion*, Acta Materialia 201, 79-93 (2020)

Balachandran, S.; Zachariah, Z.; Fischer, A.; **Mayweg, D.**; Wimmer, M. A.; Raabe, D.; Herbig, M.: *Atomic Scale Origin of Metal Ion Release from Hip Implant Taper Junctions.* Advanced Science, 1903008 (2020)

Morsdorf, L.; **Mayweg, D**.; Li, Y.; Diederichs, A.; Raabe, D.; Herbig, M.: *Moving cracks form white etching areas during rolling contact fatigue in bearings*. Materials Science and Engineering A 771, 138659 (2020)